3D microscopy by holographic localization of Brownian metallic nanoparticles

Ariadna Martinez Marrades

To cite this version:

Ariadna Martinez Marrades. 3D microscopy by holographic localization of Brownian metallic nanoparticles. Other [cond-mat.other]. Université Pierre et Marie Curie - Paris VI, 2015. English. NNT : 2015PA066018 . tel-01173962

HAL Id: tel-01173962
https://theses.hal.science/tel-01173962v1

Submitted on 8 Jul 2015

HAL is a multi-disciplinary open access archive for the deposit and dissemination of scientific research documents, whether they are published or not. The documents may come from teaching and research institutions in France or abroad, or from public or private research centers.

L'archive ouverte pluridisciplinaire **HAL**, est destinée au dépôt et à la diffusion de documents scientifiques de niveau recherche, publiés ou non, émanant des établissements d'enseignement et de recherche français ou étrangers, des laboratoires publics ou privés.

Thèse de Doctorat de
l'Université Paris 6 - Pierre et Marie Curie

Spécialité

Physique

École doctorale 391 : ≪ Sciences mécaniques, acoustique, électronique & robotique de Paris ≫

présentée par

Ariadna Martinez-Marrades

pour obtenir le grade de

DOCTEUR de l'UNIVERSITÉ PARIS 6

3D Microscopy by Holographic Localization of Brownian Metallic Nanoparticles

Soutenance prévue le 06 janvier 2015 devant le jury composé de

Mme Sophie Brasselet	Rapporteur
Mme. María García-Parajo	Rapporteur
M. Sylvain Gigan	Examinateur
M. Michel Gross	Examinateur
M. Sébastien Bidault	Examinateur
M. Gilles Tessier	Directeur de thèse

Acknowledgements

Une thèse est comme un long voyage, avec des moments très excitants, d'autres un peu plus ennuyeux. Mais, par-dessus tout, ces trois années de thèse n'ont pas été un voyage solitaire, loin de là ! Tout d'abord, je remercie Gilles Tessier de m'avoir donné l'opportunité de travailler dans cet excellent laboratoire qu'est l'Institut Langevin. Je suis très reconnaissante de la confiance et la liberté qu'il m'a accordée dès le début de ma thèse. Avec le recul, cette liberté s'est avéré très enrichissante, à la fois sur le plan personnel et professionnel. En fin de comptes, comme le dit le proverbe, "une mer calme n'a jamais fait un bon marin".

Je tiens également à remercier tous les membres du jury pour avoir accepté d'évaluer mon travail de recherche : Sophie Brasselet et Maria Garcia-Parajo qui ont accepté d'être les rapporteurs, Sylvain Gigan pour avoir présidé le jury, ainsi que Michel Gross et Sébastien Bidault en tant qu'examinateurs.

Michel et Sébastien méritent un merci à part, pour avoir suivi de près différentes étapes de ma thèse. Tous les deux étaient toujours prêts à discuter avec moi: Michel pour les questions d'holographie et de programmation bien poussées, Sébastien pour... tout le reste ! Le soutien de Sébastien, ainsi que son humour pointu, m'ont été précieux. Dans la même optique, j'exprime toute ma gratitude à Yannick de Wilde, toujours bienveillant et enthousiaste envers mes travaux. Enfin, un grand merci aussi à Frédéric Kanoufi. Notre collaboration combinant holographie et électrochimie a redonné du sens à mon travail à des moments bien critiques. Son énergie infatigable -revêtue d'une attitude calme- ainsi que son optimisme m'ont donné un grand élan à plusieurs reprises. Tous les cinq (Gilles, Michel, Sébastien, Yannick et Frédéric) ont gagné mon admiration et ont été mes références de ce que signifie être chercheur aujourd'hui.

Je remercie d'autres personnes avec qui j'ai eu la chance de collaborer pendant ma thèse: Chris Batchelor-McAuley et Kristina Tschulik de l'Université d'Oxford, ainsi que Jean-François Rupprecht, de l'UPMC à Paris. Grâce à eux j'ai découvert l'énorme richesse de la recherche interdisciplinaire. Malgré nos différentes spécialisations, nous avons su trouver les mots afin d'arriver à un terrain d'entente, et ce dans une ambiance très amicale. Je remercie également Anisha Patel et Vitor Brasiliense et je leur souhaite le meilleur par la suite avec leurs manips "d'électrochimie holographique". Mes meilleurs vœux aussi pour Elodie Tiran et Elodie Perros, les deux stagiaires avec qui j'ai partagé mon sombre sous-sol, aujourd'hui toutes les deux en thèse à Langevin. Enfin, je tiens à remercier Gloria Foulet et Clarisse pour leur accueil chaleureux lors de ma mission complémentaire à l'Ecole Centrale avec Olivier Loison, que je remercie aussi. Les journées passées là-bas étaient marquées par une atmosphère rigoureusement soignée qui me tient à coeur.

Dans un cadre plus personnel, je remercie mes supercopines du labo: Emilie, Daria, Camille et Anne. Nos activités multiples en dehors du labo ont adouci les coups intrinsèques à la thèse: des brunchs, des ateliers cuisine, des sessions de PPG et zumba, la piscine, de nombreuses soirées… Et bien sûr je remercie aussi mes copains masculins, toujours plus nombreux dans notre domaine, avec lesquels nous avons aussi partagé des très bons moments aussi bien à l'intérieur qu'à l'extérieur du labo: Baptiste, Olivier, Pierre, Nico et Marc. La plupart d'entre eux travaillent et vivent déjà ailleurs; le reste sont, comme moi, en train de dire au revoir à une époque importante. Mais mon départ me fait d'autant plus peine car j'ai aussi croisé des gens top sur la fin de cette thèse dont la plupart sont toujours à Langevin. Heureusement, je suis sûre de revoir François, Fish, Mai, Clément, Nikos, Gautier, Jerôme et Marion sur les pistes de danse!

Enfin, je remercie ma famille ainsi que ma famille politique pour leur soutien inconditionnel. Malgré la distance, ils sont restés très près de moi dans les moments les plus importants ces trois dernières années. Un sincère merci aussi à mes copains catalans pour leur soutient, compréhension et fidélité de là où ils se trouvent. Cette réussite est aussi grâce à eux et je les porte dans mon cœur partout où je vais.

Abstract

In this thesis work, we present a novel stochastic microscopy technique based on Digital Holography for the 3D mapping of optical intensity distributions. We show that this far-field, wide-field, 3D microscopy can be turned into both a superresolution and a near-field imaging technique. To do so, we use metallic nanoparticles undergoing Brownian motion as stochastic local field probes that we localize in three-dimensions in order to overcome the diffraction limit. The random motion of the particles allows for a complete exploration of the sample. Beyond simple localization, the gold markers can actually be envisaged as extremely local electromagnetic field probes, able to scatter light into the far-field. The technique we propose here is therefore a combination of the concepts of superlocalization and NSOM microscopies. The possibilities of the technique are illustrated through the 3D optical mapping of an evanescent and a propagative wave.

Fast computation methods allow us to localize hundreds of particles per minute with accuracies as good as $3 \times 3 \times 10$ nm^3 for immobilized particles. In addition to optical intensity mapping, we show a particular application in electrochemistry, by coupling our high resolution images with electrochemical oxidation measurements on silver nanoparticles in solution at the vicinity of an electrode.

Our results pave the way for a new subwavelength imaging technique, well adapted to optical characterization in water-based systems (such as in emerging microfluidics studies), which are mostly inaccessible to electron microscopy or local probe microscopies.

Keywords: Digital holography, Three-dimensional microscopy, Optical scattering, Superresolution, Near-field microscopy, Metallic nanoparticles.

Résumé

Nous présentons dans ce manuscrit une nouvelle technique de microscopie stochastique basée sur un montage d'Holographie Digitale pour l'imagerie des distributions d'intensité optique. Nous montrons comment cette technique de champ lointain peut être adaptée afin d'obtenir des images de superrésolution ainsi que de champ proche. En pratique, nous imageons des nanoparticules métalliques en mouvement Brownien dans un liquide, que nous localisons ensuite dans le but de contourner la limite de diffraction. Le mouvement aléatoire des particules nous permet une exploration complète de l'échantillon. Au-delà de la simple localisation, ces marqueurs métalliques agissent comme des sondes locales du champ électromagnétique environnant, pouvant notamment diffuser la lumière confinée vers le champ lointain. La technique que nous proposons ici est donc une combinaison des concepts de superlocalisation et de NSOM. Les possibilités de cette nouvelle technique sont illustrées à travers l'imagerie de l'intensité optique d'une onde évanescente et d'une onde propagative.

Grâce à des méthodes de calcul très performantes, nous sommes capables de localiser des centaines de particules par minute, avec une précision de l'ordre de $3 \times 3 \times 10$ nm^3 pour des particules immobiles. En plus de l'imagerie des distributions de champ optique, nous présentons une application combinant nos mesures superrésolues et des mesures d'électrochimie pour l'étude des processus d'oxydation de nanoparticules d'argent à proximité d'une électrode.

Nos résultats ouvrent la voie à une nouvelle technique d'imagerie superrésolue, particulièrement bien adaptée à la caractérisation optique dans des milieux liquides (comme des systèmes microfluidiques), qui étaient jusqu'à présent inaccessibles par microscopie électronique ou par des microscopies à sonde locale.

Mots clé: Holographie digitale, Microscopie tridimensionnelle, Diffusion optique, Superrésolution, Microscopie de champ proche, Nanoparticules métalliques.

Résumé Substantiel

Le travail de thèse développé dans ce manuscrit consiste principalement à utiliser la localisation de Nano Particules Métalliques (NPMs) pour obtenir une imagerie optique super-résolue. Comparés aux marqueurs fluorescents, les NPMs offrent des nombreux avantages. Notamment, la cohérence de la lumière diffusée par ces nanoparticules permet leur détection interférométrique et donc l'obtention d'une image volumétrique. En outre, elles présentent une grande section efficace de diffusion (à la longueur de résonance plasmon de la particule) et permettent une grande stabilité des signaux diffusés grâce à leur réponse linéaire au champ électromagnétique incident (absence d'effet de désactivation, saturation ou photoblanchiment comme dans le cas des fluorophores). Ces nanoparticules sont donc d'excellentes candidates pour sonder des distributions de champs optiques à l'échelle nanométrique.

Ce manuscrit est structuré en quatre chapitres. Le premier chapitre introduit le principe général de l'holographie numérique hétérodyne (en Anglais Digital Heterodyne Holography, DHH).Dans un premier temps, cette technique est appliquée à l'imagerie plein champ de la lumière diffusée par des nano-antennes plasmoniques en champ lointain. Les structures à l'étude étaient des chaines de nano-trous percés dans une couche d'or de 50 nm d'épaisseur via lithographie électronique. Les paramètres comme le nombre de trous de la chaine, leur diamètre et la distance entre les trous ont été ajustés afin d'obtenir une structure résonante à la longueur d'onde utilisée par notre système holographique (dans cette expérience en particulier, $\lambda = 660$ nm). Afin d'illustrer la validité de la DHH pour l'obtention de diagrammes de rayonnement de ces nanostructures résonantes, nous avons comparé nos mesures holographiques avec des mesures de microscopie de champ proche à balayage (Near-field Scanning Optical Microscopy, NSOM). Nos résultats expérimentaux montrent comment, malgré la résolution limitée par la diffraction de notre système holographique plein champ, on peut facilement obtenir par DHH des informations importantes à propos des nanostructures résonantes, et ce de façon non invasive. L'intérêt de l'information tridimensionnelle ainsi que l'étude de la phase du champ diffusé sont mis en avant pour améliorer la compréhension de telles nanostructures.

Le deuxième chapitre décrit le cas particulier de la diffusion optique par des nanoparticules métalliques (toujours inférieures à 100 nm de diamètre), introduisant les concepts fondamentaux à l'origine de ce processus, notamment la présence de la résonance plasmon qui donne à ces nano-objets une section efficace de diffusion importante. Cette réponse optique est ensuite utilisée pour élucider des processus de modifications chimiques des nanoparticules d'argent en contact avec une électrode en or, grâce à l'étude simultanée de ces NPMs via électrochimie et holographie. Ces expériences ont été effectuées à l'intérieur de chambres microfluidiques dont l'une des surfaces était recouverte d'une couche d'environ 70 nm d'or utilisée comme électrode. En particulier, nous avons montré comment le couplage entre ces deux techniques apporte des informations complémentaires sur la nature des nanoparticules à l'étude. D'un côté, les expériences d'électrochimie permettent l'étude de l'oxydation d'un ensemble de nanoparticules d'argent en contact avec l'électrode. De l'autre côté, les images holographiques permettent d'élucider le comportement des nanoparticules en suspension dans tout le volume de la chambre microfluidique, tout en permettant la détermination précise de leur taille par des calculs de déplacement quadratique moyen (mean square displacement, MSD). De plus, l'holographie permet de détecter d'autres transformations chimiques telles que la dissolution des particules, qui ne sont pas mesurables par électrochimie car ce type de processus n'impliquent pas d'échange de charge électrique entre la particule et l'électrode.

Le chapitre trois, qui constitue le centre de ce travail, étudie la capacité de la méthode de DHH pour l'imagerie de super-résolution. La première partie examine les performances de cette technique en termes de précision de localisation sur des nanoparticules immobiles. Une estimation théorique de cette précision montre qu'elle dépend principalement du nombre de photons détectés par particule. Une seconde partie est centrée sur la localisation de particules en mouvement, de manière à obtenir une information 3D par l'accumulation des données de localisation de particules uniques obtenues à différents positions et divers instants. La question de la rapidité des algorithmes a été également abordée, conduisant à l'utilisation de cartes graphiques (Graphic Processing Unit, GPU) pour la parallélisation du traitement des hologrammes et la superlocalisation des particules, réduisant le temps de calcul à moins d'une seconde là où les algorithmes séquentiels classiques requièrent plusieurs dizaines de secondes.

Enfin, le chapitre quatre porte sur les premières démonstrations expérimentales de reconstitution d'images 3D pour la caractérisation des distributions d'intensité optiques utilisant le suivi de nanoparticules métalliques. Le premier exemple choisi démontre la reconstitution d'une onde évanescente, qui devient accessible en champ lointain par DHH grâce à la présence des nano-diffuseurs métalliques en mouvement agissant comme des sondes locales multiples. La distribution d'intensité d'un faisceau laser focalisé sous incidence oblique est ensuite imagée en 3D, mettant l'accent sur la grande étendue axiale qui peut être imagée par cette technique. Enfin, nous avons revisité la question centrale de ce travail à long terme : l'utilisation de cet outil pour explorer des concentrations de champs proches optiques aux abords de nanostructures plasmoniques avec une résolution nanométrique. Un problème majeur apparait à l'issue de cette question, qui est la lumière diffusée vers le champ lointain par la nanostructure plasmonique elle-même. Diverses stratégies de filtrage ont été explorées pour la différentiation de cette lumière parasite par rapport à la lumière diffusée par les sondes locales en mouvement. En particulier, des expériences reposant sur un filtrage hétérodyne de la lumière diffusée par les structures statiques montrent des premiers résultats très encourageants.

Contents

Introduction

The use of nanostructured systems, ranging from simple fluorescent molecules to sophisticatedly nanofabricated devices, has considerably spread in recent years, either for the imaging of living cells and tissues or for technological applications such as nanoelectronics. In parallel, a great deal of attention is devoted to advancing the field of optics on the nanometer scale. The diffraction of light in conventional optical microscopes, however, hampers our ability to selectively address nanoscale features separated by less than half the wavelength of light. Numerous strategies have been proposed to overcome this fundamental limit, many of them relying in turn in nanosystems to make this tiny world visible to the eye. Indeed, nanosystems offer interesting possibilities as local probes of their surrounding environment. It is the case of single-molecule studies in Biology, for example, which use nanoscopic markers to study cellular processes with nanoscale precision. Such is the case as well for Near-Field Scanning Optical Microscopies (NSOM) [48], which are able to unravel strongly confined electromagnetic fields with nanometer resolution by using nanoscopic probes.

Most superresolution imaging techniques, however, manage to achieve a resolution enhancement at the expense of other performances: long acquisition times, denaturation of the sample under study, difficult experimental implementation or high sample specificity, among other disadvantages. Particularly, for superresolution optical field mapping, crucial for plasmonic sensing [80] or SERS studies [101], the lack of local characterization techniques usable in water-based systems is a key issue. Analysis techniques involving electrons as probes are unsuited as they need to operate in vacuum environments, while scanning optical probes used by NSOM suffer from strong damping of mechanical oscillations when working in liquids. A large range of studies in microfluidics or in the emerging field of opto-fluidics would greatly benefit from the availability of high resolution imaging techniques.

Techniques using fluorescent markers such as PALM [15] and STORM [74] are nevertheless capable of imaging in liquid environments with excellent accuracies and are extensively used for imaging in biological media. They are based on single-molecule localization methods, obtaining outstanding position accuracies by pointing the center of mass of the diffraction pattern of individual fluorescent probes. However, although these methods rely on optics for detection, few of them have been used to image electromagnetic fields, i.e. to retrieve an optical information with subwavelength resolution. Yet, for this purpose, the use of fluorophores presents some disadvantages, since the fluorescence intensity can suffer from non-linear effects such as saturation, photo-bleaching and quenching. In addition, the extension of these methods to 3D imaging [43] is still limited to a few micrometers in depth.

Some years ago, our laboratory applied the technique of (off-axis) digital heterodyne holography (DHH) to the characterization of the field scattered by plasmonic nanoobjects. Using this interferometric technique, Suck *et al.* [82, 83] were able to recover the whole 3D information carried by the scattered light, particularly establishing a clear distinction between resonant and non-resonant nanoantennas in the far field. Moreover, the angular scattering pattern of the nanostructure could be obtained from a single snapshot. Although being diffraction-limited, DHH was therefore shown to be capable to extract relevant information about nanoscopic systems.

DHH was also shown by our research group, among others, to be well adapted to the detection of weakly scattering nanoobjects [8, 50]. Owing to its excellent sensitivity [36], this technique was successfully applied to image and localize metal nanoparticles of 50 nm diameter in three-dimensions, either for fixed particles spin coated on a glass substrate or in free motion within a water suspension [4, 91]. Besides, it was shown that gold nanobeads, functionalized and fixed on the membrane of living cells, could be detected by DHH in order to obtain a three-dimensional image of the cell surface [44, 100].

In this thesis work, the main motivation has been to turn this far-field, wide-field, 3D imaging technique into both a superresolution technique and a near-field imaging technique. To do so, we have used metallic nanoparticles (MNPs) undergoing Brownian motion as stochastic local field probes that we have localized in three-dimensions in order to overcome the diffraction limit. The technique we propose here is therefore a combination of the concepts of superlocalization and NSOM microscopies. Beyond simple localization, the gold markers can actually be envisaged as extremely local electromagnetic field probes, able to couple light into the far-field. Instead of scanning the probe across the sample under study (like do NSOM techniques), we propose here to use probe particles at low concentrations and allow them to move randomly in the imaged volume: given sufficient time, these probes stochastically visit each (or most) voxel(s) of the investigated volume. In addition, the coherent light scattering by MNPs allows the direct extension of these methods to 3D imaging, with an unprecedentedly large depth range.

This work is organized as follows: **Chapter 1** starts out by providing an introduction to digital heterodyne holography, as well as the basics of numerical reconstruction. Particularly, we depict our holographic microscope setup and detail the specific reconstruction algorithm used throughout this thesis work. In the context of previous work in our group, we present a further validation of DHH measurements for the study of plasmonic nanoantennas in the far-field by comparing them to measurements performed with a well-established technique in the field: aperture NSOM (aNSOM).

We then proceed, in **Chapter 2**, with the discussion of the electromagnetic response of nanoparticles to an incident light, addressing the main phenomena of light scattering and absorption. We particularly study the case of MNPs, for which a resonant response known as Localized Surface Plasmons can arise, giving them relatively large scattering cross sections. By imaging this scattered light, we finally show the capabilities of our holographic microscopy setup to explore the behaviour of silver NPs in solution, as well as to elucidate their chemical transformations in contact with a gold electrode by coupling our technique to electrochemical measurements.

To set the basis for further discussion, in **Chapter 3** we analyse the smallest resolution that can be achieved by localization methods. We first review various wide-field sub-diffraction microscopy techniques based on single-particle localization, giving particular attention to the recent achievements of digital holographic microscopy in this field. Then we present different strategies that have been proposed not only towards the tracking and dynamic study of single sub-diffraction objects, but also for superresolution imaging obtained point-by-point by accumulating data from thousands of individual localizations. This leads us to introduce our approach: the 3D imaging of MNPs undergoing Brownian motion to stochastically probe a certain volume under study. Besides, we study by statistic means the minimum time necessary to recover a 2D image with our stochastically moving particles. Finally, we complete our discussion with a technical section about our fast particle detection algorithm, based on parallel calculations using a Graphics Processing Unit.

Chapter 4 then deals with the central question of this PhD work, that is to use gold nanoparticles as local EM field probes. After a brief discussion about the concepts of near-field and evanescent waves, we illustrate the near-field imaging potential of our holographic system by imaging the evanescent wave decay in a Total Internal Reflection (TIR) configuration. Then, highlighting the large 3D volume that can be imaged with our technique, we reconstruct the intensity profile of a focused Gaussian laser beam inside a microfluidic chamber. However, some key issues remain when trying to characterize the electromagnetic field distribution around plasmonic nanostructures with subwavelength resolution using MNPs. The light scattered to the far field by the plasmonic object itself degrades the detection of the metallic nanoprobes. Two filtering methods are therefore presented, relying on the differentiation of each type of scattering: that from static, generally bigger features, from the scattering of small moving NPs. The preliminary results are discussed as well as further possible improvements.

View of Boston, 1860
An early stereoscopic card for 3D viewing

Chapter 1

Holographic microscopy for far-field optical mapping

Holography is an interferometric technique for the three-dimensional characterization of the wavefield diffracted by an object upon illumination by a coherent incident wave. It was invented by physicist Dennis Gabor in 1948 [32] while trying to enhance the resolving power of electron microscopes. The development of the laser in the early 1960s provided suitable coherent illumination sources enabling the rise of optical holography.

In the beginning, holograms were recorded on a photographic plate that needed to be chemically developed. Later improvements in large photosensitive detectors arrays such as CCD (Charge-Coupled Device) and CMOS (Complementary Metal Oxide Semiconductor) cameras, associated to an increase in computing power, made possible its digital and dynamic implementation for many industrial purposes such as deformation measurements and vibrometry [89, 90, 94], flow visualization [95], removal of wavefront distortions in optical communications [67] and high density data storage [46], among others.

In this chapter, we first introduce the principles of digital holography, as well as the basics of numerical reconstruction. Particularly, we depict our holographic microscope setup and detail the specific reconstruction algorithm used throughout this thesis work. Finally, we show how holographic microscopy can be used for the characterization of plasmonic structures and, notably, to image the three-dimensional scattering pattern of nanoantennas in the far-field, from a single snapshot.

1.1 Principles of digital holography

Holography is based upon diffraction and interference principles: the amplitude and phase of the diffracted wavefield under study are encoded owing to its interference with a well-known local oscillator, which is usually called the reference wave. The resulting interference pattern is referred to as the hologram and corresponds to a fringe-like intensity distribution. The analytical expression of the recorded intensity at the detector plane can be written as the square modulus of the sum of the two complex fields:

$$\begin{aligned} I_H(x,y,z_p) &= |E_H(x,y,z_p)|^2 \\ &= |E_R(x,y,z_p) + E_S(x,y,z_p)|^2 \\ &= E_R^* E_R + E_S^* E_S + E_R E_S^* + E_R^* E_S \end{aligned} \tag{1.1}$$

where E_R and E_S are the complex field of the reference and the scattered wave, respectively, and z_p indicates the position of the recording plane, perpendicular to the optical axis. The first two terms in the last equation correspond to the reference and scattered intensities (also called *autocorrelation terms*, or *0 order*) and do not contain any phase information. The last two terms are the conjugate of each other ($E_R E_S^*$, *-1 order* also called the *twin image* of $E_R^* E_S$, *+1 order* or *virtual image*) and, conversely to the first two terms, both carry the whole information about the unknown complex scattered field under study.

Historically, in the experimental configuration that was first proposed, later called in-line holography, the interferences took place between the light scattered by a weakly scattering object (semitransparent) and the strong coherent background due to the direct transmission of the incident light through the object itself (see Fig. 1.1). Consequently, all four terms from Eq. 1.1 were recoded in the hologram plane and the reconstruction of the scattered field E_S was deteriorated by the autocorrelation components and the twin image which overlapped with the signal image. In the following section, we present two techniques enabling us to suppress these undesired diffraction orders from the recorded interference.

1.1.1 Experimental suppression of parasite diffraction orders

Off-axis holography

In 1964 Leith and Upatnieks [51, 52] proposed to divide the incident illumination wave into two separate arms and to introduce a small tilt θ_R in the reference beam (see Fig. 1.2), so that $k_R = k_{R_x} + k_{R_z}$ and $k_{R_x} = k \sin\theta_R$. For simplicity, we define the recording

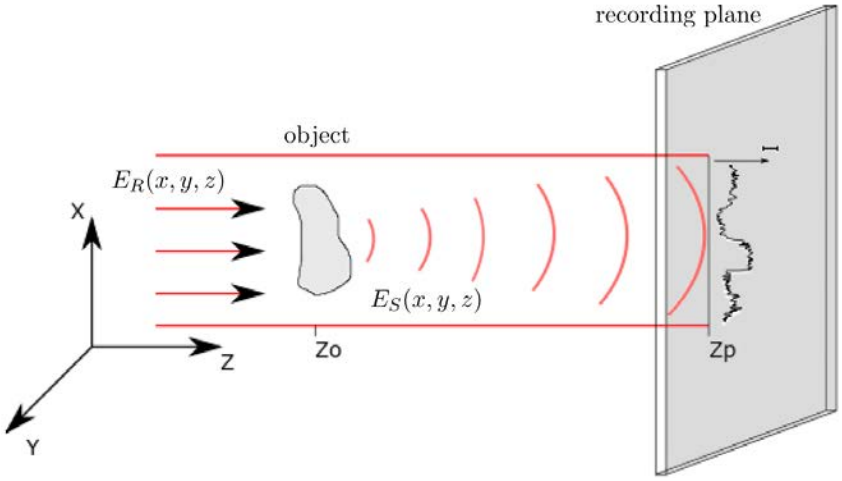

FIGURE 1.1: In-line holography configuration scheme. Interference takes place between the light scattered by a weakly scattering object (semitransparent) and the strong coherent background due to the direct transmission of the incident light through the object itself.

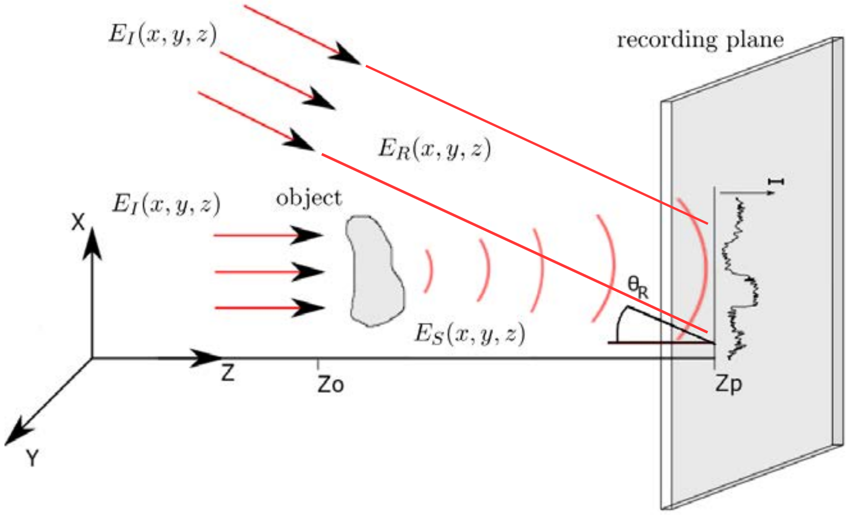

FIGURE 1.2: Off-axis holography configuration scheme. The propagation direction of the reference wave E_R is tilted by an angle θ_R with respect to the optical axis.

plane as $z = 0$. The small angle between the two beams transforms Eq. 1.1 as follows:

$$\begin{aligned} I_H(x,y) &= |E_R(x,y)e^{-ikx\sin\theta_R} + E_S(x,y)|^2 \\ &= \Big(I_R + I_S(x,y)\Big) + e^{ikx\sin\theta_R}E_R^*E_S(x,y) + e^{-ikx\sin\theta_R}E_RE_S^*(x,y) \end{aligned} \tag{1.2}$$

where $k = 2\pi/\lambda$. Note that the z-component of the reference wave vector introduces a constant phase shift on the hologram plane $k_{R_z} = k\cos\theta_R$ that can be ignored. In this case, the different terms vary at different spatial frequencies and therefore they will split in the Fourier space. In other words, the phase delay in the real space induces a simple shift in the spatial frequency domain. Consequently, the +1 order can be numerically selected by computing the spatial Fourier transform of our hologram $\tilde{I}(k_x, k_y) = \mathcal{F}[I_H(x,y)]$ and we obtain:

$$\tilde{I}_H(k_x, k_y) = \tilde{I}_R + \tilde{I}_S(k_x, k_y) + E_R^* \tilde{E}_S(k_x + k\sin\theta_R, k_y) + E_R \tilde{E}_S^*(k_x - k\sin\theta_R, k_y) \quad (1.3)$$

Figure 1.3 represents the four terms obtained in Eq. 1.3 in the spatial frequency domain along the k_x axis. The first term, $\tilde{I}_R$, corresponds to the spectrum of the reference wave, assumed to be uniform. Its Fourier transform is thus a Dirac peak centred at 0 in Fig. 1.3. The second term, $\tilde{I}_S$, is the intensity spectrum of the scattered wave and its width is twice the spectral width of E_S, which we write as $2\Delta k$ and is also centred at 0. The last two terms in Eq. 1.3 also have a spectral width equal to Δk but are frequency shifted towards $\pm k\sin\theta_R$. They are represented by the two side lobes in Fig. 1.3.

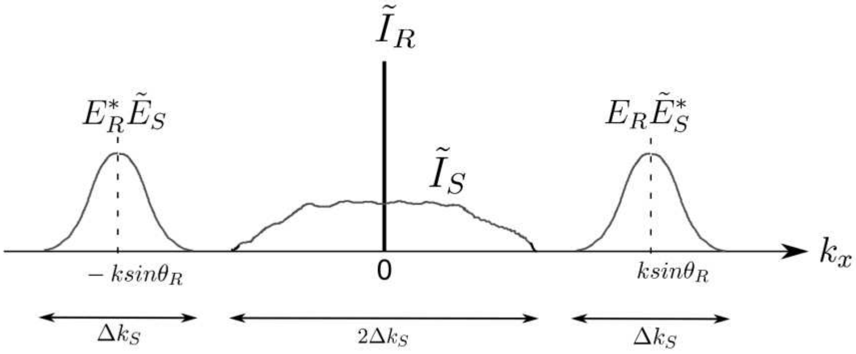

FIGURE 1.3: Representation of the diffraction orders splitting in the Fourier space.

Phase-shifting Holography

In 1997, Yamaguchi and Zhang [102, 103] proposed another strategy to retain only the +1 diffraction order that was independent of the geometry of the setup (valid for either in-line or off-axis configuration). It consists in the combination of multiple images acquired with different phase shifts introduced between the reference and the object beams, in order to extract only the relevant $E_R^* E_S$ term.

If we denote as ϕ the relative phase between the reference and the object arm at the detector plane, the hologram intensity can now be written as:

$$I_H(x,y)^{(\phi)} = I_R + I_S(x,y) + e^{i\phi} E_R^* E_S(x,y) + e^{-i\phi} E_R E_S^*(x,y) \quad (1.4)$$

Several strategies can be implemented to appropriately sample this phase shifted holograms. Nyquist-Shannon's sampling theorem states that more than two images are necessary to correctly measure the hologram modulation. Consider a phase-shift set to $\phi = \frac{\pi}{2}$ between two snapshots on a series of four successive acquisitions (what is called a 4-phase demodulation method): we obtain four different holograms, referred as $I_H^{(n\pi/2)}$, where n is an integer going from 0 to 3. The following linear combination of these 4 images allows us to extract the term $E_R^* E_S$:

$$\begin{aligned} I_H &= \frac{1}{4}[(I_H^{(0)} - I_H^{(\pi)}) + i(I_H^{(\pi/2)} - I_H^{(3\pi/2)})] \\ &= E_R^* E_S \end{aligned} \tag{1.5}$$

$N = 4$ images is a simple case, but for a more general case of a N-phases demodulation, the phase-shift that needs to be imposed between two successive snapshots is $\phi_n = \frac{2\pi n}{N}$ with n being an integer going from 0 to $N-1$, from a series of N acquisitions. The linear combination that allows the suppression of all the diffraction terms except from the +1 order is:

$$\begin{aligned} I_H &= \frac{1}{N} \sum_{n=0}^{N-1} e^{i\phi_n} I_H^{(\phi_n)} \\ &= \frac{1}{N} \underbrace{\left[\sum_{n=0}^{N-1} e^{\frac{4i\pi n}{N}} \right]}_{=0} (I_R + I_S) + \frac{1}{N} \underbrace{\left[\sum_{n=0}^{N-1} e^{\frac{4i\pi n}{N}} \right]}_{=0} E_R E_S^* + E_R^* E_S \\ &= E_R^* E_S \end{aligned} \tag{1.6}$$

The main disadvantage of this technique is, however, the need to acquire multiple images, which slows down the acquisition rate.

Off-axis Digital Heterodyne Holography (DHH)

Gross and Atlan [36] first proposed in 2007 to combine the two strategies previously detailed to remove aliases, associating both off-axis geometry and phase-shifting holography in a single experimental setup. This double filtering in both the spatial and the frequency domain enables the recording and reconstruction of holographic images at very low light levels. The scope of this work being the imaging of nanoobjects, this low noise configuration is currently used by our group.

To better illustrate this double filtering process in both the spatial and temporal frequency domains, Fig. 1.4 shows the image obtained by performing a spatial Fourier transform of one our our holograms. In (a) we can see the splitting of the three diffraction orders due to the off-axis configuration. In (b), phase shifting has been added and a better filtering is obtained by calculating a linear combination of four successive images with a relative phase-shift of $\pi/2$. Especially, the zero-order term in the middle of the k-space is largely removed in (b) as compared to (a), which reduces the overlap between the zero-order and the +1 order containing E_S. In order to remove efficiently the parasitic diffraction orders, we apply digitally an additional circular mask to select only the +1 order. This diffraction order is then recentred, which effectively cancels the spatial frequency shift induced by the off-axis geometry. Note that, for a given CCD detector area, off-axis holography suffers from a four-fold loss in resolution with respect to in-line holography, as we finally use only one quarter of the detector surface. However, although phase shifting holography is an powerful technique for noise reduction when imaging static samples, it is not always well-suited when imaging moving objects. As we further discuss in Chapter 3, the minimal acquisition delay between two frames (which is driven by our camera transfer time) is, in some cases, too long with respect to the object mean displacement during the same time-lapse, which can blur the object reconstruction. In this work, either 1, 2 or 4-phase schemes have been used depending on the objects under study.

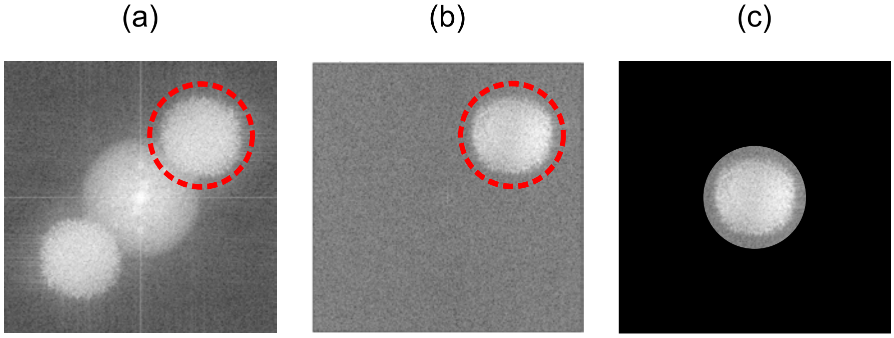

FIGURE 1.4: Double filtering in the Fourier space. (a) Splitting of the three diffraction orders due to the off-axis configuration. (b) Additional phase shifting and 4-phase demodulation of the same hologram. (c) Recentring of the +1 order containing the relevant $E_R^* E_S$ term in order to cancel the effect of off-axis geometry.

1.1.2 Experimental setup

Throughout my thesis work, I have contributed to the implementation of two different Olympus microscopes: an upright BX-URA2 and an inverted IX-71, equipped with various microscope objectives. With few differences between the two setups around each microscope, the overall holographic configuration is sketched in Fig. 1.6. Long coherence length lasers (a single mode laser diode and a diode pumped solid-state laser) were used in order to avoid arm length compensation adjustments. We used two different wavelength: $\lambda = 532$ nm and $\lambda = 660$ nm. Both the illumination source and the microscope objective will be detailed before each experiment.

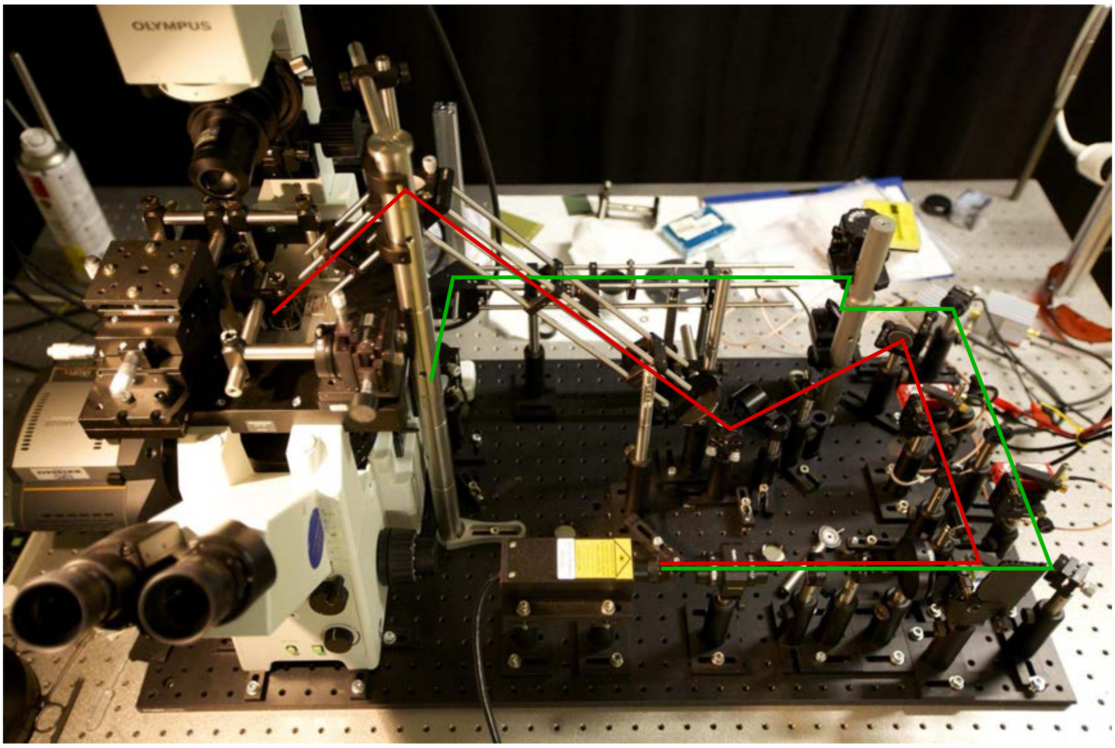

FIGURE 1.5: Inverted microscope Olympus IX71.

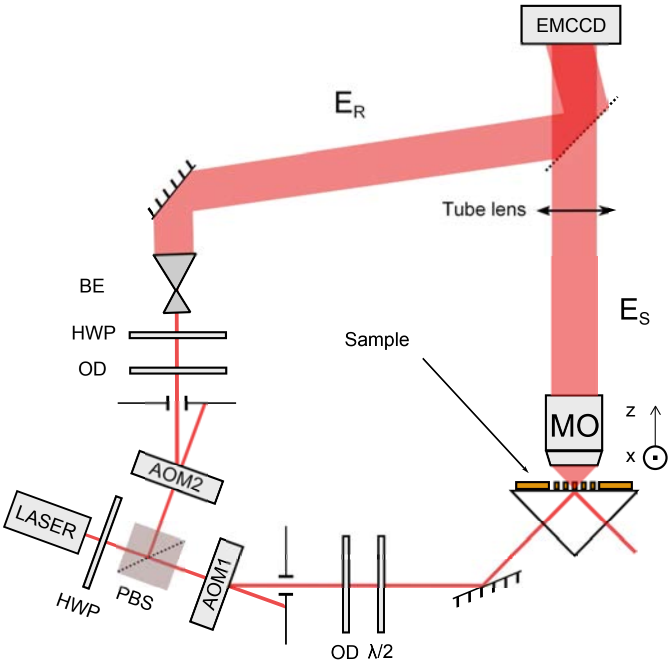

FIGURE 1.6: Setup scheme.

First, the excitation laser beam is split with a polarizing beam splitter (PBS) in a reference and an illumination arm in a Mach–Zehnder configuration manner. A first $\lambda/2$ waveplate (half wave plate, HWP) and variable optical densities (OD) allow the control of the optical power in each arm. Additional HWPs in each arm allow us to adjust the polarization state impinging the sample as well as to maximize the holographic modulation depth by aligning the polarization iof E_S and E_R. The reference beam passes through a beam expander (BE) so that it covers the whole detector surface. In the object arm, the sample is illuminated under total internal reflexion (TIR) using a glass prism, ensuring dark-field illumination. Thus, only the field scattered by the structures under study is collected by the microscope objective (MO) and reaches the EMCCD camera (Andor iXon3 885, cooled at 10°C, up to 40 Hz acquisition rate for 512 × 512 images, square pixels of 8 μm) and it interferes with the reference beam in an off-axis configuration.

Finally, we have the possibility to introduce an accurate phase-shift between the two arms. For that, we use acousto-optic modulators working at frequencies in the MHz range. Such a high frequency modulation is unfortunately too fast for existing digital cameras. One solution, which we use in our setup, consists in frequency-shifting both arms by two acousto-optic modulators (AOM1, AOM2) at frequencies $f_{AOM1} = 80$ MHz and $f_{AOM2} = 80\ \mathrm{MHz} - \Delta f$, with Δf values of a few tens of Hz, within the acquisition rate of the camera. The resulting interference pattern thus bears a modulation at a beating frequency $\Delta f = f_{AOM1} - f_{AOM2} = \Delta f$, while the acquisition rate is set to $f_{CCD} = 4\Delta f$ in order to perform a frequency filtering by means of a four-phase demodulation method. Each holographic image is then reconstructed from a sequence of four consecutively phase-shifted intensity images.

1.1.3 Digital reconstruction process

As mentioned in the introduction, holography consists in recording the optical field diffracted by an object at *a certain* distance from it. Numerical calculations to retrieve the optical field emerging from the object at *any* distance from a single hologram is what is called the reconstruction process. There exist a number of different approaches [92] to calculate the backward propagation of light from the hologram to the reconstruction plane, all based on diffraction theory.

The field scattered by the object in any given plane can be written using the Kirchhoff diffraction integral:

$$E(x', y', z) = \frac{1}{i\lambda} \iint_{-\infty}^{+\infty} E(x, y) \frac{e^{ikr}}{r} \cos(\mathbf{n}, \mathbf{r})\ \mathrm{d}x\mathrm{d}y \tag{1.7}$$

where (x', y') and (x, y) denote the spatial coordinates in the hologram and the object plane, respectively (see Fig. 1.7). This expression can be understood as the addition (integral) of spherical secondary waves coming from every point in the object as stated by the Huygens principle. The factor $1/i\lambda$ is a phase and amplitude factor, and $\cos(\mathbf{n}, \mathbf{r})$ is a polarization factor.

Since the direct numerical processing of the Kirchhoff integral is time consuming, more efficient computational schemes have been developed. In the paraxial limit, i.e. for reconstruction distances much larger than the object dimensions, expression 1.7 can be simplified, leading to a single fast Fourier transform (FFT) calculation, know as the Fresnel approximation. This alternative is unfortunately not suitable for microscopy images, as the reconstruction distances are of the order of the dimensions of the objects and angular collection apertures are too large for the paraxial approximation to remain valid. Moreover, in this approach, coordinates in the reconstruction plane scale linearly with the distance to the object. Consequently, the reconstruction of a thick object leads to a distorted image.

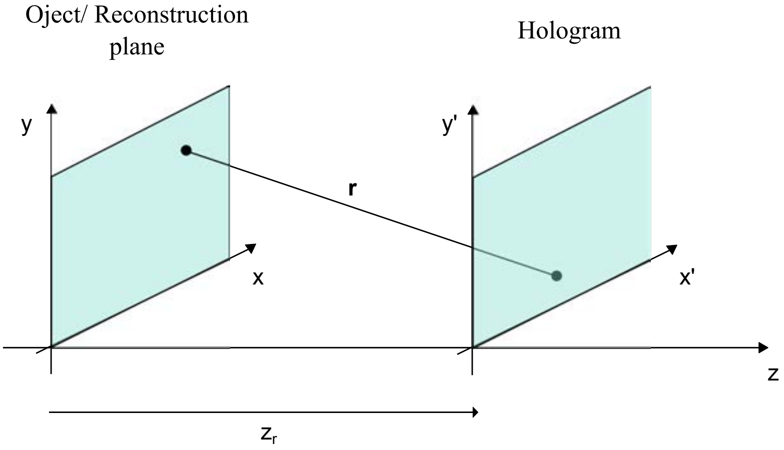

FIGURE 1.7: Coordinate system.

As a result, methods using more than one FFT are more suitable. The so-called "Three-FFT Algorithm" is based on convolution methods: the field at the recording plane can be understood in this approach as the convolution between the field at the object plane and the impulse response of the system, $h_z(x, y)$. The field scattered by the object in any given plane can now be written as:

$$E(x', y', z) = E(x, y, 0) * h_z(x, y) = \iint_{-\infty}^{+\infty} E(x, y, 0) h_z(x' - x, y' - y)\ \mathrm{d}x\mathrm{d}y \tag{1.8}$$

The $h_z(x, y)$ impulse response function, analogous to the Huygens secondary wavelets, can take many forms depending on the chosen approximations. It is possible to link

Fourier-based approaches and convolution methods by writing, for instance:

$$h_z(x'-x, y'-y) = \frac{1}{i\lambda}\frac{e^{ikr}}{r}\cos(\mathbf{n}, \mathbf{r}) \tag{1.9}$$

where $r = |\mathbf{r}| = \sqrt{z^2 - (x'-x)^2 - (y'-y)^2}$. In the Fourier domain, it is easy to see that Eq. 1.8 becomes:

$$E(x', y', z) = \mathcal{F}^{-1}[\mathcal{F}\{E(x, y, 0)\} \times \mathcal{F}\{h_z(x, y)\}] \tag{1.10}$$

therefore involving the calculation of three Fourier transforms.

Angular spectrum method

A better compromise for us is yet a third approach, known as the angular spectrum method, which involves two FFTs and does not require any approximations to reach a simple computational expression. It consists in a mathematical representation in which an optical field in a homogeneous medium can be described as a superposition of plane waves with variable amplitudes and propagation directions.

Let us assume that we know the field distribution at the object plane $E_S(x, y, 0)$, the z axis being the optical axis. The field amplitude for every spatial frequency of the object (i.e., its spectrum) can be expressed as:

$$A_0(k_x, k_y) = \mathcal{F}\{E(x, y, 0)\} = \iint_{-\infty}^{+\infty} E_S(x, y, 0)e^{i2\pi(k_x x + k_y y)}\mathrm{d}x\mathrm{d}y \tag{1.11}$$

Accordingly, the inverse Fourier transform of Eq. 1.11 reads as:

$$E(x, y, 0) = \mathcal{F}^{-1}\{A_0(k_x, k_y)\} = \iint_{-\infty}^{+\infty} A_0(k_x, k_y)e^{-i2\pi(k_x x + k_y y)}\mathrm{d}k_x\mathrm{d}k_y \tag{1.12}$$

We consider now a simple plane wave $e^{ik_z z_r}$, with a known amplitude at $z = 0$ along the plane $(x, y, 0)$ that propagates until the recording plane (x, y, z_r) at a distance z_r from the original plane. This free-space propagation simply leads to a phase change of the field that can be expressed by multiplying $E(x, y, 0)$ by this propagation term $e^{ik_z z_r}$:

$$E_S(x, y, z_r) = E_S(x, y, 0)e^{ik_z z_r} = E_S(x, y, 0)e^{i\sqrt{k^2 - k_x^2 - k_y^2}z_r} \tag{1.13}$$

Taking into account all the different plane waves in which the field has been decomposed, we obtain:

$$E_S(x, y, z_r) = \iint_{-\infty}^{+\infty} A_0(k_x, k_y)e^{i2\pi(k_x x + k_y y)}e^{i\sqrt{k^2 - k_x^2 - k_y^2}z_r}\mathrm{d}k_x\mathrm{d}k_y \tag{1.14}$$

If we denote $A_{z_r}(k_x, k_y)$ the spectrum of the scattered field at the recording plane (i.e. the spectrum of the hologram), in analogy to Eq. 1.13 we have:

$$A_{z_r}(k_x, k_y) = A_0(k_x, k_y)e^{i\sqrt{k^2-k_x^2-k_y^2}z_r} \tag{1.15}$$

and we can simplify Eq. 1.14 as follows:

$$E_S(x, y, z_r) = \mathcal{F}^{-1}\{A_{z_r}(k_x, k_y)\} \tag{1.16}$$

Eq. 1.16 shows that, using the angular spectrum method, only two FFTs need to be computed: a first Fourier transform of the hologram, that we can then propagate to any z-plane through multiplication by a pure imaginary propagation term, prior to computing a second Fourier transform (inverse FT) to obtain the scattered field in that particular plane, as illustrated in Fig. 1.8.

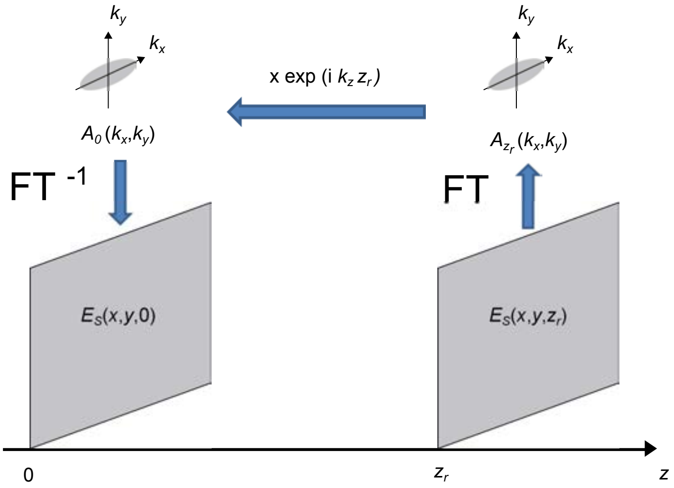

FIGURE 1.8: Angular spectrum method, also called “Two-FFT Algorithm”.

Practical implementation of the reconstruction process

Fig. 1.9 depicts the different steps of our numerical reconstruction process, detailed here:

Step 1. Numerical correction of the signal wave sphericity: the hologram I_{ccd} is multiplied by a complex phase matrix, M, to compensate for the sphericity induced by the microscope tube lens both on the signal wave and the reference wave:

$$M(x, y, d) = exp\Big(\frac{i\pi(x^2 + y^2)}{\lambda d}\Big) \tag{1.17}$$

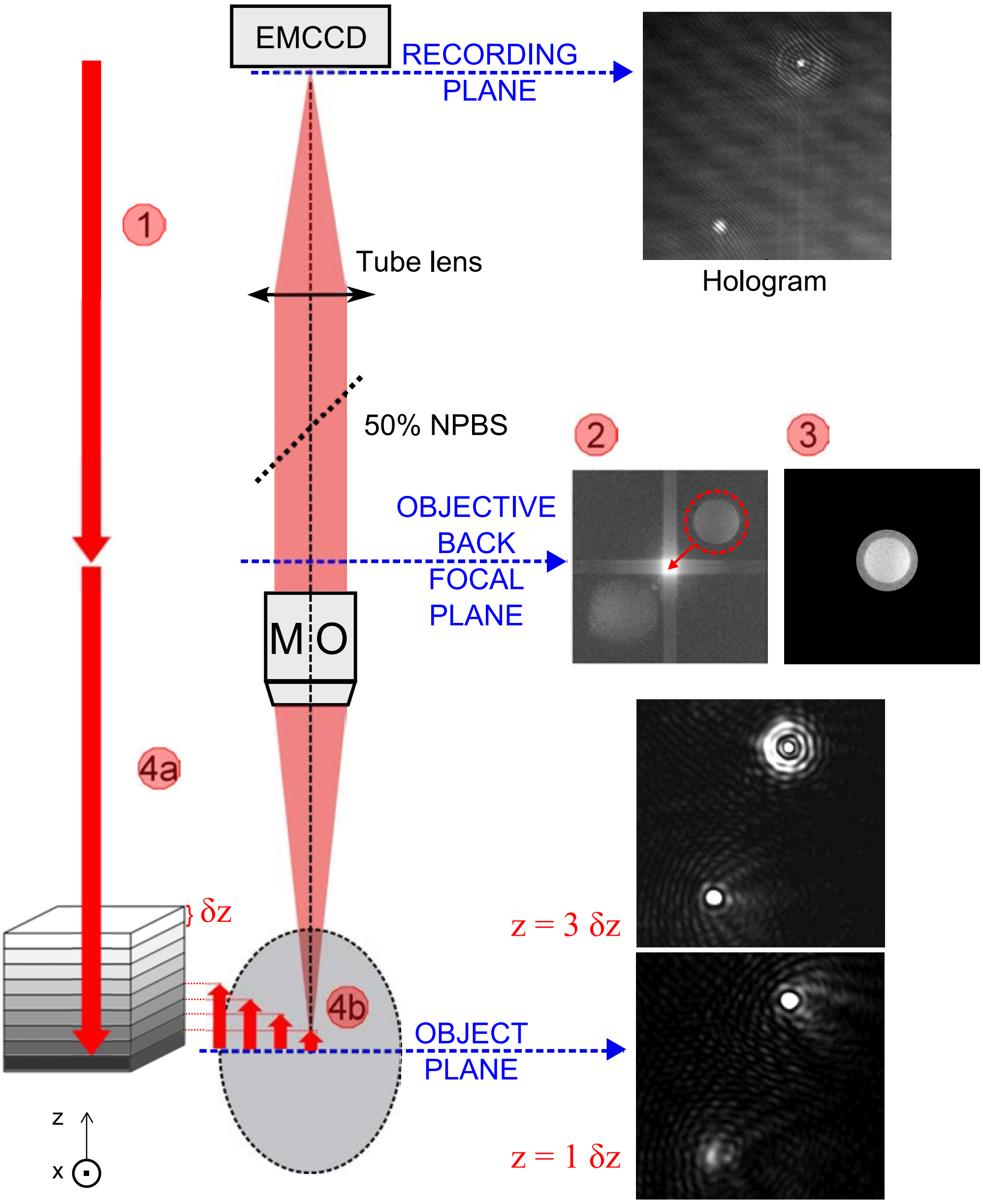

FIGURE 1.9: Practical implementation of the numerical reconstruction process. The number in circles correspond to the different steps of the reconstruction algorithm.

where d is the local radius of curvature of the wave on the CCD plane. If the reference wave was a plane wave after the tube lens, the distance d would simply be the virtual distance between the recording plane and the back focal plane of the objective trough the tube lens.

Step 2. First FFT (Fast Fourier Transform): the discrete Fourier transform of the corrected hologram is calculated:

$$\tilde{H}(k_x, k_y) = FFT[I_{ccd} \times M] \tag{1.18}$$

Step 2 in Fig. 1.8 shows the intensity $|\tilde{H}|$ in the k-space, in logarithmic scale, in the case where there is no phase-shifting between the object and the reference. For particles in motion, we need to implement different strategies for noise reduction (see Chapter 3 for further discussion). The term related to E_S is at the top-right corner, centred on the spatial frequency induced by the off-axis geometry. At this step, the calculation is equivalent to the one-FFT reconstruction (Fresnel approximation presented earlier) of the hologram at the distance d described in the previous step. Since the back focal plane of our microscope objective coincides with the output pupil plane, which is common for high magnification objectives, what we see for this +1 order is the sharp reconstruction of the output pupil plane. Likewise, the virtual image term related to E_S^* is centred on the conjugate frequency (bottom-left corner). If we changed in Step 1 the parameter d to -d, the image of the output pupil would be sharp in the bottom-left corner, while the term related to E_S would be blurred. In the middle of $|\tilde{H}|$, the zero-order appears as a square instead of a circle because of the multiplication by the matrix M as well. Figure 1.4(a) shows an example in which no correction of the wavefront sphericity has been applied.

Step 3. Spatial filtering and centring: to remove the zero-order term and replace the term related to E_S in the middle of the Fourier plane, a round numerical filter is applied, which matches the output pupil of the objective. Since the shape of the pupil is sharp in the k-space, we can isolate precisely the pixels containing the signal, minimizing the loss of information. The filtered part is then translated to the middle of a 512 × 512 calculation grid in order to compensate the off-axis shift.

Step 4. Second FFT:

Step 4a: The back focal plane of an objective shows nothing more than the Fourier transform of the object placed in its object plane. Therefore, to reconstruct the field scattered at this plane, only one last step is needed, that is, an inverse Fourier transform.

Step 4b: In order to reconstruct any plane different from the objective focal plane, we need to multiply $\tilde{H}$ by a propagation matrix $\tilde{K}(k_x, k_y, z)$ of the form:

$$\tilde{K}(k_x, k_y, z) = exp(izk_z) = exp\Big(iz \times \sqrt{k_0^2 - k_x^2 - k_y^2}\Big) \tag{1.19}$$

where

$$k_0 = \frac{2\pi n}{\lambda},\ k_x = \frac{2\pi(x-256)}{512 \times \Delta_{pix}},\ k_y = \frac{2\pi(y-256)}{512 \times \Delta_{pix}} \tag{1.20}$$

to propagate the hologram by a distance z in the axial direction. Δ_{pix} is the magnified pixel size. Equations on 1.20 are suited for holograms of 512 × 512 pixels but are easy to generalize. Finally, as in Step 4a, the inverse FFT is calculated to recover the real-space image at the specific z-plane. For each hologram, this step is repeated n times (n being an integer) in order to get a stack of the scattered field at different depths, with a propagation step of δz:

$$H(x, y, n \cdot \delta z) = FFT^{-1}[\tilde{H}(k_x, k_y) \times \tilde{K}(x, y, n \cdot \delta z)] \tag{1.21}$$

Figure 1.9 shows reconstruction for $n = 1$ and $n = 3$, but any number of planes can be calculated to obtain a 3D stack of images.

1.2 Mapping optical fields with DHH

Among the numerous applications of off-axis DHH microscopy, in 2011 our group first addressed the characterization of plasmonic structures using this far field technique [82, 83]. Plasmonics is a branch of nanophotonics that is primarily concerned about the coupling of light to electronic charges in metals. Under specific illumination conditions, charge oscillations inside nanostructurated metals enable strongly localized field enhancements of subwavelength dimensions. This ability to squeeze light into subdiffraction volumes has stimulated many attractive applications such as extremely high sensitivity spectroscopy and sensing of chemical agents, novel drug-delivery designs, original strategies for high-resolution microscopy, compact metal-based waveguides for miniaturized photonic devices and more efficient solar cells, among others [80].

A characteristic fingerprint of plasmonic nanostructures is their ability to work as nanoantennas, being able to convert freely propagating optical radiation into strongly localized energy, and vice versa [66]. Therefore, in order to understand and exploit the plasmonic properties of nanostructures, it is fundamental to obtain the full knowledge of the three-dimensional electromagnetic field around a nanoobject interacting with a light source. Although being diffraction-limited, DHH microscopy has been shown to be a useful tool to image nanoantennas' three-dimensional scattering patterns from a single snapshot. In addition, just as with back focal plane microscopy [54], the angular radiation pattern can also be obtained straightforwardly by computing a simple Fourier transform of the hologram [82]. Heterodyning is indeed another driving force of DHH as it offers the possibility to perform phase measurements and to investigate frequency modulated phenomena, although it has not been the main purpose of my work, presented hereafter.

While our group first studies were mainly centred on establishing a clear distinction between resonant and non-resonant nanoantennas in the far field [83], the present work aims at further validating DHH measurements by comparing them to measurements performed with a well-established technique in this field, aperture Near-field Scanning Optical Microscopy (aNSOM). Particularly, working in collaboration with an NSOM research group from our laboratory, directed by Dr.Yannick DeWilde, we characterized the same nanoantennas using both imaging techniques.

Samples under study

Similar to nanodisk chains, series of disk-like nanoholes (see Fig. 1.10) can likewise present characteristic nanoantenna features (i.e. high directivity and enhanced scattering). Our samples were fabricated by thermal evaporation of a 2 nm thick Cr layer for adhesion, prior to a 40 nm gold deposition forming a thin, partially transparent layer. Several nanohole chains were drilled by electron beam lithography in a poly-(methylmethacrylate) resist and transferred into the metal layer by ionic beam etching. A set of different chains was fabricated by varying three parameters, in order to find nanostructures resonating at our laser wavelength ($\lambda = 660$ nm): the number of holes, the hole diameter and the edge-to-edge distance between holes. This was the case for chains composed of 17 nanoholes, 150 nm diameter, spaced by around 20 nm, for an incident polarization along the chain axis. The total length of the nanoantenna is about 3 μm. The nanofabrication was performed at the *Laboratoire Photonique et Nanostructures* facility by Dr. Nathalie Bardou and Dr. Stéphane Collin.

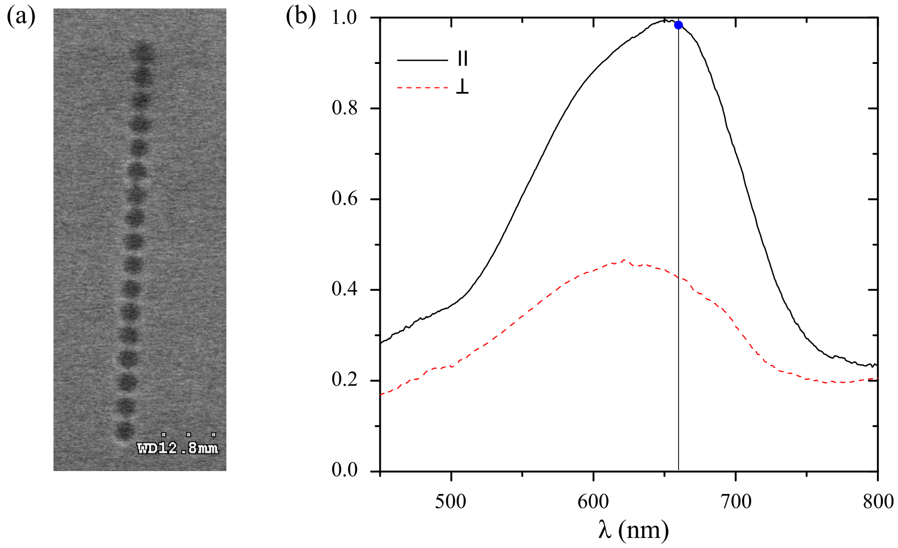

FIGURE 1.10: (a) SEM image of a Au nanohole chain consisting of 17 disks of 150 nm diameter and $\Delta = 30$ nm edge-to-edge spacing. (b) Corresponding far-field transmission scattering spectra obtained with an incident polarization along the chain axis (solid curve) and perpendicular to it (dashed curve). The blue dot indicates $\lambda = 660$ nm.

Experimental conditions

In both experimental setups, the light source is a single longitudinal mode laser diode ($\lambda = 660$ nm, $P_{max} = 120$ mW). For the holographic measurement, the reference E_R and the object arm E_O were frequency-shifted at frequencies $f_{AOM1} = 80$ MHz and $f_{AOM2} = 79,999996$ MHz. To avoid saturation of the sensor, the sample was illuminated under total internal reflexion (TIR), ensuring dark-field conditions. Only the field scattered by the nanostructures was then collected by the microscope objective (100× magnification, N.A.=0.8) and reached the EMCCD camera (Andor iXon3 885), where it interfered with the reference beam in an off-axis configuration. The resulting interference pattern was modulated at a beating frequency $\Delta f = f_{AOM1} - f_{AOM2} = 4$ Hz while the acquisition rate was set to $f_{CCD} = 4\Delta f = 16$ Hz in order to perform a frequency filtering by means of the four-phase demodulation method. Each holographic image shown in this section was thus reconstructed from a sequence of four consecutively phase-shifted holograms, acquired at the EMCCD plane with an exposure time of $\tau_{exp} = 1$ ms and subsequently numerically reconstructed to any plane.

The near-field measurements were performed with a modified commercial NSOM (WITec GmbH alpha300S, see Fig. 1.11) using a hollow silicon square-based pyramid with a nanoaperture at its apex (diameter $\sim$ 100 nm) acting as the probe, mounted at the end of a cantilever [22]. The optical signal transmitted through the nanoaperture was collected by a microscope objective and focused on a photomultiplier tube detector (PMT). The sample stage was translated using piezoelectric translators, while the tip and the illuminator were maintained at a fixed position. The studied objects being much smaller than the illuminated region (3 μm and 60 μm, respectively), we assume that similar illumination conditions were maintained throughout the experiment in spite of the sample translation.

Regarding the DHH measurements, direct illumination in transmission mode, even through a thin film of gold, can blind the detector and cause strong interference with the measured fields which are weak for a single nanoobject. This is the reason why we chose an excitation beam at an incidence angle of 45° for the holographic measurement. In this TIR configuration, the s-polarization remains in the plane of the sample, whereas p-polarization has a component across its surface. We therefore chose to excite the chain with an s-polarized incident wave (see schemes on Fig. 1.12(a) and 1.13(a)) and to rotate the sample in order to analyse both longitudinal and transverse polarizations with respect to the chain axis. Regarding the NSOM measurements, the metallized lateral facets of the pyramid nanoaperture act as a screen, efficiently removing stray light, and therefore allowing excitation under normal incidence. The difference in excitation conditions between the two techniques (oblique and normal incidence) only play a role in the case of a transverse polarization, as detailed below in the non-resonant case.

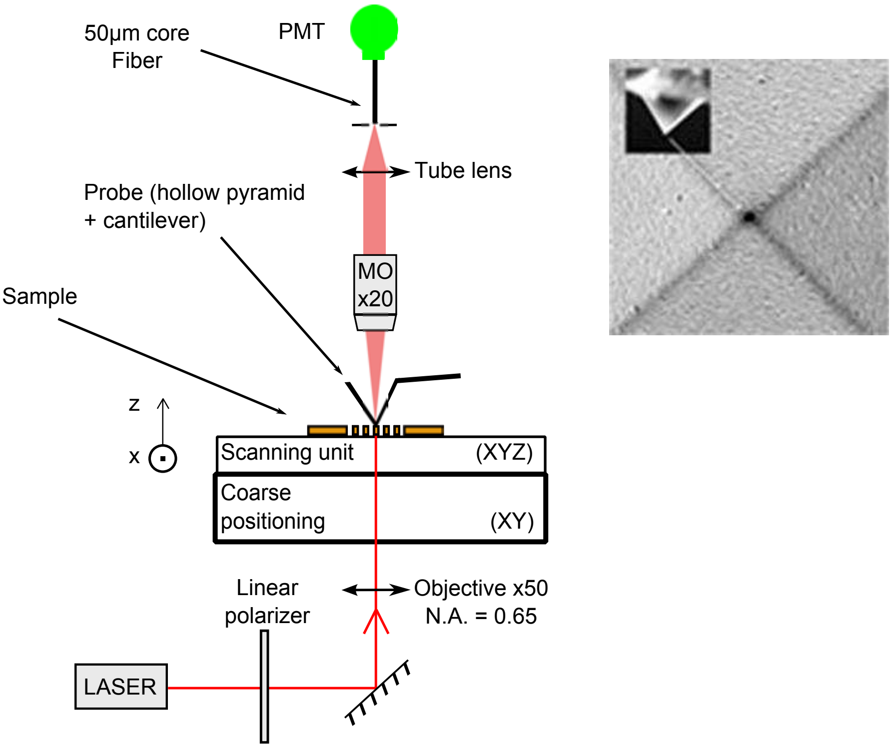

FIGURE 1.11: NSOM setup using a hollow silicon square-based pyramid with a nanoaperture at its apex (diameter $\sim$ 100 nm) acting as the probe, mounted at the end of a cantilever.

Comparison between DHH and NSOM images

Resonant case

Let us first look at the resonant case, i.e. under a polarization along the chain axis, shown in Fig. 1.12. On the one hand, we acquired in-plane xy images with both techniques. While with DHH we only needed to reconstruct the xy-plane containing the nanohole antenna by propagating the demodulated hologram to the corresponding z distance, with the NSOM device the tip had to be laterally scanned along the whole surface, with the apex of the hollow pyramid permanently in contact with the surface. This way, near-field in-plane images as well as topographic images were collected simultaneously. The images obtained using each of these techniques were very similar (see Fig. 1.12(b)), despite the fact that the holographic image was obviously less resolved, the NSOM lateral resolution being determined by the tip aperture, around 100 nm. Both showed an homogeneous intensity distribution, suggesting coupling between neighbouring nanoholes.

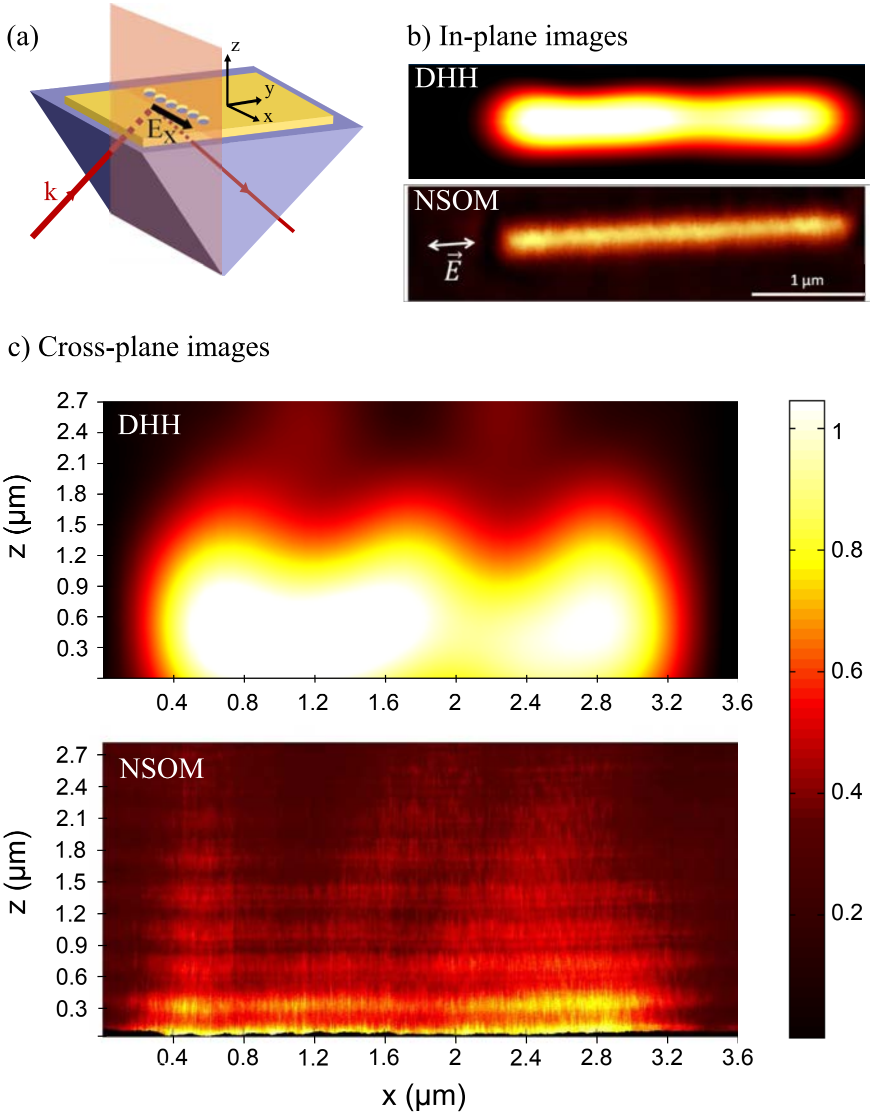

FIGURE 1.12: Resonant case. (a) Experimental configuration for the holographic far-field measurement of a 40 nm thick gold film (17 holes, 150 nm in diameter, separated by 20 nm) for an electric field polarization parallel to the axis of the antenna. (b) In-plane holographic reconstruction of the intensity in the plane of a nanohole chain antenna, under TIR illumination, and the corresponding near-field images obtained for an incident wave vector perpendicular to the plane of the gold layer. (c) Intensity in a plane perpendicular to the gold layer.

On the other hand, regarding the cross-plane images (xz), after the DHH measurement the reconstruction of one single hologram was performed in several z planes by steps of 100 nm, although the axial resolution of this diffraction-limited technique is of the order of 1.5 μm at the present wavelength. The corresponding NSOM acquisition (Fig. 1.12(c)) was performed by retracting the tip and recording the measured intensity as a function of the tip-to-surface distance (z coordinate, 10 nm steps) at several lateral positions (x coordinate, 10 nm steps) along the nanoantenna. The NSOM resolution in the axial direction is expected to be at best of the order of the skin depth of the pyramid metal (a few 10 nm). Both axial cross-sections obtained with each of the two techniques qualitatively agree and we distinguish three main radiation lobes with a marked directivity.

Such NSOM microscopes are mostly designed to deliver xy-plane images. However, Costantini *et al.* [22] recently showed that series of intensity profiles performed by retracting the tip at different locations can provide optical images in a plane perpendicular to the sample surface in order to record cross-sections (xz) of the scattered field. Other approaches in which several xy-planes are recorded at different heights have also been proposed [21]. However, taking series of vertical lines, as proposed here, has the important advantage of allowing contact, and therefore a correct value of z, at the beginning of each vertical line acquisition. Note that the vertical intensity modulation in the NSOM image is a perturbation due to interference between light directly transmitted through the nanoholes and through the thin film and light scattered by the pyramid apex and back-reflected on the metallic surface of the sample into the aperture, as had already been observed in [22, 53].

Non-resonant case

For an excitation light polarized orthogonally to the chain axis, the in-plane NSOM image (Fig. 1.13(b)) shows an intensity distribution in which bright spots appear on the two rims of the chain. Such a spatial field distribution suggests a dipolar charge oscillation in the hole walls along the incident polarization direction. Indeed, electrodynamic simulations demonstrated the analogy between LSP resonances induced in isolated gold nanodisks and the very similar charge distribution in disk-like nanoholes of complementary dimensions [73].

However, the near-field and the far-field images for the non-resonant case significantly differ. In the far-field, we do not see the dipolar distribution at every nanohole location but only two bright spots at the edges of the chain. We attribute this asymmetry between the near- and far-field images to the oblique incidence in the DHH measurement. Indeed, under TIR illumination and for transverse polarization, all the nanoholes in the chain are not excited in phase (as opposed to a polarization parallel to the chain axis, for which all elements are excited in phase despite the oblique angle of incidence). The length between the center of the first and the last nanohole of the chain is equal to $L = 150$ nm $\times$ 16 holes $+ 20$ nm $\times$ 16 gaps $= 2720$ nm. For an incidence angle of 45°, the path difference between them is very approximately three times the wavelength of the exciting wave, i.e. $\delta = L\sin(45°) \simeq 3\lambda$. Thus, the central nanohole sees an incident field phase shifted by $\phi = k\delta/2 = 3\pi$ rad.

Phase-imaging

We took advantage of our interferometric technique to look at the holographic phase

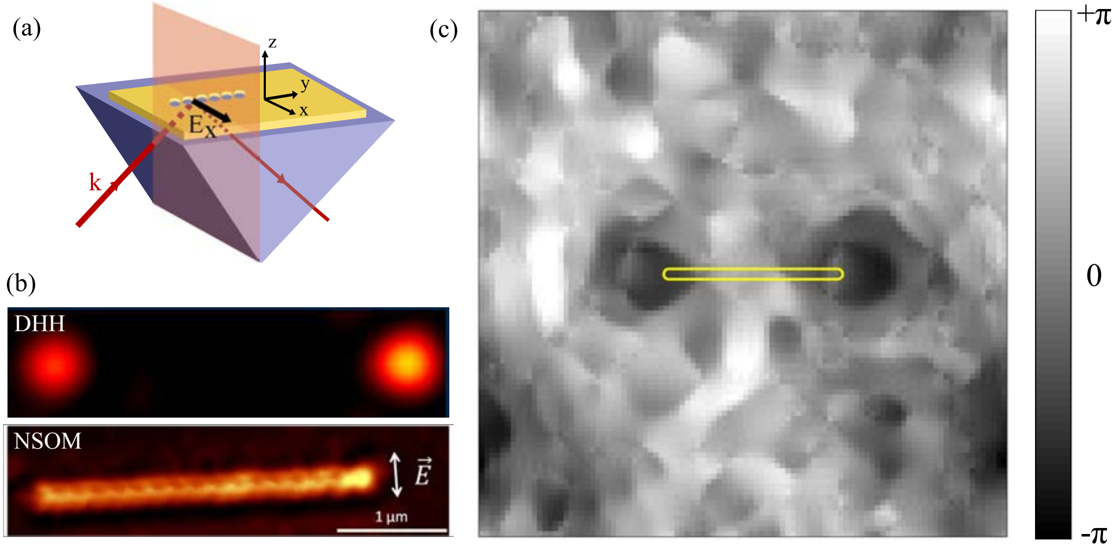

FIGURE 1.13: Non-resonant case.(a) Experimental configuration for the holographic far-field measurement of a 40 nm thick gold film (17 holes, 150 nm in diameter, separated by 20 nm) for an electric field polarization perpendicular to the axis of the antenna. (b) In-plane holographic reconstruction of the intensity in the plane of a nanohole chain antenna, under TIR illumination, and the corresponding near-field images obtained for an incident wave vector perpendicular to the plane of the gold layer. (c) Unwrapped holographic phase image in the plane of the antenna.

image reconstructed at the plane of the antenna (see Fig. 1.13(c)). However, the periodicity of the phase causes problems in the recovery known as *wrapping* effects. If the phase difference is larger than 2π, then the measured phase will be wrapped modulo 2π and the computed value will be $\phi_w = \phi - 2\pi n$, where n is an integer number. There exist several unwrapping algorithms allowing the recovery of the true phase [19, 97], so that the real physical quantities can be extracted from a given phase map. One of these methods, developed by Dr. Marc Guillon, from the research centre of *Neurophysiologie et Nouvelles Microscopies* (in Paris), allowed the phase unwrapping of this particular image using the Helmholtz Hodge decomposition approach [12]. As expected considering the length of the antenna and the angle of incidence, we measure a relative π-shift between the central nanohole and the two nanoholes at the chain edges. The gray scale indicating the relative phase, the two edges of the chain appear dark while the central position is bright. Thus, under this out-of-phase excitation, only two bright spots appear in the scattered far-field intensity image, owing to the coherent far-field superposition of the light scattered by the different individual dipoles.

Conclusions

In this chapter, we have introduced the working principles of digital heterodyne holographic microscopy. After presenting our specific experimental implementation, we have described the hologram reconstruction algorithm used throughout this thesis work, together with some practical considerations regarding the computational steps. Finally, in the context of our group's previous research, we have shown that optical intensity distributions near the plane of a diffracting nanoantenna can be accurately reconstructed by DHH microscopy. For an in-phase illumination of all the elements in the nanoantenna, good qualitative agreement has been demonstrated by comparing our holographic measurements to near-field images performed using the well-established technique of aperture near-field scanning optical microscopy, both in the plane of the nanoantenna and across. Consequently, although being diffraction-limited, we believe that DHH microscopy is a promising tool for the fast, easy and non-invasive characterization of plasmonic nanoantennas in many cases. Particularly, we have seen that cross-plane images are cumbersome to achieve with scanning techniques, whereas DHH allows for a whole volume reconstruction from a single acquisition. In addition, DHH simultaneously gives access to the phase of the nanoantenna, helping to gain more insight about its scattering pattern.

“*Lycurgus cup*”, 4th-century. First example of the use of gold nanoparticles in the staining of glass.
British Museum

Chapter 2

Metallic nanoparticles

Small objects from 10 nm and up to 100 nm in size are widely referred as nanoparticles. At this scale, size-related properties that differ from bulk materials may arise. Particularly, we focus our interest on metallic nanoparticles (MNPs) in solution. They are most commonly chemically synthesized through the reduction of a metal salt in the presence of a stabilizer, which limits the growth of the particles, directs their shape and provides colloidal stability.

Throughout this thesis work, nanoparticles are used as optical probes, which requires a good knowledge of their optical properties. In this chapter, we first report the basic principles accounting for the electromagnetic response of a nanoparticle under an incident light wave. Absorption and scattering are the two main phenomena discussed here. Using the holographic tools presented in the previous chapter and this description of the optical properties of MNPs, we present a first set of results regarding the optical investigation of chemical transformations of individual MNPs. We particularly focus on oxidation reactions initiated by electrochemistry, by simultaneously investigating the system via holography and electrochemistry techniques.

2.1 Overview of the electromagnetic response of nanoparticles

When light waves encounter an object of any size, their energy propagation changes. Matter being composed by discrete electrical charges, these charges oscillate upon illumination by the incident electromagnetic field and radiate in turn electromagnetic energy, what is called *scattered light*. Besides this elastic re-emission of light, matter can

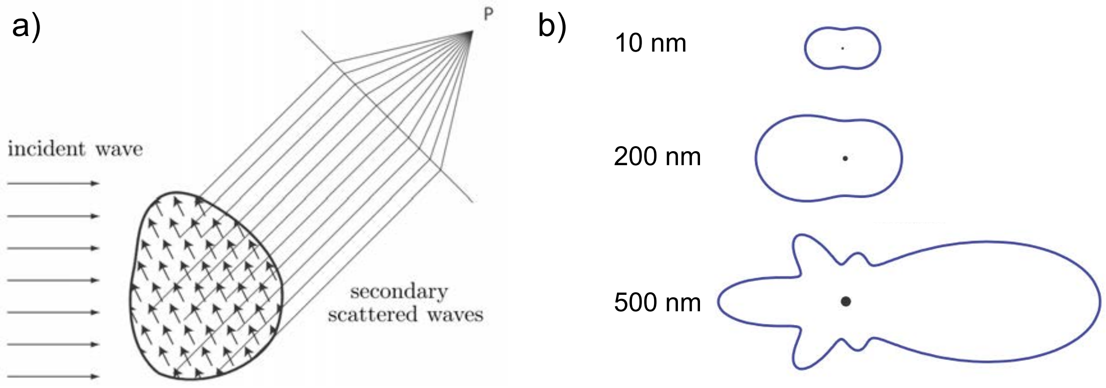

Figure 2.1: a) Superposition of the wavelets scattered by elementary dipoles inside the object at an observation point P. b) Scattering diagrams for spherical particles of different size under white light illumination. Amplitudes are not proportional between diagrams.

also absorb part of the incident energy and convert it into other forms such as heat or vibrations.

Before we go into any mathematical formalism, it is useful to discuss which parameters determine the amplitude and phase relations between the multiple individual dipoles induced in an object by an incident light wave. One can easily imagine that the number of possible phase relations between elementary dipoles increases for bigger particles and that the shape of the object also plays a major role (see Fig. 2.1). Strictly speaking, it is the size and shape of the particle versus the wavelength and the polarization of the incident light that determines the particle's response. But phase relations will also be governed by the object composition, which determines the medium permittivity, i.e., the resistance of the medium to be polarized. To summarize, the factors that determine the scattering and absorption efficiencies of the object under study are:

- the object characteristic size, a, and shape
- $\varepsilon_1(\omega)$ and $\varepsilon_2(\omega)$ the dielectric functions of the object and the surrounding medium, respectively
- the wavelength of the incident light, λ, the polarization and the wavevector

However, calculating the analytical expression of the field scattered by an object can be very cumbersome, as it requires solving Maxwell's equations for the particular object shape and composition. In 1908, Gustav Mie analytically solved the scattering problem for spherical particles of any size [59], by decomposing the incident field in its multipolar infinite series under spherical coordinates. Nowadays, the term "Mie scattering" is commonly used to describe cases in which the size of the particle is comparable to the wavelength of the incident light, i.e. for $a \sim \lambda$. A later version of this theory, called "generalized Mie theory" is also able to account for non-spherical particle shapes.

For the scattering of particles much smaller than the incident light, Lord Rayleigh developed in 1871 a simpler formalism [72]. In Rayleigh's regime, when $a \ll \lambda$, the phase of the incident electromagnetic wave is practically constant over the particle volume. Consequently, all points of the object respond simultaneously and the particle can be considered as an individual radiating dipole. Accordingly, this regime is also commonly called the *dipolar regime*.

One can adopt an even simpler analysis by considering the dipolar regime in the electrostatic limit. For very small particles, owing to the absence of retardation effects, total spatial field distribution can be calculated by assuming the simplified problem of an electric dipole in an electrostatic field. The harmonic time dependence can then be added to the solution once the field distributions are known. This approach is therefore called the *quasi-static approximation*.

As the particle size used in this thesis work ranges from 60 nm to 100 nm, this size can no longer be considered negligible compared to our excitation wavelengths in the visible domain. Hence, we should use Mie's rigorous formalism to solve the full scattering problem. Still, the quasi-static approximation describes quite adequately the optical properties of nanoparticles up to 100 nm for many purposes [55]. Although not fully accurate, the quasi-static approximation is also particularly useful to give a qualitative idea about the scattering and absorption behaviour of nanoparticles.

2.1.1 Quasi-static approximation

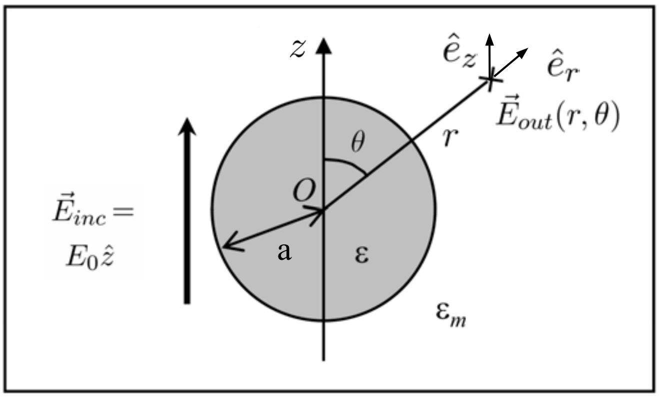

FIGURE 2.2: Spherical particle of radius a located at the origin in a uniform, static electric field.

In the electrostatic problem, the Helmholtz equation reduces to the Laplace equation, which is much easier to solve. We are thus interested in the solution of the Laplace equation for the potential, $\Delta\Phi = 0$, from which the electric field can be calculated: $\vec{E}_{inc} = -\nabla\Phi$. As an example, let us consider the analytical solution for the easiest geometry: an homogeneous sphere of radius a located at the origin in a uniform, static electric field $\vec{E} = E_0\hat{z}$ (see Fig. 2.2). The surrounding medium is assumed to be isotropic and non-absorbing with dielectric constant ε_m, and the field lines are parallel to the z-direction. The dielectric response of the sphere is described by the dielectric permittivity ε which is, in general, a complex number. Under these conditions, the solution for the field distribution outside the nanosphere is the following [55]:

$$\vec{E}_{out}(r,\theta) = E_0\hat{e}_z + E_0 a^3 \frac{\varepsilon - \varepsilon_m}{\varepsilon + 2\varepsilon_m} \frac{3\cos\theta\hat{e}_r - \hat{e}_z}{r^3} \tag{2.1}$$

The total external field is thus the superposition of the applied field plus a second term which takes the same form as the electric field created by a dipole located at the sphere center and oriented along the direction of the incident electric field:

$$\vec{E}_{dipole}(\vec{r}) = \frac{1}{4\pi\varepsilon_0\varepsilon_m} \frac{3(\vec{p}\cdot\hat{e}_r)\hat{e}_r - \vec{p}}{r^3} \tag{2.2}$$

By matching equations (2.1) and (2.2), we can express the dipolar moment induced inside the sphere, which is proportional to $|E_0|$ in magnitude:

$$\vec{p} = 4\pi\varepsilon_0\varepsilon_m a^3 \frac{\varepsilon - \varepsilon_m}{\varepsilon + 2\varepsilon_m}\vec{E}_0 \tag{2.3}$$

Here, we can introduce the polarizability α_0, defined via $\vec{p} = \varepsilon_0\varepsilon_m\alpha_0\vec{E}_0$

$$\alpha_0 = 4\pi a^3 \frac{\varepsilon - \varepsilon_m}{\varepsilon + 2\varepsilon_m} \tag{2.4}$$

Thus we see that the polarizability, for a given particle shape, embraces three of the key parameters playing a role in the electromagnetic response of the particle: the particle size and both the composition of the particle and that of the surrounding medium. We discuss the limits of this electrostatic polarizability in the following section.

2.1.2 Oscillating electric dipole fields

In the dynamic case, e.g. under plane-wave illumination with $\vec{E}(\vec{r},t) = E_0 e^{-i\omega t}$, the incident field induces an oscillating dipole moment $\vec{p} = \varepsilon_0\varepsilon_m\alpha(\omega)\vec{E}_0 e^{-i\omega t}$. Here, the frequency dependence of the permittivity ($\varepsilon(\omega)$) has to be taken into account. The radiation of this dipole leads to the scattering of the incident plane wave by the sphere. Many reference books, which describe the extinction efficiency (energy removal from the incident beam due to the presence of the particle) by small spherical particles, consider the dipolar approximation in the electrostatic limit. However, the electrostatic polarizability α_0 given by Eq. 2.4 violates the principle of energy conservation.

Let us briefly review the basics of the electromagnetic fields associated with an oscillating electric dipole. The total fields $\vec{H}(t) = \vec{H}e^{-i\omega t}$ and $\vec{E}(t) = \vec{E}e^{-i\omega t}$ in any point in space are (see Ref.[41] for demonstration):

$$\vec{E} = \frac{1}{4\pi\varepsilon_0\varepsilon_m}\left\{k^2(\vec{n}\times\vec{p})\times\vec{n}\frac{e^{ikr}}{r} + [3\vec{n}(\vec{n}\cdot\vec{p}) - \vec{p}]\left(\frac{1}{r^3} - \frac{ik}{r^2}\right)e^{ikr}\right\} \tag{2.5}$$

$$\vec{H} = \frac{ck^2}{4\pi}(\vec{n}\times\vec{p})\frac{e^{ikr}}{r}\left(1 - \frac{1}{ikr}\right) \tag{2.6}$$

with $k = 2\pi/\lambda$ and $\vec{n}$ the unit vector in the direction of the observation point r. There are two main spatial regions of interest, depending on the distance to the dipole. Very close to the dipole, $kr \ll 1$, is what is called the near-field region. Far from it, $kr \gg 1$, the region is known as the radiative far-field zone.

In the far-field zone, the dipole fields are of the well-known spherical-wave form:

$$\vec{E} = \sqrt{\frac{\mu_0}{\varepsilon_0\varepsilon_m}}\vec{H}\times\vec{n} \tag{2.7}$$

$$\vec{H} = \frac{ck^2}{4\pi}(\vec{n}\times\vec{p})\frac{e^{ikr}}{r} \tag{2.8}$$

whereas in the near-field zone limit, the fields approach:

$$\vec{E} = \frac{3\vec{n}(\vec{n}\cdot\vec{p}) - \vec{p}}{4\pi\varepsilon_0\varepsilon_m}\frac{1}{r^3} \tag{2.9}$$

$$\vec{H} = \frac{i\omega}{4\pi}(\vec{n}\times\vec{p})\frac{1}{r^2} \tag{2.10}$$

We can see that within the near-field, the fields are predominantly electric in nature, since the magnitude of the magnetic field is about a factor $\sqrt{\varepsilon_0\varepsilon_m}(kr)$ smaller than that of the electric field. For static fields ($kr \to 0$), the magnetic field simply vanishes. Moreover, with Eq.2.9 we recover the expression obtained for the quasi-static approximation. This means that in the derivation of the electrostatic polarizability no radiative components of the oscillating dipole were taken into account. Consequently, α_0 cannot take into account the particle's scattering and therefore radiative corrections to the electrostatic polarizability need to be included in order to solve the problem of energy conservation [5]. Still, the simple expression of α_0 is often used to roughly estimate the order of magnitude of an absorbing particle's polarizability in many cases.

2.1.3 Scattering and absorption cross-sections

Scattering and absorption cross-sections have area units; they determine quantitatively the object effective area that interacts with the incident field. They are described as follows:

$$\begin{aligned} C_{scat} &= \frac{P_{scat}}{I_{inc}} \\ C_{abs} &= \frac{P_{abs}}{I_{inc}} \end{aligned} \tag{2.11}$$

where P_{scat} and P_{abs} are the power scattered/absorbed by the particle, respectively, and I_{inc} is the incident power per unit surface (irradiance), defined as the time averaged modulus of the Poynting vector:

$$I_{inc} = \left|\left\langle \vec{S}_{inc}(\vec{r}) \right\rangle\right| = \left| \frac{1}{2} \Re\{\vec{E}_{inc}(\vec{r}, t) \wedge \vec{H}^{*}_{inc}(\vec{r}, t)\} \right| \tag{2.12}$$

For a spherical particle in the dipolar regime and under the quasi-static approximation, C_{scat} and C_{abs} can be calculated via the Poynting vector determined from Ref. [16] as:

$$\begin{aligned} C_{scat} &= \frac{k^4}{6\pi}|\alpha_0|^2 = \frac{8\pi}{3}k^4 a^6 \left| \frac{\varepsilon - \varepsilon_m}{\varepsilon + 2\varepsilon_m} \right|^2 \\ C_{abs} &= k \ \mathrm{Im}[\alpha_0] = 4\pi k a^3 \ \mathrm{Im}\left[\frac{\varepsilon - \varepsilon_m}{\varepsilon + 2\varepsilon_m} \right] \end{aligned} \tag{2.13}$$

We point out that no explicit assumptions were made in our derivations so far about the sphere material. The expressions for the cross-sections in Eq. 2.13 are thus valid for dielectric as well as for metallic scatterers (the only difference lies in the the real or complex value of ε), and demonstrate a very important problem for practical purposes. Due to the rapid scaling of $C_{scat} \propto a^6$, very little light is scattered by small particles, hindering their optical detection. Particularly, imaging small nanoparticles immersed in a background of larger scatterers can in many cases only be achieved using photothermal techniques relying on the slower scaling of the absorption cross section with size [4]. In the next section, we discuss the advantages of using metallic nanoparticles.

2.1.4 Localized surface plasmon resonances

The optical properties of metals can be described by their complex dielectric function, which depends on the frequency of light, $\varepsilon(\omega) = \varepsilon_1(\omega) + i\varepsilon_2(\omega)$. Without going into much detail, these properties are mainly determined by two phenomena. On the one hand, conduction electrons can move freely inside the metal, as opposed to bound electrons in dielectric media. The Drude-Sommerfeld theory describes reasonably well the contribution of this conduction electrons, called the *free-electron gas*, by solving the equation of motion for free electrons under the influence of an external harmonic field. On the other hand, high-energy incident photons at optical frequencies can promote electrons from lower-lying bands to the conduction band, inducing interband transitions, therefore modifying the behaviour of the material as compared to an ideal Drude metal.

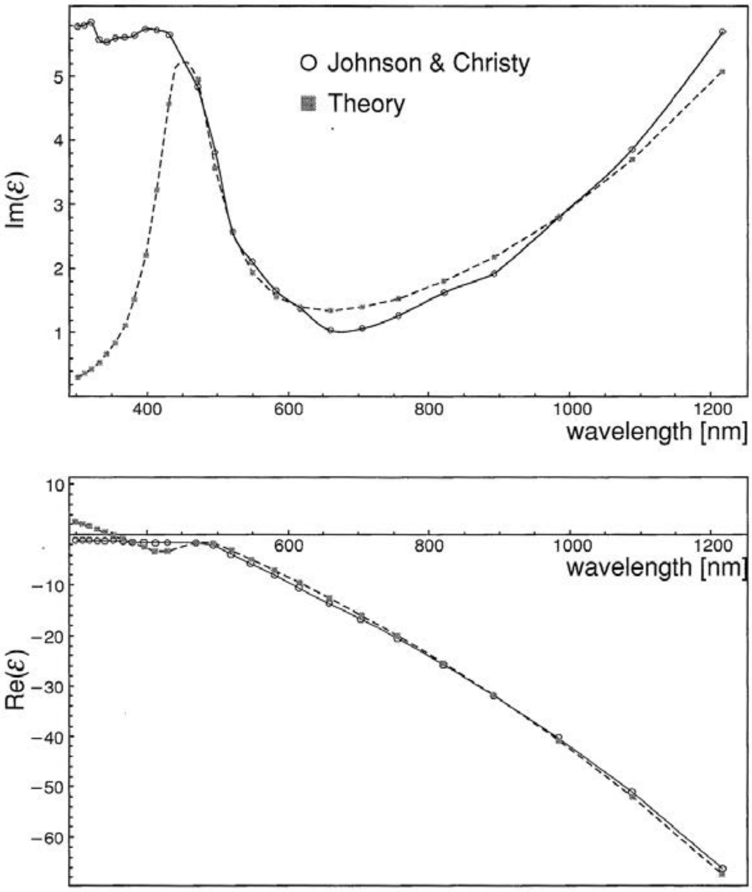

FIGURE 2.3: Real and imaginary parts of the dielectric function of gold. Circles: Experimental values from [42]. Squares: Model of the dielectric function taking into account the free-electron contribution and the contribution of a single interband transition. A better reproduction of the experimental values at high energies can be obtained by integrating more interband transitions.

Both contributions, from free and bound electrons, lead to a negative value of the real part of the dielectric constant [65]. Consequently, for metals, and particularly for the case of a sphere derived in Eq. 2.4, the polarizability experiences a resonant enhancement under the condition that $|\varepsilon(\omega)+2\varepsilon_m|$ is minimum, which for the case of a non-absorbing medium (at least around the resonance frequency) simplifies to

$$Re[\varepsilon(\omega)] = -2\varepsilon_m \tag{2.14}$$

This relationship is know as the Fröhlich condition. For gold and silver, this resonance falls into the visible region of the spectrum. The collective oscillating response of the electrons in resonance with the incident light is known as the plasmon resonance, plasmons being by definition the quanta of surface-charge-density oscillations coupled to electromagnetic waves. The associated resonant frequency, derived in the present case from the quasi-static approximation, is called the *dipolar surface plasmon* resonant frequency of the metal nanoparticle.

On the one hand, for a planar metal surface, the excitation of this resonance is known as a Surface Plasmon Resonance (SPR): the coupling of an incident electromagnetic field with oscillations of the conductor's free-electron gas leads to p-polarized surface waves propagating along the interface between the conductor and the surrounding electromagnetic medium. In the direction perpendicular to the interface, these surface plasmons waves are evanescently confined. On the other hand, an incident EM field on a metallic nanoparticle induces as well a coherent oscillation of the free-electron cloud (see Fig. 2.4). Due to the particle finite size, the displacement of the electron cloud inside the nanoparticle induces a depolarizing force, governed by Coulomb's law. A resonant coupling with the incident electromagnetic field arises for an incident frequency appropriately tuned with the characteristic frequency of the charge oscillation inside the nanoparticle. This resonance is then called a Localised Surface Plasmon Resonance (LSPR). When one of these LSPRs arises, it leads to a field enhancement both inside and in the near-field zone outside the particle [75]. This field is highly localized at the nanoparticle and decays rapidly with distance (since $\mathbf{E}_{out} \propto 1/r^3$), as far-field scattering and absorption by the particle are greatly enhanced by the resonance. Equations 2.13 show that, indeed, for metal nanoparticles both absorption and scattering are resonantly enhanced at the dipole particle plasmon resonance, as both cross-sections depend on the polarizability.

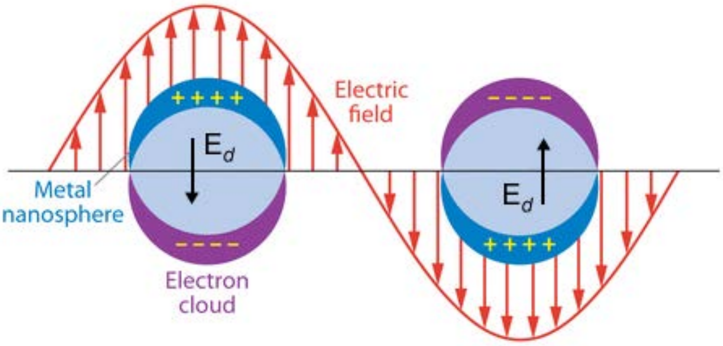

FIGURE 2.4: Sketch of a homogeneous metal sphere placed into a harmonically oscillating electromagnetic field, at two different moments of the field passage.

Gold nanoparticles spectra

Experimentally, optical spectroscopy based on scattering or extinction (absorption together with scattering) measurements is the simplest method to detect LSPR. Alternatively, we used an on-line open-source Mie calculator [1] to plot the accurate spectra of the gold nanoparticles used in this thesis work (see Fig. 2.5). Our first experiences were performed using a diode laser at 660 nm (Opnext HL6545MG, max. power 120 mW) to image 100 nm particles. Despite not being at the plasmon resonance of the beads, their scattering cross-section was beyond our sensitivity threshold, so we were able to detect them. Conversely, when we tried to image smaller particles, reducing the size to 60 nm diameter particles, we were obliged to adapt our wavelength. For this size we chose to excite the NPs close to their scattering resonant wavelength with a single-mode solid-state laser at 532 nm (CNILASER, max. power 80 mW).

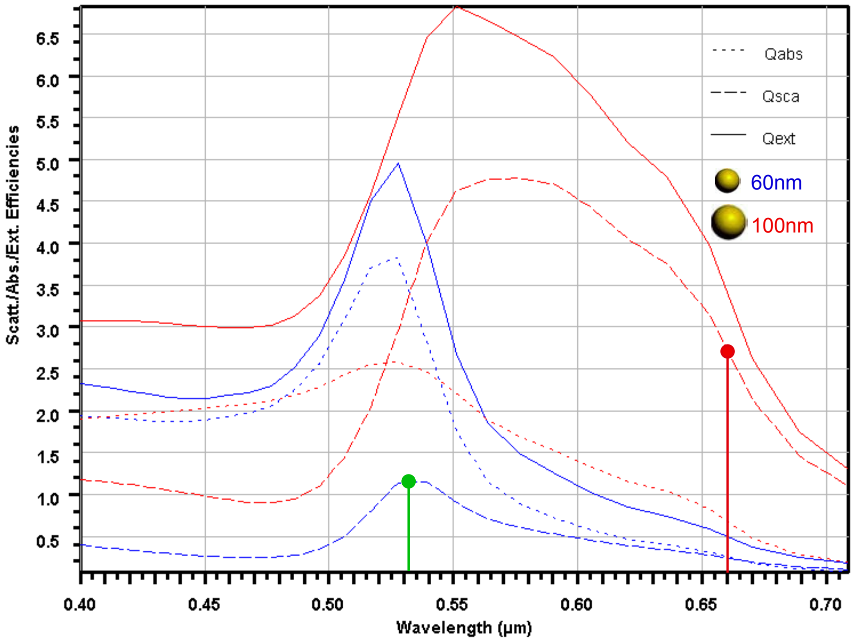

FIGURE 2.5: Spectra from http://www.lightscattering.de/MieCalc/eindex.html, calculated for the two main sizes of NPs used throughout this PhD work. The green and red dots indicate our two excitation wavelengths at 532 nm and 660 nm, respectively.

If we denote $A = \pi a^2$ the geometrical area of the particle, an even more intuitive dimensionless parameter is the **scattering efficiency coefficient**:

$$Q_{scat} = \frac{C_{scat}}{A} \tag{2.15}$$

Finally, Fig. 2.6 shows the scattering dependence on the incident polarization direction.

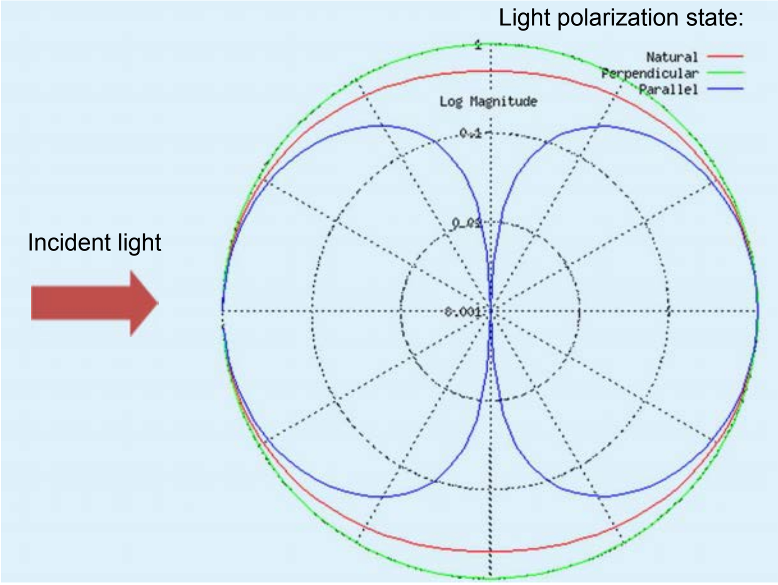

FIGURE 2.6: Simple polar graph of the scattering pattern, from http://omlc.org/calc/mie_calc.html (radial distance is plotted on a log scale). Light is incident from the left on a sphere located at the center of the polar plot.

2.2 Electrochemistry studies coupled to holographic imaging

Electrochemistry, as its name suggests, is the study of chemical reactions between an electrode (a solid metal or a semiconductor) and an electrolyte (usually ionic species in a liquid solution). In other words, it deals with the interaction between electrical energy and chemical change: it studies both chemical reactions caused by an externally supplied current, and electrical currents produced by a spontaneous chemical reaction (as in a battery). Recently, nanoparticle detection capabilities using electrochemistry have been reported, involving the observation of Faradaic charge transfer associated with the quantitative destructive oxidation of nanoparticles colliding with (or becoming adsorbed to) an electrode surface [81].

However, nanoparticle suspensions exhibit properties that can vary dramatically depending upon the synthesis methodology. Even for a highly characterised nearly monodisperse nanoparticle system, the particle size distribution can be significant. Therefore, single particle electrochemical studies are a particularly crucial area. Unfortunately, a number of key issues remain, specially concerning the particles behaviour within solution (when not in contact with the electrode), such as possible agglomeration or aggregation of particles.

The work presented in this section was done in collaboration by an electrochemistry group from the *ESPCI Paristech* in Paris and a research group from the *Department of*

Chemistry, Physical and Theoretical Chemistry Laboratory from the University of Oxford. The aim of the collaboration was to study the chemical reactions of colloidal silver NPs adsorbed onto a thin-film gold electrode by simultaneously investigating the system via digital holography and electrochemistry. While electrochemistry can easily provide ensemble measurements, holography allows to individually visualize many single particle stochastic events. Moreover, holography being a non-invasive 3D imaging technique capable of imaging inside a water-based system, the particles can be investigated *in situ* in a typical electrochemical situation. The change in the optical response of the silver nanoparticles during their chemical reaction may as well help us elucidate the particles' transformation. Hereafter, we show how the coupling of both techniques can offer more chemical and physical insight. This work led to a joint publication [13].

Electrochemical setup

A standard three-electrode setup was used, comprising a thin (40 nm) evaporated gold film working electrode supported on a glass slide, a coiled platinum wire acting as the counter, and a AgCl modified silver wire as a reference. The working electrode potential was controlled and the electrode current was measured using a CH660B potentiostat (CH Instruments, IJ Cambria), with the electrochemical experiments being performed at room temperature ($25 \pm 2°$C). Citrate capped silver nanoparticles were synthesised, with an average radius of 23 ± 9 nm. The experiments were performed in 0.1 M NaCl, with 200 μL of the silver nanoparticles solution being diluted to a total volume of 1 mL of ultrapure water (resistivity not less than 18.2 $\mathrm{M}\Omega \cdot \mathrm{cm}$ at 25°C). In order to enclose and protect the nanoparticles, we fabricated microfluidic chambers using a glass slide/parafilm®/cover-slip stack: a double-layer ring of parafilm was heated to its melting point to serve as waterproof spacer of ~ 150 μm thickness, and to seal tightly two plastic micropipettes which were used to fill the chamber after fabrication. A schematic of the fabricated thin-layer electrochemical cell is shown in Fig. 2.7.

Results

Electrochemistry of individual Ag NPs

Inside the electrolytic solution and for a given applied voltage, the silver NPs that are in contact with the gold electrode can be oxidized. This oxidation implies the donation of an electron by the NP to the gold surface, according to the following electrochemical equation:

$$\mathrm{Ag}_{\ (\mathrm{NP})} \rightarrow \mathrm{Ag}^{+}_{(\mathrm{sol})} + \mathrm{e}^{-}_{(\mathrm{electrode})} \tag{2.16}$$

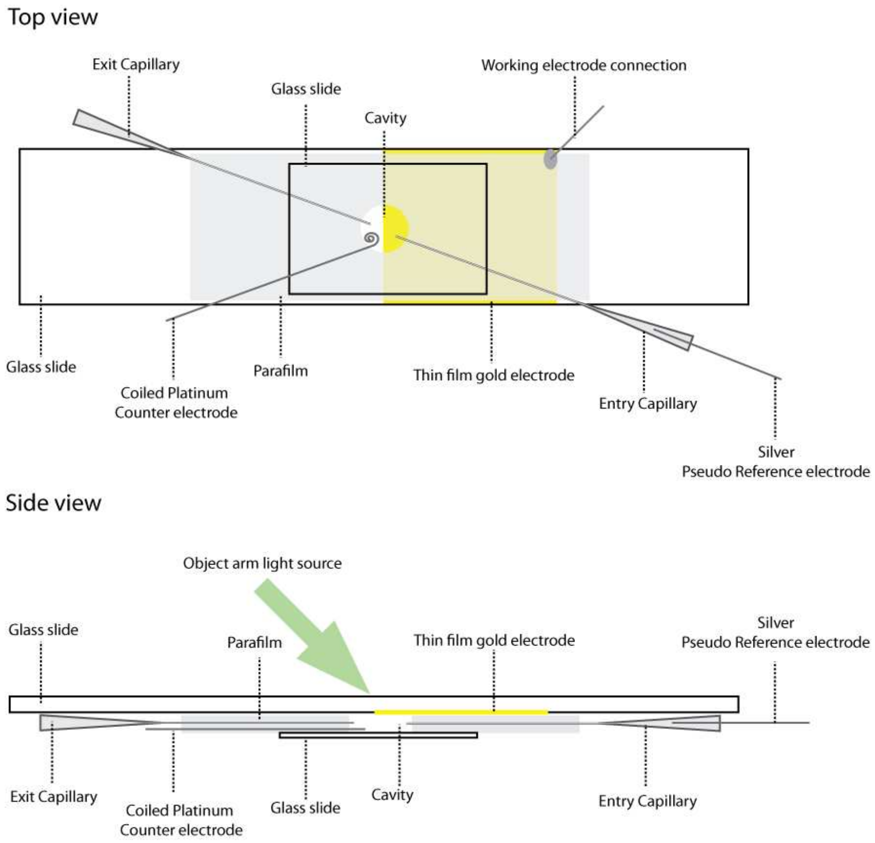

FIGURE 2.7: Schematic description of the microfluidic chamber/cell. The green arrow shows the direction of the laser propagation and, as can be seen in the side view, the working gold electrode is situated on the upper plane.

Basically, upon oxidation, one expects to transform the Ag NP into Ag^+, which may be dissolved into the solution while an electron is injected into the electrode per Ag transformed atom. Consequently, this oxidation induces a measurable current [81].

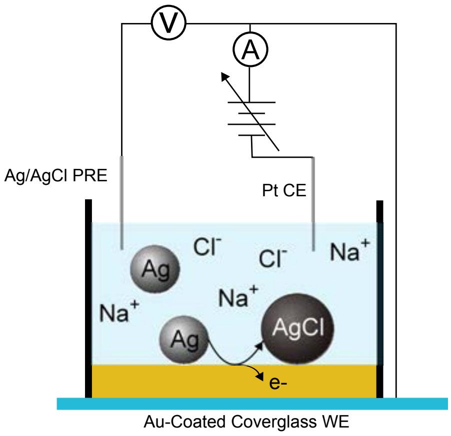

FIGURE 2.8: Schematic diagram illustrating a silver nanoparticle with a potentiostatted electrode. The silver nanoparticle is oxidised upon contact to the electrode, leading to the formation of a silver chlorite particle.

In our case, due to the presence of chloride in the solution (NaCl, sodium chloride solution), the transfer of an electron to the electrode during the oxidation process is expected to transform the Ag NPs into AgCl NPs (silver chloride NPs, as schematically depicted in Fig. 2.8) according to:

$$\text{Ag}_{\text{ (NP)}} + \text{Cl}^-_{\text{(sol)}} \rightarrow \text{AgCl}_{\text{ (NP)}} + \text{e}^-_{\text{(electrode)}} \tag{2.17}$$

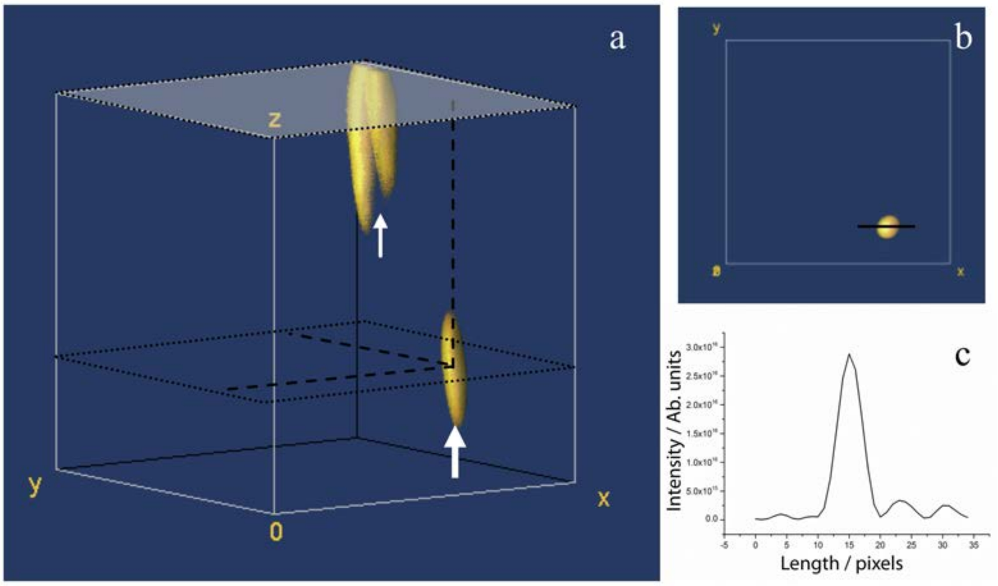

FIGURE 2.9: (a) 3D volume representations of scattered intensity isosurfaces, along with (b) XY plane section and (c) scattering intensity, showing the object to be diffraction-limited in size. In (a) the upper white plane corresponds to the electrode plane.

Holographic tracking and NP's size estimation

Before performing any electrochemistry measurements, we acquired holographic films of the silver NPs freely moving inside the cell at an acquisition rate of 12 Hz. Using holography, we were able to detect and track the NPs in solution as well as the features (either NPs or defects) immobilized at the electrode surface. For instance, Fig. 2.9 shows the reconstruction of one of the recorded holographic frames, which features two fixed bright spots corresponding to two scattering defects at the electrode plane and one colloidal NP in the solution. With this 3D temporal information we were able to track this NP until it was adsorbed at the electrode surface (see Fig. 2.10). The tracking allowed us to estimate quite accurately the NP size by fitting its Mean Square Displacement (see Chap. 3 for tracking details). In particular, this allowed us to demonstrate that all detected NPs were aggregates (radius $>$ 50nm) instead of individual 23 nm radii NPs. This is mainly due to the use of high concentrations of electrolyte, which decreases the Debye length and favours inter-NP interactions and aggregation [28, 79].

Next, we launched simultaneously the optical and electrochemical measurements.

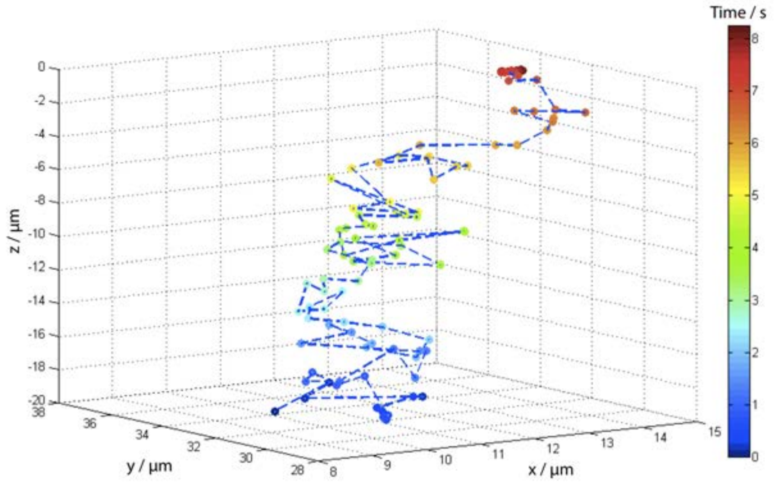

FIGURE 2.10: An example of 3D nanoparticle tracking over 8 s, depicting the particle adsorption onto the electrode surface situated on the upper plane of the volume.

Electrochemical observations

Figure 2.11 shows the voltammogram obtained by sweeping the potential applied to the gold electrode in a cyclic manner. In the forward sweep, one can see that an oxidation peak appears, corresponding to the oxidation of silver NPs previously adsorbed on the gold electrode. At larger voltage values, a second broad feature can be found due to the onset of the oxidation of the gold surface itself. In the backward sweep, there is also a reduction peak associated with the silver NPs' reaction, which indicates that their oxidation process is reversible:

$$\mathrm{AgCl}_{\ (\mathrm{NP})} + \mathrm{e}^{-}_{(\mathrm{electrode})} \rightarrow \mathrm{Ag}_{\ (\mathrm{NP})} + \mathrm{Cl}^{-}_{(\mathrm{sol})} \tag{2.18}$$

Optical intensities

During this oxidation reaction, both the size and the refractive index of the transformed NPs should be modified, leading to a change in the optical scattered power. On the one hand, AgCl formed NPs should be bigger than the initial Ag NPs, with an increased radius given by:

$$r_{AgCl} = r_{Ag}\Big(\frac{M_{AgCl}}{\rho_{AgCl}}\frac{\rho_{Ag}}{M_{Ag}}\Big)^{1/3} \approx 1.36\ r_{Ag} \tag{2.19}$$

where M is the molar mass and ρ is the material density. On the other hand, silver chloride particles have a refractive index $\big(n_{AgCl}(\lambda = 587nm) = 2,067\big)$ [2] closer to the solvent than the initial silver particles $(n_{Ag} = 0.14 - 3.05i)$. Hence, we expect to detect some alterations in the observed optical power during the electrochemical reaction.

Overlaid (in black) in Fig. 2.11, we plot the recorded light scattering intensity for an Ag

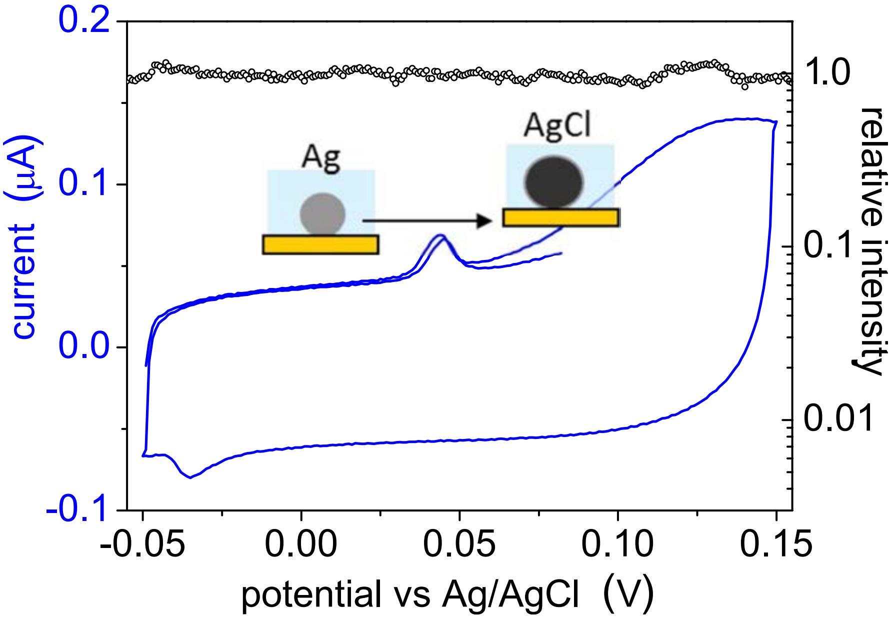

FIGURE 2.11: Voltammogram. Presence of an oxidation peak in the forward potential sweep corresponding to the oxidation of the silver NPs and the associated reduction peak in the backward sweep, indicating a quasi-reversible process. At larger voltage values, a second broad feature can be found due to the onset of the oxidation of the gold surface itself. Overlaid (in black) is the recorded light scattering intensity for the adsorbed particle tracked in Fig. 2.10

particle adsorbed on the electrode surface. From the tracking previous to its adsorption onto the electrode, the hydrodynamic radius of this particle was found to be 71 nm. Contrary to our expectations, no remarkable alteration of the measured intensity was recorded during the oxidation process. For an initial Ag NP of 71 nm radius, a Mie scattering calculation [1] gives a ratio between the initial and final scattering cross-sections of $C_{AgCl}^{scat} = 0.78\, C_{Ag}^{scat}$, which indicates an intensity decrease due to the chemical reaction when going from Ag to AgCl. Yet, we did not observe any decrease, suggesting that the two competing factors mentioned above (i.e. the change in size and composition involved in the transformation from Ag to AgCl) may compensate optically one another. The influence of the highly reflective gold electrode on the scattering cross-section of the NPs, in addition to possible plasmonic coupling of the particle with the gold surface, are likely to result in a non-linear relationship between particle size/nature and optical intensity. A detailed model of the particle/surface system (using the nature of the particle, its size and its distance to the gold electrode as parameters) is being developed by Dr. Robert Kuszelewicz (at *Université Paris Descartes*) using the Simphotonics Boundary Elements Model developed by Dr. Mondher Besbes (at the *Institut d'Optique*). This model will soon be able to predict the exact ratio between the scattering cross-sections C_{AgCl}^{scat} and C_{Ag}^{scat} in the vicinity of a reflecting surface. However, in the case of this particular experiment, the fact that the transformations under study involve agglomerates instead of single NPs may induce some error in the calculation of the transformed NP radius in

Eq. 2.19.

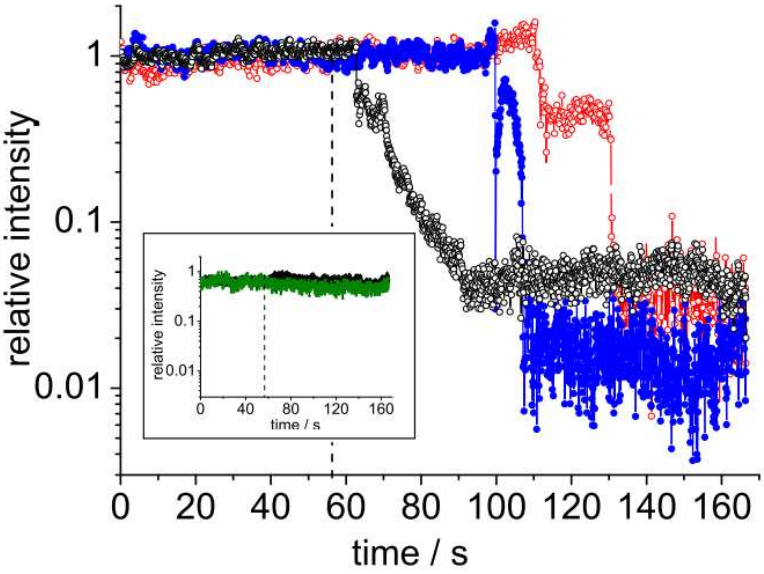

FIGURE 2.12: Scattered light intensity for three separate particles situated on the surface as a function of time. The black trace corresponds to the same particle shown in Fig. 2.10 and the vertical dashed line represents the end of the electrochemical experiment. In the insight, we show the scattered light intensity from defects in the gold electrode. The intensity of these features does not alter significantly over the experimental time frame, thus confirming that the observed decrease in intensity of the particles is not an artefact.

Figure 2.12 shows the scattered light intensity recorded for three other adsorbed particles both during and after the electrochemical oxidation. The dashed line indicates the end of the cyclic potential sweep, where many Ag particles have been oxidized into AgCl. The particles optically monitored in Fig. 2.12 do not show a significant variation in the scattered intensity during the oxidation process. Instead, the scattered light diminishes significantly only after the end of the voltammetric experiment. This decrease in the scattering intensity is attributed either to the dissolution of the electrochemically formed AgCl NPs into ions or to the formation of smaller solution-phase crystals. As these crystals are not detected by holography, it is suggested that they are smaller than 20 nm in radius. Such a chemical dissolution cannot be directly studied via electrochemical methods, as the process does not involve any electrode charge transfer, but it is clearly evidenced optically. Particularly, Fig. 2.12 shows that the dissolution process is sequential and last several seconds.

Conclusions

We have shown that the coupling of electrochemical measurements with holographic microscopy provides complementary chemical information. The ensemble response of the oxidation of surface-adsorbed Ag NPs to AgCl NPs is monitored electrochemically, whereas this process is difficult to observe optically. Conversely, the subsequent chemical dissolution of individual AgCl nanocrystals can be tracked optically due to the associated decrease in the scattered light intensity. Here the dissolution mechanism is found to be highly complex, involving chemical rather than electrochemical processes and since aggregates instead of individual NPs are concerned. These results were recently published in the scientific journal *Chemical Physics Letters* [13].

In addition, owing to the dependence of the NP optical response on its size and composition, the rate of the chemical process (evolution of the particle radius with the reaction time) could be *a priori* addressed at the level of individual NPs/aggregates. Once again, it requires the precise knowledge of the dependence of the NP scattering cross-section in contact with a highly reflecting surface, which we are currently studying. Other present motivations include the use of microelectrodes, with sizes similar to the field of view of our microscope, that would allow us to correlate the optical and electrochemical response of individual NP impacts on the electrode.

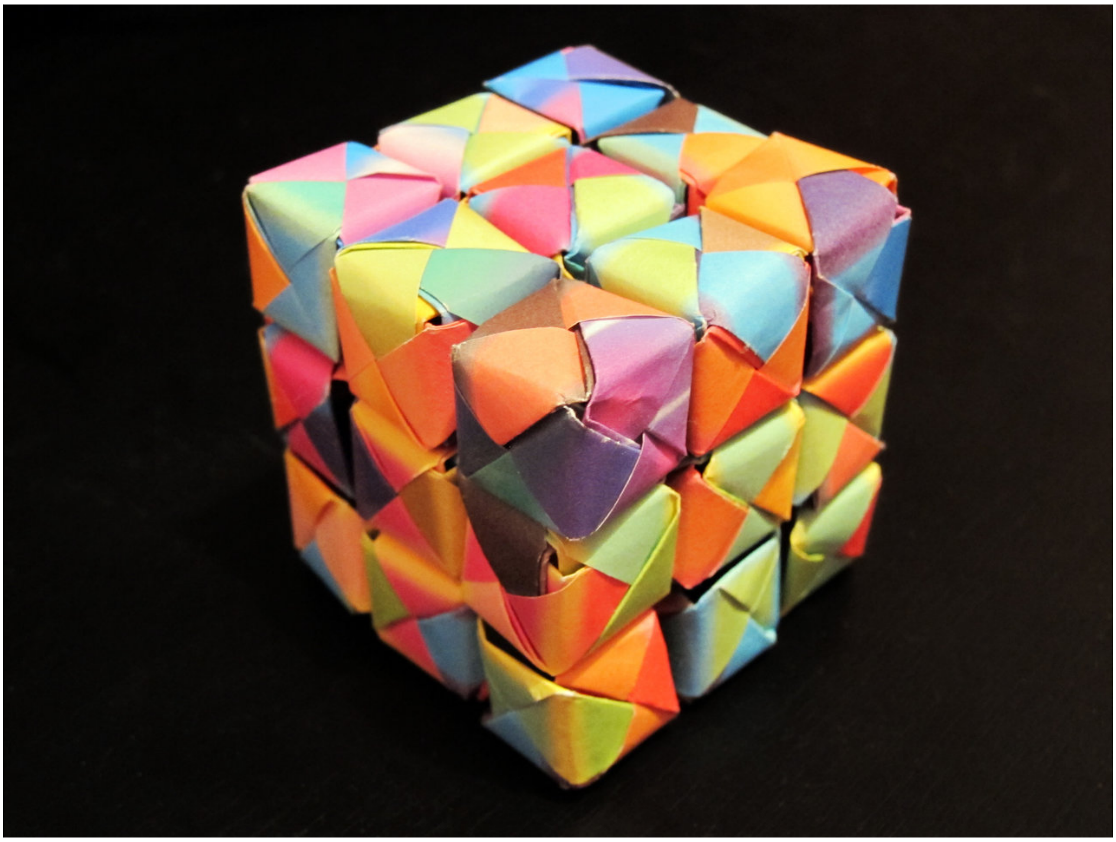

Origami cube.

Chapter 3

Holography for particle localization, tracking and superresolution imaging

As for any other wide-field imaging technique, the raw images that we obtain with holographic microscopy are diffraction-limited, meaning that we are not able to distinguish two separate point-like objects that are closer than roughly $\lambda/2$. Fortunately, there exist ways to overcome this resolution limit, enabling us to image subdiffraction objects with high position accuracy. Just last month, the Nobel Prize in Chemistry 2014 was awarded jointly to Eric Betzig, Stefan W. Hell and William E. Moerner for the development of striking sub-diffraction microscopy techniques [14, 38, 62].

In this chapter, we first review various wide-field sub-diffraction microscopy techniques based on single-particle localization. Particular attention is given to the recent achievements of digital holographic microscopy using localization methods. Then we present different strategies that have been proposed towards not only the tracking and dynamic study of single sub-diffraction objects, but also for superresolution imaging obtained point-by-point by accumulating data from thousands of individual localizations. In this context, we present our approach through the 3D imaging of metallic nanoparticles undergoing Brownian motion. Finally, we detail the methods used in this thesis work for particle tracking and we present our multiple-particle localization procedure using a fast Graphics Processing Unit.

3.1 Wide-field microscopy: beyond the diffraction limit

An optical system (in our case a microscope) does not image a point source into a point but into a 3D light distribution called the Point Spread Function (PSF). In the case of aberration-free imaging, the 2D light distribution in the image focal plane is an Airy disk. The radius of the central lobe of the Airy disk is given by Abbe's formula [3]:

$$\Delta r = \frac{1.22\ \lambda}{2\ N.A.} \tag{3.1}$$

with $N.A.$ is the numerical aperture of the imaging system, which corresponds to $N.A. = n \sin(\alpha)$, with n being the refractive index of the imaging medium and α the half-angle of collection. As a result, the transverse (also called lateral) resolution of the imaging system is limited. The only mechanisms for reducing this spot size are to decrease the imaging wavelength, increase the numerical aperture, or to use an object medium having a larger refractive index. In any case, light diffraction represents a fundamental limit. The Rayleigh criterion states that two point sources of equal intensity separated by a distance d can be resolved down to distances such that the maximum of the Airy disk due to one of the sources coincides with the first minimum of the other. In other words, we can only distinguish two sources separated by, at least, Abbe's radius (Eq. 3.1).

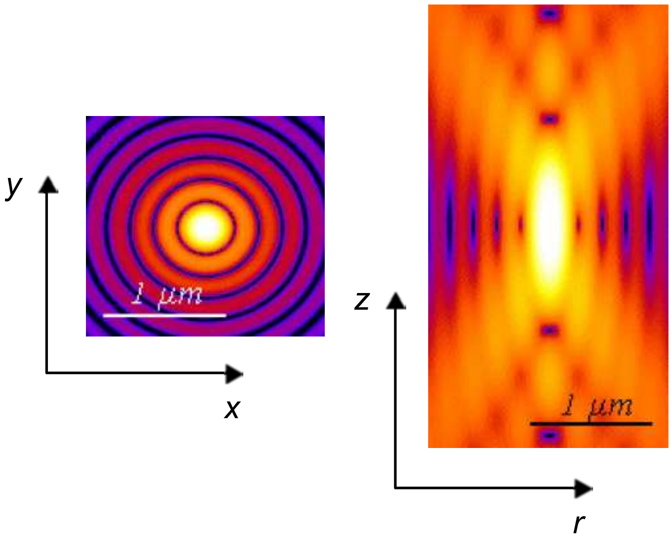

FIGURE 3.1: Image from [26]. Calculated PSF for a point-like source imaged by means of a wide-field microscope. Intensity distributions for x-y (left) and r-z (right) planes in logarithmic scale, for an emission wavelength of 520 nm; numerical aperture is 1.3 for an oil immersion objective with oil refractive index value set at 1.515.

Axial resolution (also called longitudinal resolution) in optical microscopy is even worse than transverse resolution, leading to a poor axial sectioning capability. The axial dimension of the Airy disk forms an elongated pattern (see Fig. 3.1), with a main lobe

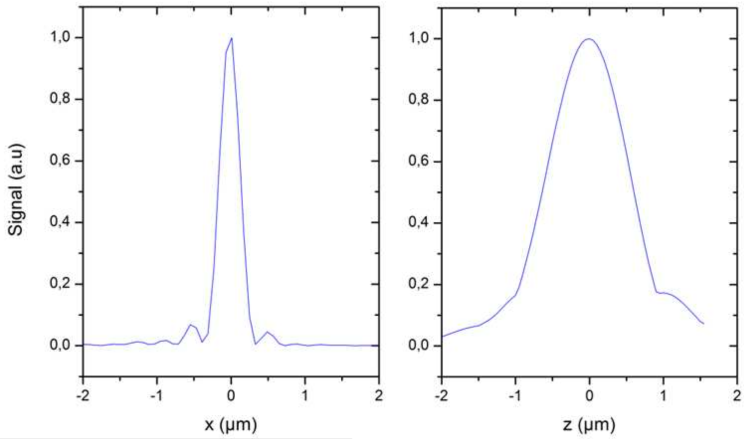

FIGURE 3.2: Experimental Intensity profiles of the light scattered by a 100 nm gold bead in the x and z-direction with our holographic microscope.

radius along the z axis of:

$$\Delta z = \frac{\lambda}{2n\sin^2(\alpha/2)} \tag{3.2}$$

It is common to measure experimentally the PSF of a microscope by imaging an individual scatterer small enough to be assimilated to a point source. Measurements of resolution usually utilize the Full Width at Half Maximum (FWHM) values of the PSF, which are slightly smaller than those calculated employing the Rayleigh criterion. Figure 3.2 shows the experimental intensity profiles obtained with our holographic microscope for the light scattered by a 100 nm gold bead in the x and z directions under an incident laser light at $\lambda = 532$ nm, using a collection objective of N.A.=0.85 and 100× magnification. In the transverse direction we measure a FWHM of about 400 nm, whereas in the axial direction it is of 1.25 μm, as expected for the PSF of our microscope objective (see Table 3.1).

Illumination	$\lambda = 532$ nm	$\lambda = 660$ nm
Objective	100× N.A.=0.85	60× N.A.=0.7
Transverse resolution (nm)	381	575
Axial resolution (nm)	1125	2312

TABLE 3.1: Summary of the expected resolution values for different illumination wavelengths and different objectives at our disposal.

The PSF depends as well on the orientation of the dipole moment of the emitting point source. Equations 3.1 and 3.2 correspond to a dipole moment laying in the imaging plane. The situation is very different for a dipole with its axis along the optical axis. In this case, the transverse PSF shows two main lobes (see Fig. 3.3) and a vanishing field amplitude on the optical axis at the image plane (z=0), which makes it difficult to define a characteristic width for the PSF [60].

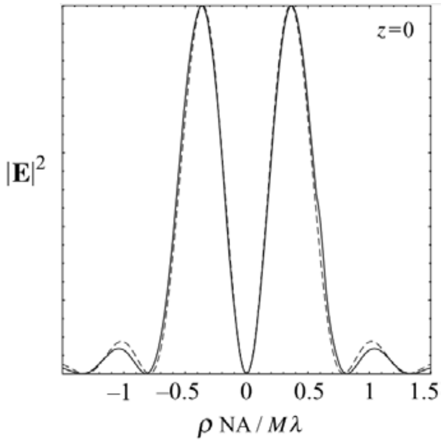

Figure 3.3: Image from [65]. Point-spread function depicted in the image plane of a dipole with moment oriented parallel to the optical axis (ρ indicates the transverse distance and M is the object magnification). The solid curve corresponds to the paraxial approximation and the dashed curve is the exact result for NA =1.4.

So far, we have considered the paraxial approximation, but exact calculations demonstrate that these expressions are a good approach for apertures up to N.A.=1.4 [65].

Despite the diffraction barrier, the Airy disk for an isolated point source can be mathematically fitted so that its central position can be determined with an arbitrary precision, limited only by the Signal-to-noise ratio (SNR). Hence, the imaging resolution can be greatly enhanced, provided we address a single point source at a time. This strategy is called localization microscopy. It is extensively used for the detection and tracking of subdiffraction objects because of its simple implementation and sub-λ accuracy. However, while the transverse PSF can easily be obtained, the axial PSF is only accessible to techniques which can provide 3D information.

3.1.1 3D localization microscopy

Most commonly, 3D information is obtained by imaging a transverse plane and inferring the axial coordinate from the transverse width of the PSF. As mentioned above, the natural PSF of a wide-field microscope being axially symmetric and quite insensitive to axial changes close to the focus, the PSF has to be modified in order to contain axial information from a transverse cut. Several methods have been used to engineer the PSF to be more responsive to axial variations, among which we can cite: lobe splitting, biplane imaging and astigmatic imaging. For lobe splitting approaches like the double-helix PSF [87] and phase ramp imaging localization microscopy (PRILM) [11], the PSF is split into two lobes whose relative distance encodes the axial position. For the biplane approach [45], the emission beam is split equally and projected onto two cameras. The focal planes in each path are calibrated to be a few hundred nanometers apart, and recorded simultaneously. In this way, two sections of the PSF with known axial offsets are provided. The astigmatic approach [39] inserts a cylindrical lens into the optical detection path, which leads to slightly different focal planes in the x and y directions. This results in elliptically shaped PSFs whose ellipticity changes with respect to z. Depending on the shape of the modified PSF, different fitting procedures are needed [70], and resolutions of 15-20 nm transversely and 40-80 nm axially are achieved [39, 45] (values expressed as FWHM). However, the axial range of these techniques is tipically restricted to a few micrometers.

In the past ten years, various research teams from the *Laboratoire Kastler Brossel-Laboratoire Charles Coulomb* (LKB-L2C) and ESPCI in Paris have buildt a solid foundation of knowledge on the 3D wide-field localization of metallic nanoparticles (MNPs) using digital holographic microscopy. Light scattering by MNPs preserves the coherence of light, thus allowing interferometric detection. This technique has been shown to be able to reconstruct the 3D image of several metallic nanoparticles, resulting in multiple PSF spots, from a single snapshot. Superlocalization can then be achieved in 3D on these PSFs with excellent accuracy with no need to modify the standard PSF of the microscope. Particularly, Warnasooriya *et al.* [100] demonstrated the ability of digital heterodyne holography to locate 40 nm gold nanoparticles in living cells environment with a position accuracy of 5 nm and 100 nm in the xy and in the z directions, respectively. More recently, the group of Verpillat *et al.* [91] was able to reconstruct 100 nm gold particles trajectories in water, evidencing the Brownian nature of the motion and determining the related diffusion coefficient.

In addition to direct 3D information, the main strength of digital holography with respect to other 3D localization techniques is that it provides a constant localization accuracy along tens or even a few hundred micrometers (see Sec. 3.1.2.2 for detail). For holographic 3D localization, two main strategies have been proposed, with similar accuracies. One approach consists in working on the hologram itself by building a numerical library of the holographic signatures of objects at different depth positions. The localization is then performed by matching the experimentally recorded hologram with the reference patterns from well-known z-positions [76, 99]. Instead, the second approach works in real space: the hologram is reconstructed into a volume prior to localizing the particle's accurate position. Although it requires an additional step, we chose this approach as it makes easier the visual identification of features or artefacts, as well as the choice of parameters with which to avoid them.

3.1.2 Holographic microscope: localization accuracy on immobilized NPs

Once the hologram has been reconstructed, we localize the particles by pointing the local maxima of the scattered field intensity. A threshold is applied to the reconstructed $I_{scat}(x, y, z)$ in the full volume of the sample in order to detect likely particles. Then, for each region above the threshold, we perform the following steps:

- We determine the reconstruction plane along z_p and the $x_p y_p$ transverse pixel for which the intensity is highest.
- Using this coarse $x_p y_p$ position, we perform a Gaussian fit in the transverse direction to localize precisely the particle transverse position, yielding its xy coordinates with subdiffraction resolution.
- We adjust a parabolic fit along the axial direction using the coarse $x_p y_p z_p$ pixel for which the intensity is maximum and the two axially adjacent pixels $z_p - 2$ and $z_p + 2$ to localize the particle axial position z of the particle with subdiffraction resolution.
- We record the intensity of the detected particle.

The ensemble of these steps yields sets of $I(x, y, z)$ values which reflect the intensity of the light scattered by each particle at a given instant in a given position, determined with sub-diffraction accuracy.

3.1.2.1 Signal-to-noise ratio

In order to study the achievable localization accuracy of our setup, we imaged gold NPs immobilized on a substrate, in air. The aim was to compare the experimentally scattered intensity and the variations of the measured positions to models. For this purpose, we fixed gold beads of 30 nm radius in a polyvinyl alcohol (PVA) matrix deposited by spin coating onto a glass slide. The bead concentration was chosen so as to obtain above-diffraction spacing between particles (average distance 10 μm). The spin coating conditions ensured a thin PVA film, with all particles lying in the plane of the glass substrate, as shown in an earlier study [4]. These slides were set onto a prism and illuminated at an angle larger than the critical angle at the glass-air interface $\theta > \theta_{c-ga} = \arcsin(n_{glass}/n_{air}) = 41.8°$ to create TIR at the PVA-air interface. The evanescent wave locally frustrated by the beads was therefore scattered into a propagative field E_S collected by the objective (Olympus ×100, NA=0.85).

Under these conditions, the bead diffraction spot spread along a 40×40 pixel area, with an integrated intensity, expressed in arbitrary units (a.u.) as given by direct camera output of 2.7×10^{18} a.u. As previously shown by Gross *et al.* [36], this intensity value can be converted to an absolute number of photo-electrons. For low light holographic images, the noise level is related to the shot noise of the reference beam and corresponds to 1 photo-electron per pixel. We thus determined the noise floor of our images by integrating the intensity of a 40×40 pixel area from the darkest region of the same axial plane containing the NPs. This relative value, measured at 4×10^{16} a.u., corresponds quantitatively to $40 \times 40 = 1600$ photo-electrons. With this simple calibration step, we obtained an absolute value of 1.1×10^5 photo-electrons scattered per particle in our reconstructed holograms. This method has the advantage of being independent of any direct optical power measurement, which is delicate for such weak signals.

The expected number of photons scattered by an individual immobilized NP under these conditions can also be expressed theoretically. For an incident laser power of 14 mW and an exposure time of $\tau_{exp} = 1$ ms, we get 3.6×10^{13} photons impinging the plane of the NPs. The total illumination area is assimilated to a uniform disk of 20 μm radius (~ 1250 μm^2). The scattering cross section of $r = 30$ nm gold particles, 4×10^{-4} μm^2,was calculated using Mie theory with the bulk optical properties of gold ($n = 0.467 - 2.41j$ at 532 nm). Thus we get 1.2×10^7 scattered photons per bead. Since the bead is located at an air-glass interface, most of the light (85%) is scattered towards the highest refractive index half-space, i.e. the glass substrate [8], and 2×10^6 photons are scattered forward within a 2π solid angle. The collection solid angle of a NA $= 0.85$ objective is ~ 0.5 Steradian. We then get 8.4×10^5 photons on the detector, yielding an expected signal of 4.6×10^5 photo-electrons (using the 55% quantum efficiency given by the EMCCD manufacturer at 532 nm), which is in good agreement with the measured values, of 1.1×10^5 photo-electrons.

The central position of a diffraction spot (and thus the position of the subdiffraction object originating it) can be determined with arbitrarily high accuracy given a sufficient number of photons in the spot. Owing to our off-axis filtering, our reconstructed images are mainly limited by shot noise. As shown by Thompson *et al.* in the case of fluorescent particles [88], each photon collected in the image gives a measure of the position of the object and its position error is the same as the standard deviation of the PSF of the microscope. The best estimate of the position of the object is then given by the average of the positions of the individual photons, with a standard error σ of the mean position μ along the z direction of

$$\sigma = \sqrt{\langle (z-\mu)^2 \rangle} = \frac{\alpha}{\sqrt{N}} \tag{3.3}$$

given that the shot noise scales with the number of detected photons N as $N^{-1/2}$, where z is the position of each photon in the spot, α is the standard deviation of the PSF and $\langle\ \rangle$ indicates the average.

With the signal level experimentally measured as discussed above, and using Eq. (3.3), we find a theoretical estimate of the error in the localization position of 0.3 nm in the transverse xy-direction and 1.2 nm in the axial z-direction.

Statistical analysis

To test this prediction, sets of 200 holograms of these immobilized beads were recorded. After reconstruction of the thin volume containing the NPs, the algorithm previously described was applied to detect the bright spots and to fit precisely each bead position in the transverse and axial directions. For each bead, we calculated the standard deviation over the successive 200 localizations in order to statistically determine our localization accuracy (see Fig. 3.4). As previously reported [91], the optimal localization precision is obtained for an hologram acquisition with particles slightly out of focus (typically ±10 μm off the optimal focusing position), as the particle scattering is encoded over a larger portion of the hologram and it is recorded by more pixels (see following subsection). At this optimal position, we found that the standard deviation was of 3 nm in the transverse xy-direction and 10 nm in the axial z-direction for a signal level of the order of 10^5 scattered photons per particle.

	Signal level (photo electrons)	Localization Accuracy with 1.1×10^5 (nm)	
		x	y
Theory	4.6×10^5	0.3	1.2
Experiment	1.1×10^5	3	10

Table 3.2: Localization accuracy summary.

This statistical limit on the localization accuracy is almost one order of magnitude bigger than the theoretical values obtained for the same signal level, that is 0.3 nm and 1.2 nm along xy and z, respectively (see Table 3.2). Our experiments were conducted on standard vibration-isolated optical tables but residual vibrations, acoustical perturbation and thermal drifts, in addition to possible unaccounted noise sources, are very likely to be the limiting factors here. However, our 10 nm accuracy value along the axial direction is still a noticeable improvement over previously reported performances for even bigger gold NPs: in Ref. [91], a precision of 70 nm was reported for 50 nm radius particles instead of our smaller 30 nm. We attribute this improvement to the higher NA of the microscope objective and to the improved PSF of refractive objectives as compared to Cassegrain objectives used in [91]. Better localization accuracies could be obtained

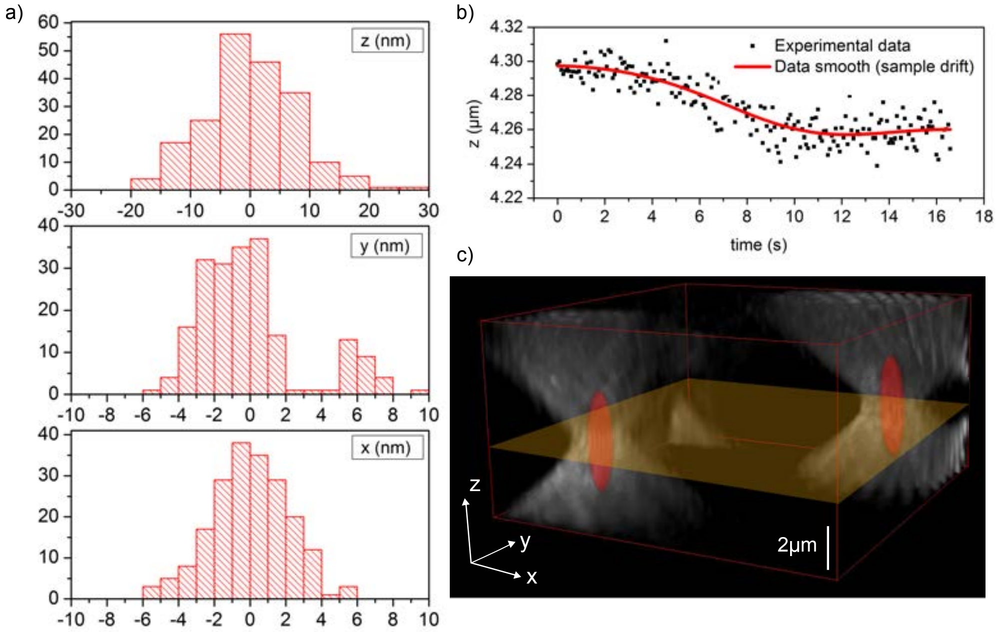

FIGURE 3.4: a) Position histograms for 200 successive localizations of the same immobilized NP. The values are centred around their mean position to highlight the standard deviation on the localization position. b) Sample defocusing during the acquisition time is corrected by subtracting a smoothed z position. c) 3D reconstructed intensity isosurfaces from a single snapshot. The shadowed gray plane indicates the position of the glass substrate.

by accumulating more photons, or adopting a heterodyne phase shifting configuration associated to a 4-buckets-based lock-in detection (see Sec. 1.1.1) to decrease the noise floor. Unfortunately, this requires that the particle stays still during the acquisition of 4 images, which is rarely possible in the case of moving particles undergoing Brownian motion, as we predominantly address in this PhD work.

3.1.2.2 Axial range

As mentioned above, the main strength of digital holography with respect to other 3D localization techniques is that it provides an excellent localization accuracy along an unprecedented large axial depth. In fact, with an holographic microscope, the localization accuracy is only limited by the degradation of the PSF by the objective aberrations when working far from the plane of best focus. Verpillat *et al.* [91] showed the localization accuracy for 100 nm gold beads as a function of the distance between the bead and the focal plane obtained with a dark-field reflecting objective of N.A.$=0.5$ and $36\times$ magnification (Fig. 3.5). While the transverse accuracy is shown to be constant ($\sim$3 nm) for $\mid z \mid < 250$ nm, the axial accuracy is about $\sim$150 nm around $z = 0$, then decreases to $\sim$70 nm for $\mid z \mid < 250$ nm. This accuracy strongly deteriorates for $|z| > 250$ μm, and for $|z| > 400$ μm, the localization of the particle is not possible because the scattered signal

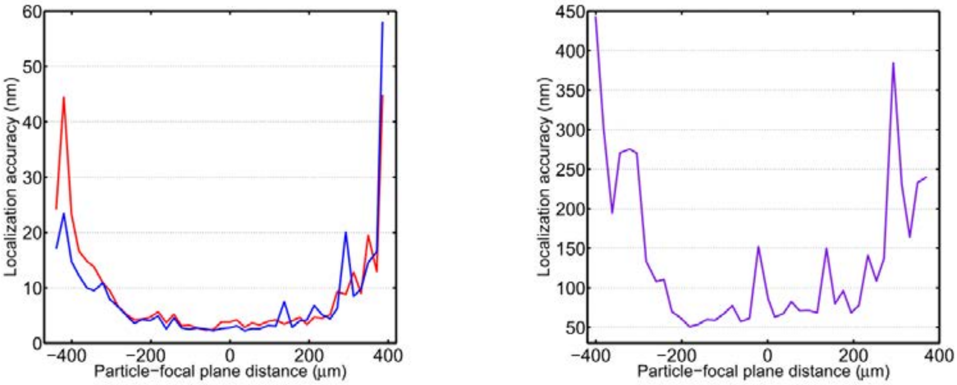

FIGURE 3.5: Figure from [91]. Localization accuracy as a function of the distance between the bead and the focal plane. (a) Transverse localization accuracy in X (blue line) and Y (red line). (b) Axial localization accuracy.

level reaches the noise level. The local maximum at $z=0$ observed on the axial accuracy curve shows that the localization is not optimal when the gold particle is the focal plane of the objective. In this case the particle is imaged on a small area of the CCD chip, so that the interference pattern spreads on a small number of pixels, which degrades the quality of the reconstruction [31]. For higher N.A., the best achievable accuracy will be improved, but the acceptable range along z will decrease. We repeated this experiment with our own holographic microscope, equipped with a transmission objective of

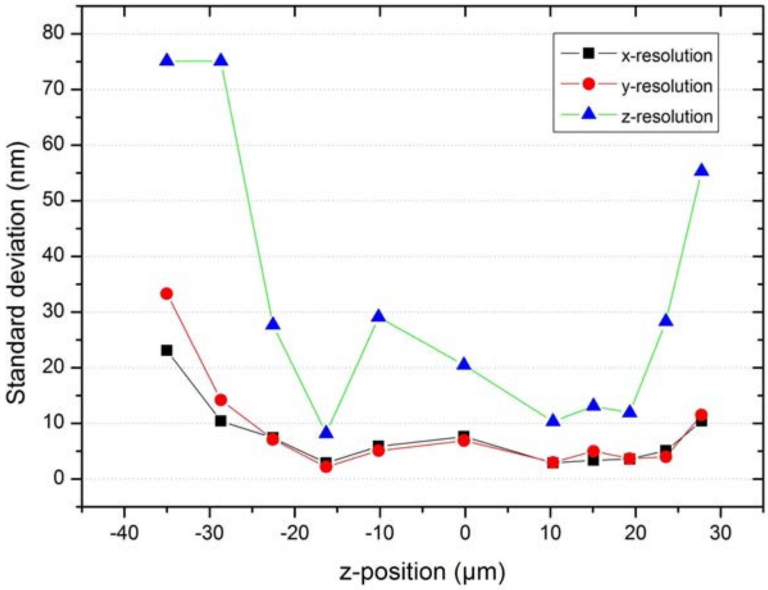

FIGURE 3.6: Localization accuracy of our holographic microscope as a function of the distance between the bead and the focal plane. Note that for values of $z < 0$ the objective was focused inside the glass coverslip, which induces a larger localization error.

N.A.=0.85 and 100× magnification. As in the previous subsection, we calculated the standard deviation of sets of 200 positions of the bead obtained from successive frames, but this time we increased the distance between the particle and the focal plane by small steps. Figure 3.6 shows our results for the localization accuracy of 100 nm gold particles under an incident power of ~ 2 mW at 532 nm and for an exposure time of 1 ms. The degradation in the axial accuracy occurs for $z = \pm 30$ μm from the focusing plane, while the accuracy in the xy plane is still an excellent 10 nm.

The accuracy achieved by our setup is thus comparable with that reached by other superresolution microscopy techniques while it has the advantage of remaining constant over a larger axial range (a few tens of micrometers instead of a few micrometers).

3.2 Superresolution imaging by point-by-point data accumulation: from 2D to 3D

3.2.1 Densely labeled samples

In recent years, numerous techniques for far-field superresolution imaging have emerged, specially using fluorescent labels. For a densely labelled sample, there exists one main wide-field localization strategy which takes advantage of the photophysics of fluorescent emitters to selectively switch on/off close-by fluorophores. Fluorescence superresolution techniques using localization methods such as Stochastic Reconstruction Microscopy

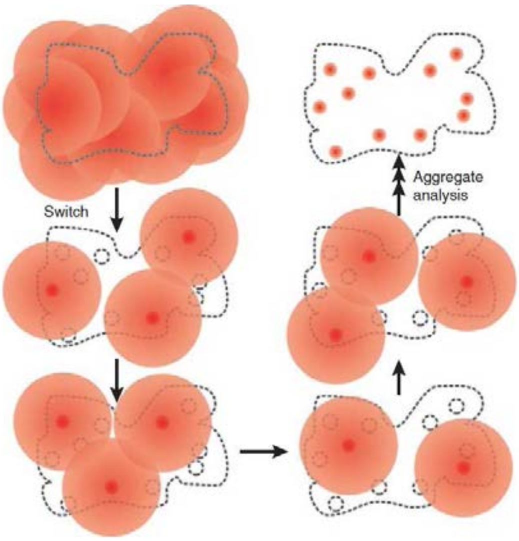

FIGURE 3.7: Image from [98]. Working principle of STORM and PALM: The sequential switching of fluorphores in a densely labelled sample allows their individual localization. The reconstruction of an image is then possible from the accumulation of thousands of individual positions.

(STORM) [74] or Photo-Activated Localization Microscopy (PALM) [15] overcome the diffraction limit by randomly activating only a sparse subset of emitters at the same time, so that they can localize very precisely the center of the Airy function coming from isolated emitters. By repeating this process several times, a computer is finally able to reconstruct a super-resolved image by accumulating data coming from thousands of individual localizations. However, the extension of these methods to 3D imaging [43, 68] is still limited to a few micrometers in depth.

An interesting alternative to fluorophores is to use metallic nanoparticles (MNPs) as markers, since they are photostable and easy to chemically functionalize. Morever, MNPs support localized surface plasmon resonances (LSPR), which can give them relatively large scattering cross sections. Recently, 2D superresolved images have been obtained using anisotropic MNPs as contrast agents [20]. Rotating the polarization of the incident light plays the same role as the random activation of the fluorophores, since LSPR of asymmetric nanoparticles are highly polarization-dependent.

3.2.2 Our approach: moving labels

Another type of strategy has been recently developed to ensure that only sparse fluorophores emit at a time in the whole field of view. This approach exploits the Brownian motion of dye molecules in a solution to let the dyes scan the surface under study in a stochastic manner [18, 77]. Here, we propose to extend this concept to metallic NPs: the random motion of these scatterers allows for a complete exploration of the sample, hence playing the same role as the random activation of the fluorophores for PALM and STORM microscopy. Besides, light scattering by MNPs preserves the coherence of light, allowing interferometric detection and therefore (provided a sufficient interparticle distance) the direct 3D localization of isolated particles.

However, imaging NPs undergoing Brownian motion is extremely challenging due to the very low number of available photons and the incessant motion of these nanoobjects. In order to obtain sharp images of moving objects, a short CCD integration time τ is essential. Over a time τ, Brownian particles travel by a distance $r(\tau) = (6D_B\tau)^{1/2}$, where D_B is the Stokes-Einstein diffusion coefficient (see next section for detail). Any distance $r(\tau)$ substantially larger than the PSF of the microscope will therefore cause a blurring of the image of the particle, effectively reducing the accuracy of the localization. Moreover, the scattering cross section of nanoparticles, which varies as the sixth power of their radius, is extremely low for small particles. In low light conditions, holography offers the possibility to increase the power of the reference beam E_R in order to increase the measured interference term $E_S E_R$ and take maximum advantage of the CCD dynamic range. The detection of small moving particles, however, remains a compromise between exposure time and particle size.

3.2.2.1 Brownian motion

Brownian motion is therefore an important selectivity mechanism in our method. It refers to the random trajectories of particles suspended in a liquid resulting from their collision with the atoms in the liquid. The particles stochastic movement can be mathematically described using the Stokes-Einstein diffusion coefficient:

$$D_{SE} = \frac{k_B T}{6\pi\eta a} \tag{3.4}$$

where k_B is the Boltzmann constant, T is the fluid temperature, η is the fluid viscosity and a is the particle radius. Knowing this coefficient, one can calculate the the average distance travelled by a moving particle during a given time interval Δt along one, two or three dimensions (see Fig. 3.8) by:

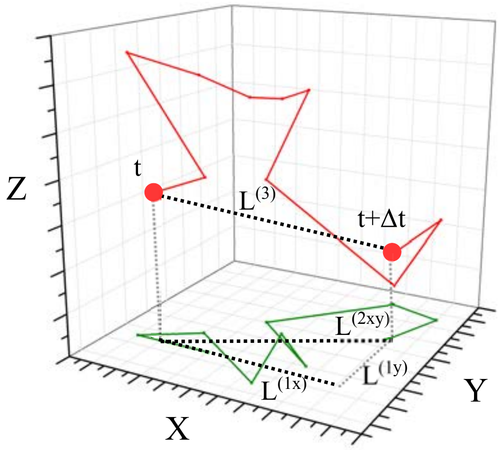

FIGURE 3.8: Average distance travelled by a Brownian particle.

$$L^{(d)}(\Delta t) = \sqrt{2d\ D\Delta t} \tag{3.5}$$

where $d = 1, 2, 3$ is the dimension.

The Brownian diffusion character of a particle can be revealed by plotting the mean square displacement MSD of the particle from its trajectory:

$$MSD(\Delta t) = \left\langle [\vec{r}(t+\Delta t) - \vec{r}(t)]^2 \right\rangle \tag{3.6}$$

where $\vec{r}$ is the particle position ($\vec{r} = (x, y, z)$) and $\langle ... \rangle$ is the time average. The MSD is therefore linear with time, with a slope $2dD$. It can be experimentally calculated by the time averaged displacements between a set of measured positions as:

$$MSD(n \cdot \Delta t) = \frac{1}{N-n} \left(\sum_{i=1}^{n-N} (x_{i+n} - x_i)^2 + (y_{i+n} - y_i)^2 + (z_{i+n} - z_i)^2 \right) \qquad (3.7)$$

with N corresponding to the total number of positions. All these parameters being well-known, we decided to track colloidal gold nanoparticles in water in order to check the reliability of our tracking. Figure 3.9(a) shows 100 data points of the trajectory of a 50 nm radius particle acquired at 40 Hz (particle followed for 2.5 s). Figure 3.9(b) shows the corresponding MSD calculation. We performed a linear regression fit over the first 10% of the data, avoiding the first point [29] and we obtained a R^2 coefficient of determination of 0.9992 and a slope of 27.88, from which we can extract a value of the radius of $r = 46,3nm$ (using a water viscosity value of 1.0 mPa.s at 20°).

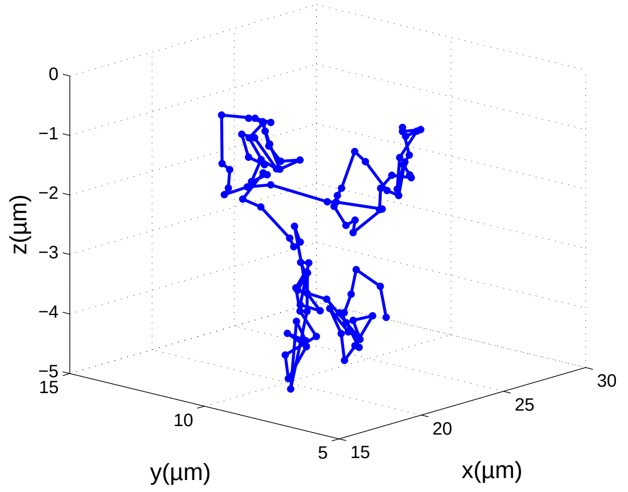

(A) 3D Tracking

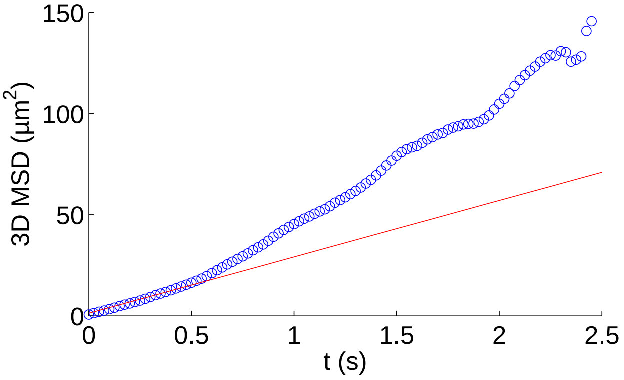

(B) MSD calculation

FIGURE 3.9: Experimental tracking of a gold NP of $r = 50$ nm radius undergoing Brownian motion.

3.2.2.2 Covering time for 2D stochastic image formation

One practical question quickly arises when using stochastically moving particles for data accumulation, that is, what should be the full duration of the experiment? More precisely, how much time do our stochastic particles need in order to visit the whole surface/volume under study? To answer this question, we collaborated with Jean-François Rupprecht, a PhD student from the *Laboratoire de Physique Théorique de la Matière Condensée*, in Paris, working on the optimization of search processes by random walk. For simplicity, we only considered here the problem of a 2D image.

In this section, we show that the answer is closely related to the coupon collector's problem (CCP) [17], which is to determine the minimal number of coupon boxes to buy in order to obtain a complete collection. Imagine for example a set of pictures of your favourite sports team. From this familiar childhood occupation, we can intuitively derive some of the consequences: when buying the first boxes of pictures, we have the impression that our collection is being filled very quickly, while obtaining the last missing pictures takes much longer to achieve. In addition, while waiting for the last pictures, we will have accumulated many doubles. The mean expected number, $\mathbb{E}\left[T\right]$, of boxes which must be purchased before we can complete one collection of N pictures is known to take the asymptotic form [30]:

$$\mathbb{E}\left[T\right] = N \ln(N) + constant \tag{3.8}$$

for the case with one coupon per box.

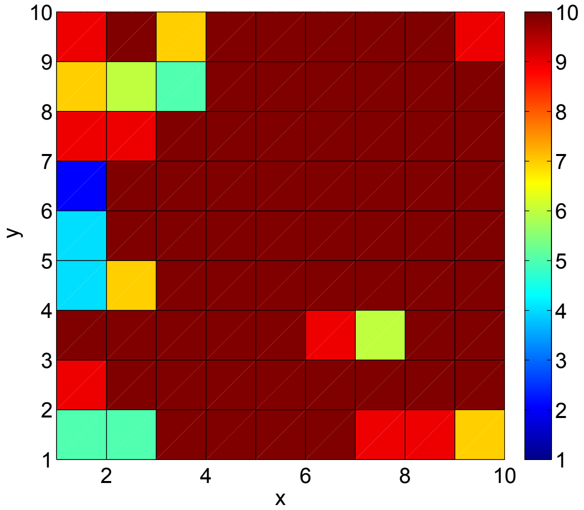

FIGURE 3.10: Map of the cumulated experimental number of observations per pixel after a 200 s acquisition (see Section 4.2.1 for experimental details). Color represents the number of particle observed in each box, each pixel counter stops when it reaches 10.

However, many subtleties need to be added to this simplified reasoning. In our case, in order to obtain a reliable measurement, every location in our image should be visited more than once, so that we can calculate an average value of the measured quantity at every point. For example, imagine that we want every pixel of our image to be visited r times before we can say that the whole 2D image is complete (see Fig. 3.10). In the coupon collector analogy, our case would not only concern a single collection with N pictures, but a group of r collectors who exchange pictures. The mean time for all of them to complete the ensemble of the r collections follows a linear relationship with r [64]:

$$\mathbb{E}\left[T\right] = N(\ln N + (r-1)\ln(\ln(N)) + constant) \tag{3.9}$$

In addition, in our case and due to the nature of Brownian motion, one particle often visits the same pixel many times, swivelling around a small region for some consecutive snapshots. To continue with the coupon collector analogy, our case would correspond to a box of pictures where there are usually many doubles. This would make us quite frustrated collectors in real life, which may explain why (to our knowledge) there has not yet been any analytical calculation to this problem.

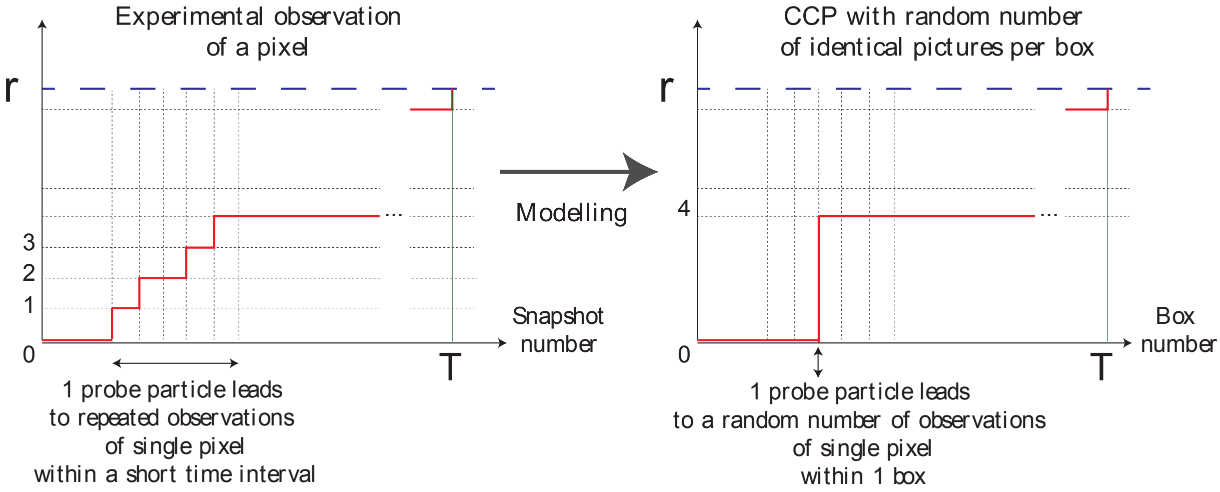

FIGURE 3.11: Scheme of our degenerated coupon collector problem.

Consequently, our aim has been to derive an expression of the full duration of the experiment for this degenerated coupon collector's problem. Rather than studying the mean time, $\mathbb{E}\left[T\right]$, we chose to study the minimum time t_θ which guarantees that each pixel has been observed r times with a given tolerance risk θ. The reasons for this choice were twofold: first, mean-time calculations for the case of $r > 1$ are complicated; second, for our experimental purposes it seemed more appropriate to calculate a given uncertainty degree rather than calculating a mean value, as the mean value can give us different uncertainties depending on the specific shape of the probability distribution.

In particular, we focus on the 95^{th} centile, a magnitude that guarantees that our time estimation is verified by a number of events larger than 95% of the total number of events. We present the mathematical development of our approach using centiles in Appendix A. We first derive an expression for the case of a single collection, analogue to Eq. 3.8, showing that we retrieve the same scaling as that of the well-known mean-time calculation approach but in an easier way. Then, we establish some hypotheses for the case of a single particle leading to a random number of observations of the same pixel (see Fig. 3.11), from which we derive our own expression for the minimum covering time t_θ that we finally compare to our experimental data.

Comparison to our experimental data

Here, we emphasize the experimental validation of our model by testing it against a statistical analysis of one of our stochastic imaging experiments. We chose to image 60 nm diameter gold particles freely moving in water inside a fluidic microchamber. With a detector surface of $N = 512 \times 512$ pixels of area 8×8 μm^2 each and a microscope objective of 100× magnification, the transverse field-of-view of our microscope objective was of 40×40 μm^2. In the axial direction, only a thin water layer of about $z = 500$ nm thickness was illuminated by means of a Total Internal Reflection configuration (see Section 4.2.1 for more details on this experiment). We thus reduced our 3D problem to 2D by considering a 2D array of voxels of volume $V = 80 \times 80 \times 500$ nm^3. In these conditions and for a low particle concentration ($c = 1.3 \times 10^9$ NPs/mL) we calculated an expected average number of particles per snapshot, μ, to be of one single particle in the whole field-of-view, $\mu = c \times V = 1$. After our post-acquisition particle localization procedure, histograms of the detection probability showed a mean number of particles per snapshot of $\mu = 0.5$, a little smaller than the expected value, most probably due to the applied optical detection threshold.

The probability p to observe a particle in a given pixel within a single snapshot was then $p = \mu/N$, provided that the considered thin volume was homogeneous and that independence from events in previous snapshots could be assured. This was indeed the case, as our stochastic particles have a diffusion coefficient of $D = 7.2$ μm$^2/s$ and showed a MSD of 1.45 μm between two snapshots, which most likely threw them out of the illuminated volume from one snapshot to the next, although they might return in subsequent snapshots.

Given these hypotheses, Fig. 3.12 shows the result of adding the observations in each pixel for different size fragmentations of our initial field-of-view (i.e. dividing the initial surface by different number of pixels N) in order to compare our theoretical model to the experiment. Variable r indicates the minimum number of observations in a pixel needed to consider the pixel as completed. Straight lines show our theoretical model of the 95^{th} centile taking into account our particular degenerated case where one particle can be observed a random number of times in the same pixel. We can see that theory matches our experimental values fairly well.

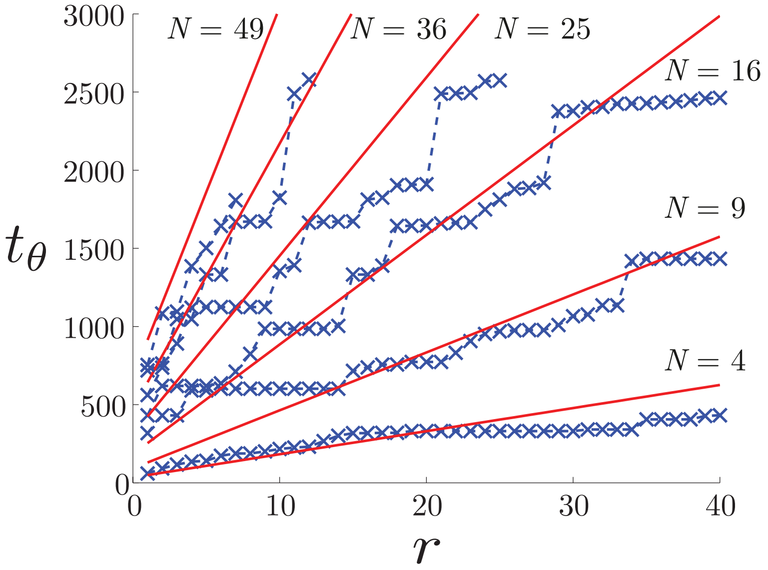

FIGURE 3.12: Minimum time t_θ (expressed in number or acquisitions) needed to collect r observations per pixel, with a variable number of N pixels. The blue crosses indicate our experimental values and the red straight lines corresponds to our model (obtained with Eq. A.15).

From this model, we can therefore extract a reliable estimation of the number of acquisitions needed to supply a sufficient amount of stochastic observations (determined by the parameter r) and for a given spatial resolution (defined by the fragmentation of the field-of-view in N compartments).

3.3 Speeding up data processing: parallel programming

A complete analysis including the hologram reconstruction and the localization of multiple particles, and repeating these steps for multiple time frames is very time consuming in terms of computation, even using recent multi-core processors. That is why we have chosen to treat our data using a Graphics Processing Unit (Nvidia GeForce GTX560), accelerating our calculations by almost two orders of magnitude as compared to classical CPU-based methods. In these conditions, the volume reconstruction and the localization of several particles is achieved in typically 200 ms per hologram.

FIGURE 3.13: Graphics Processing Unit.

A Graphics Processing Unit (GPU) is a hardware device composed of multiple processing units (also called *cores*) that can perform basic arithmetical, logical, and input/output operations simultaneously. While the main Central Processing Unit (CPU) of a computer carries out the different instructions of a computer program one after the other (i.e. in a sequential manner), GPUs are meant to conduct simple instructions in parallel on a large set of data. In particular, they were specially designed to accelerate image manipulation and display, where frequently the same instruction needs to be carried out over multiple pixels. In other words, CPUs and GPUs have significantly different architectures that make them better suited to different tasks. Consequently, an heterogeneous programming schedule that switches between sequential and parallel calculations depending on the program needs is the commonly used method.

Figure 3.14 depicts the transition from the CPU (host) to the GPU (device) for certain instructions. Inside the device, the multiple cores are gathered in blocks. The same instruction can be conducted by many blocks simultaneously. Thus, each instruction launches a determined bunch of blocks, and every core inside a block runs the same code over one memory address (in our case, a pixel).

For this thesis work, we took advantage of the hologram reconstruction program elaborated by Dr. Frédéric Verpillat, a former PhD student from the *Laboratoire Kastler Brossel*. Verpillat wrote a C++ based algorithm using a GPU and the Nvidia CUDA library to decompose the calculations on the graphics card and to copy data from the CPU to the GPU and vice-versa. His heterogeneous program aimed at optimizing the hologram's reconstruction time by attributing to the GPU all the image calculations suitable for being parallellized. As a result, this accelerated the whole data treatment by factors of many hundreds with respect to conventional 100% CPU-based calculations, enabling real-time single tracking (i.e. tracking at the same speed as the image acquisition), although performed in post-processing [91].

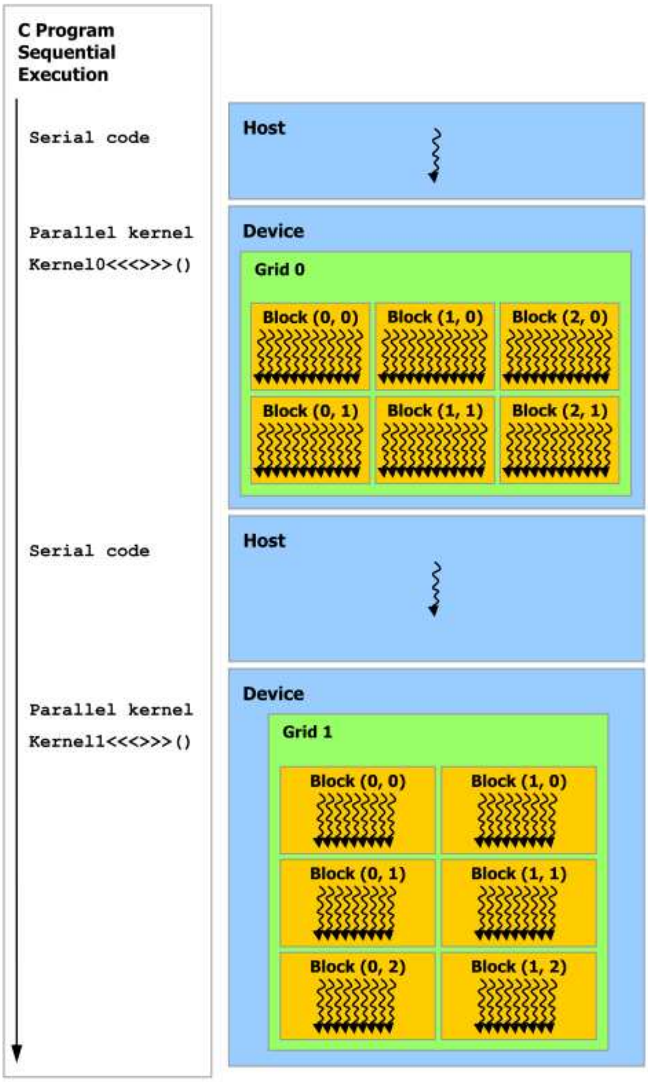

FIGURE 3.14: Heterogeneous Programming.

The program designed by Verpillat aimed at *tracking single particles*, with a manual initial designation of particle candidates by the user. However, the aim of the present work is to *localize several particles simultaneously*, so the requirements are somewhat different. In particular, in our case there is no need to track one same particle along time, since stochastic independent localizations are enough for our purpose of scanning a specific field-of-view. This means that we are not limited to short acquisition times: every Brownian particle can exit the imaged region from one snapshot to the next, which relaxes conditions on the acquisition rate. Besides, initial manual designation of the particles is not feasible, due to the huge number of individual localizations that are needed. Hence, it has been necessary to extend Verpillat's work in order to code for automatic multiple localizations, as well as adapting the reconstruction algorithm to our particular setup. In the following, we detail one small part of the parallel programming that we added to Verpillat's initial code, in collaboration with Dr. Benjamin Samson.

Although quite technical, we consider it useful to exemplify the GPU calculation power.

The fist step to automatically detect bright particles is to define an intensity threshold. As a result, for one single particle spot our thresholding step detects multiple pixels over the defined value. Consider the transverse PSF spot from one particle on one of our reconstructed images, as depicted in Fig. 3.15. The pixels with an intensity over the threshold are indicated by numbers on the figure's inset. Before we can run the subdiffraction localization of the spot center, we need to determine which pixel has a maximum intensity inside this bunch of pixels. Instead of invoking a recursive instruction to compare the intensity of each pixel with one another, we use what is called a parallel reduction algorithm. For this kind of algorithm, the characteristic working mechanism of GPU's is underlined.

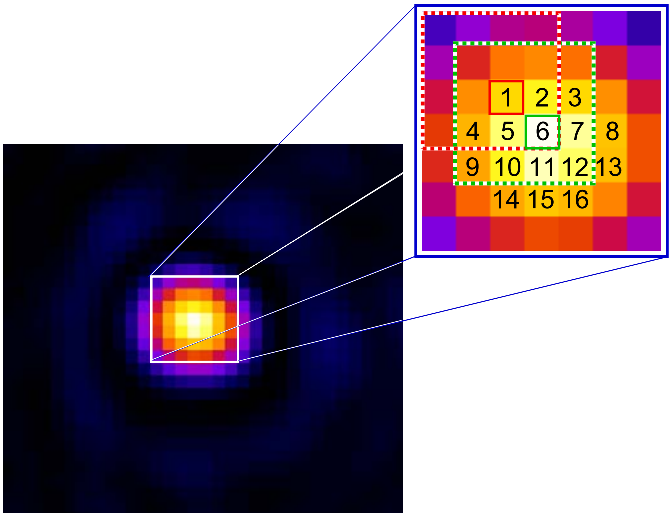

Figure 3.15: Detection of the position of the brightest pixel inside a bunch of pixels with intensities over the threshold value.

For our particular problem of finding the brightest pixel, the reduction algorithm can be imagined as a sort of origami game. We take, for pixel number 1 over the threshold, a square of size 4×4 pixels around it. We have thus a surface of 16 pixels. We then create blocks of 8 cores, as we only need 8 processors to compare two-by-two intensity values inside the 16 pixels square. Consequently, this procedure is the analogue of folding our square in two rectangular halves. Each of the 8 processors retains the position and value of the brightest of the two pixels. For the next iteration, only 4 cores are needed to compare the remaining 8 values (like in the tree-structure of Fig. 3.16), and in the next step only one half is used again, and so on.

Following the origami analogy, we keep folding the paper until only the intensity and the position of one pixel remains. For the square around pixel 1, the result will be the

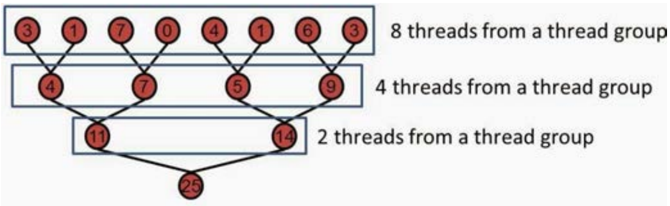

FIGURE 3.16: Tree structure.

intensity and position of pixel 6. This result will be reached in 4 steps. For a bigger square area with S pixels, the number of steps needed is thus $\log_2 S$.

For the case with 16 pixels above threshold from a single PSF spot, we run 16 times the value comparison previously described, creating a square around each pixel above threshold. It is only when the maximum value of the square coincides with the pixel being tested that we know whether it is the brightest pixel in the spot. In our example in Fig. 3.15, the maximum value for the square around pixel 1 gives pixel 6 as the output; this is not the pixel being tested, so we reject pixel 1 as the maximum pixel. Instead, the output of the investigation of the square around pixel 6 gives pixel 6 itself, as it is the brightest pixel in the spot.

This might seem a very time consuming task, but in practice it is not. As we only need a block of 8 cores from a total of 512 cores in the GPU in order to investigate one pixel, we can create $512/8 = 64$ blocks to investigate 64 pixels in parallel. With a threshold value giving 16 possible pixels per particle spot, it means that we can find the central pixel of $64/16 = 4$ particles in a 512×512 pixels field-of-view with only 4 steps. It is thus straightforward that this parallel calculation is much faster than a sequential algorithm that would investigate one pixel at a time.

Conclusion

In this chapter, we have first discussed several existing techniques based on single-molecule localization methods in order to beat the diffraction limit, mainly for accurate particle tracking. In addition, we have seen how some of these techniques use the accumulation of multiple single-particle localizations to recompose a 2D image with subdiffraction resolution. This has led us to introduce our present approach, which consists in localizing, in 3D, metallic nanoparticles in solution by digital holographic microscopy. These MNPs undergo Brownian motion, which allows them to scan the whole surface or volume under study, and can be individually localized provided they are sufficiently dispersed.

In particular, we have studied the localization accuracy obtained with our holographic setup on immobilized MNPs. For a signal level of the order of 10^5 scattered photons per particle, we have demonstrated an excellent $3 \times 3 \times 10$ nm^3 localization accuracy for 30 nm radius NPs. This accuracy strongly depends on the available illumination and could be further improved using higher laser power while staying under the particle or solvent damage thresholds. Moreover, this value of the position accuracy has been shown to remain constant over an unprecedentedly large axial range of $|z| = 40$ μm as compared to other existing techniques using fluorescent probes.

Besides, we have studied the minimum covering time necessary to recover a 2D image with our stochastically moving particles. We have statistically calculated the minimum number of snapshots by using an original approach based on centiles instead of the complex mean-time calculations, in good agreement with our experimental values. Finally, we have presented our fast particle detection algorithm, based on parallel calculations using a Graphics Processing Unit.

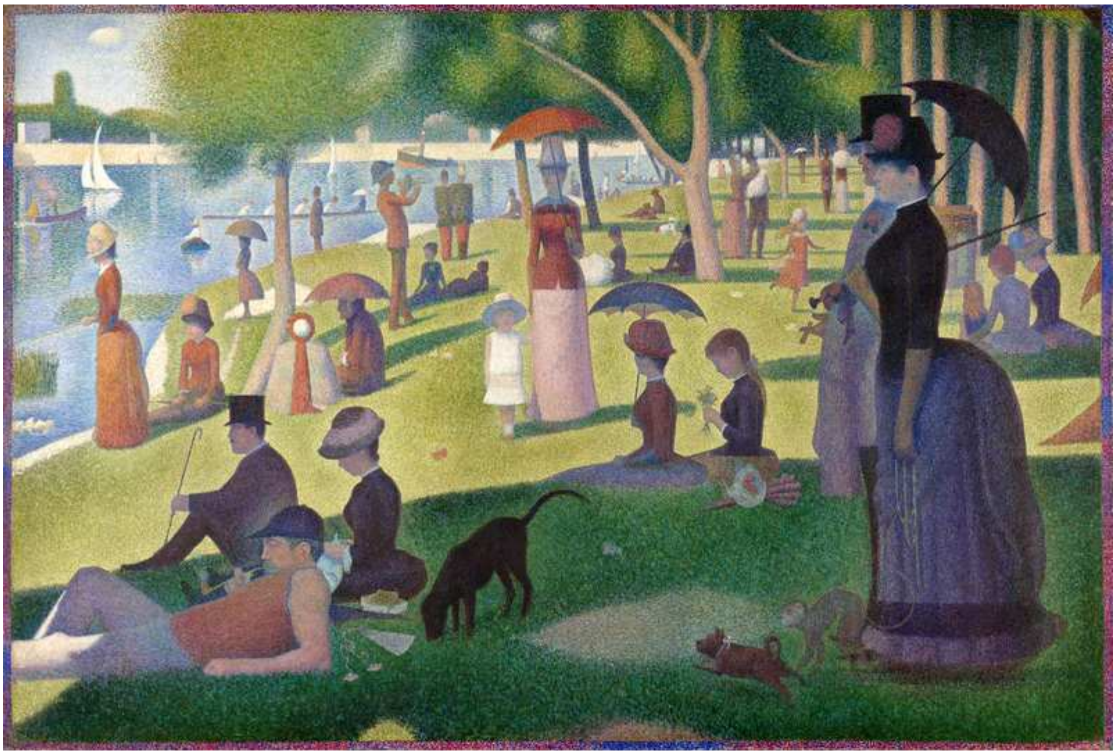

“*Sunday afternoon on the island of La Grande Jatte*”
Georges Seurat

Chapter 4

Gold NPs for superresolution stochastic optical mapping

In Chap. 1 we described the use of digital holographic microscopy for the far-field imaging of the light scattered by a nanostructured gold film in three dimensions. Although being diffraction-limited, DHM was shown to be able to extract relevant information about nanoscopic systems. In the present chapter, we focus on the main motivation of this thesis work, which is to turn this far-field, wide-field 3D imaging technique into both a superresolution technique and a near-field imaging technique. To do so, we use Brownian metallic nanoparticles as local field probes and we localize them in space in order to overcome the diffraction limit.

In order to illustrate the near-field imaging potential of our system, we then image the evanescent wave decay in a Total Internal Reflection (TIR) configuration. Finally, highlighting the large 3D volume that can be imaged with our technique, we reconstruct the intensity profile of a focused Gaussian laser beam inside a microfluidic chamber.

4.1 Framework

4.1.1 Propagating versus evanescent waves

Free-space propagation acts as a band-pass filter, since only light with wavevectors under the dispersion curve ($\omega(k) = ck/n$) of the medium are permitted. Light waves with wavevectors larger than this limit (i.e. for $k \geq n\omega/c$) are known as evanescent waves and they are forbidden in free space. Instead, evanescent waves can arise due to some inhomogeneity, such as a change of propagation medium, as is the case for Total

Internal Reflection or Surface Plasmon Polaritons. Alternatively, light diffraction by a small object may also contain wavevectors larger than $n\omega/c$, leading evanescent waves to occur. In any case, these evanescent waves remain bound to the interface or to the diffracting object which has originated them. Their surrounding electromagnetic field is then formed of a combination of propagating and evanescent waves.

Let us have a mathematical glimpse on those statements. For simplicity, we consider light propagation in air ($n = 1$). The angular spectrum representation allows us to describe a given optical field as a superposition of plane waves with variable amplitudes and propagation directions, as we already used in Chap. 1 to study the light propagation from an object to the hologram plane. Particularly, Eq.1.15 showed that the Fourier spectrum $A_z(k_x, k_y)$ of a given optical field evolves along the optical axis (z-axis) as

$$A(k_x, k_y; z) = A(k_x, k_y; 0)e^{\pm ik_z z} \tag{4.1}$$

which tells us that the Fourier spectrum in an arbitrary image plane located at $z = \text{const}$ can be calculated by multiplying the spectrum in the object plane at $z = 0$ by the factor $\exp(\pm ik_z z)$. The $+$ sign refers to a wave propagating into the half-space $z > 0$ whereas the $-$ sign denotes a wave propagating into $z < 0$. By definition, we can write k_z as

$$k_z \equiv \sqrt{k^2 - k_x^2 - k_y^2} \tag{4.2}$$

The electric field in the angular spectrum representation can then be expressed as the inverse Fourier transform of its spectrum:

$$E(x, y, z) = \iint_{-\infty}^{+\infty} A(k_x, k_y; 0)e^{i[k_x x\ + k_y y\ \pm k_z z]}\mathrm{d}k_x\mathrm{d}k_y \tag{4.3}$$

Hence, for a certain (k_x, k_y) pair, two different characteristic solutions are possible, for which the wavevector component k_z is either real or imaginary and turns the factor $\exp(\pm ik_z z)$ into an oscillatory or an exponentially decaying function:

$$\begin{array}{lll} \text{Plane waves :} & e^{i[k_x x\ + k_y y]}e^{\pm i|k_z|z}, & k_x^2 + k_y^2 \leq k^2, \\ \text{Evanescent waves :} & e^{i[k_x x\ + k_y y]}e^{-|k_z||z|}, & k_x^2 + k_y^2 > k^2. \end{array}$$

Figure 4.2a shows a schematic representation of the transverse spatial frequencies ($k_\parallel^2 = k_x^2 + k_y^2$) of plane waves incident from different angles. A plane wave propagating in the direction of z will have no oscillations in the transverse plane ($k_\parallel = 0$), whereas, in the other limit, a plane wave propagating at a right angle with respect to z will show the highest spatial oscillations in the transverse plane ($k_\parallel^2 = k^2$). Even higher spatial frequencies are possible within the domain of evanescent waves, but they are lost upon propagation from the source to the detector due to their exponentially decaying form. Moreover, the higher the spatial frequencies of an evanescent wave are, the faster the field decay along the z-axis will be.

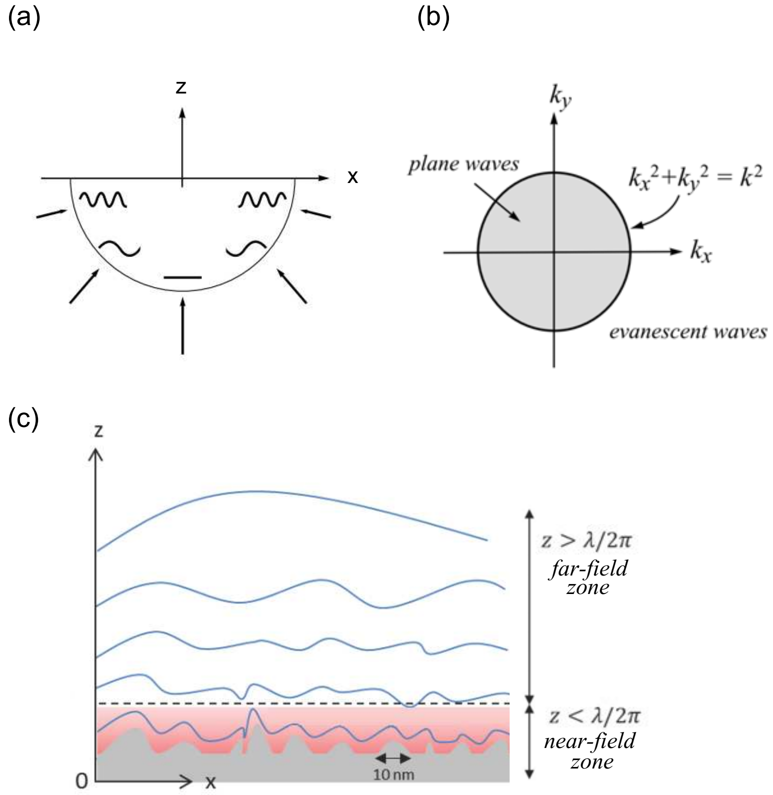

FIGURE 4.1: (a) Illustration of the transverse spatial frequencies of plane waves incident from different angles. The transverse wavenumber $(k_x^2 + k_y^2)^{1/2}$ depends on the angle of incidence and is limited to the interval $[0...k]$. (b) The transverse wavenumbers k_x, k_y of plane waves are restricted to a circular area with radius k. Evanescent waves fill the infinite space outside the circle. (c) Schematic representation of the near- and far-field zones above a rough diffracting surface. The boundary between the two regions is only vaguely defined, and it depends on the dominant wavelength λ emitted by the source.

4.1.2 Spatial resolution versus spatial frequency bandwidth

Heisenberg's uncertainty relation ($\Delta k_x \cdot \Delta x \geq 1/2$) can be interpreted in terms of microscopic imaging resolution so that the spatial resolution that can be achieved with an imaging system is inversely proportional to the available bandwidth for every spatial direction. If only propagating waves are taken into account, the maximum possible spread in the wavevector component k_x is the total length of the free-space wavevector $k = 2\pi/\lambda$, which leads to a resolution of $\Delta x \geq \lambda/4\pi$. This is very similar to the expression of Rayleigh diffraction presented in Eq. 3.1. Conversely, if one manages to retain the higher spatial frequencies associated to evanescent waves, the collection bandwidth

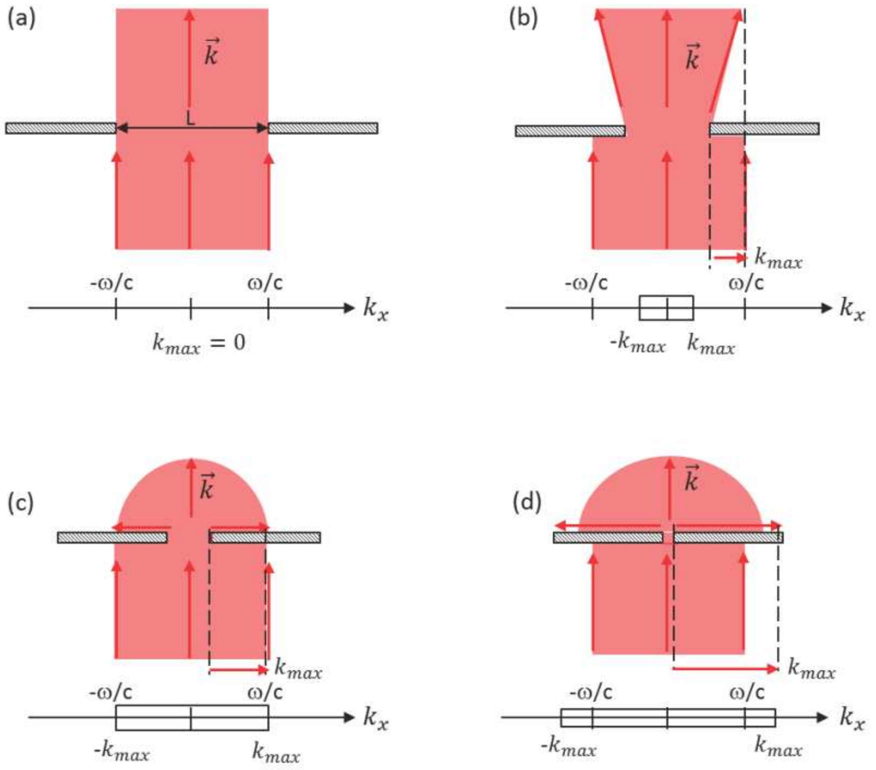

Figure 4.2: Schematic representation of the diffraction of a monochromatic plane wave by a slit of variable width, L. (a) $L \gg \lambda$. (b) $L \sim \lambda$ (c) $L = \lambda$. (d) $L < \lambda$. k_{max} represents the maximum value of the diffracted wavevector in the associated spatial direction.

of spatial frequencies increases and infinite resolution is a priori possible. However, practical limitations make the bandwidth finite.

Let us briefly analyse a theoretical example corresponding to the diffraction of a monochromatic plane wave of wavelength λ which is diffracted by a slit of variable width L. While $L \gg \lambda$, we can consider that the incident rays are not deviated by the slit (diffraction on the slit edges is negligible). Therefore, the transverse wavevector component k_x is zero. When the size of the slit becomes comparable to the incident wavelength, $L \sim \lambda$, the diffraction phenomenon over the slit edges starts to be visible. The more we reduce the slit width, the more the diffracted rays will spread. In this way, when $L = \lambda$ (which corresponds approximatively to the Rayleigh criterion), the diffracted rays spread all over the half-space above the slit and the transmitted waves thus have a transverse wavevector that spans between $k_x \in [0, \omega/c]$ or, equivalently, $k_x \in [0, 2\pi/\lambda]$. For a slit width even smaller, when $L < \lambda$, the maximum transverse wavevector is then $k_{max} > \omega/c$.

Within this 2D simplified problem, k_z can be written as $k_z = \sqrt{\omega^2/c^2 - k_x^2}$ (alike Eq. 4.2). As we have seen in the previous section, the wavevectors such that $k_x > \omega/c$ give rise to evanescent waves which remain bound to the slit surface. Consequently, when $L < \lambda$, the spectrum of the diffracted light is thus formed by a combination of propagating and evanescent waves. In 1928, Synge [86] first proposed a setup composed of a minute aperture in an opaque plate illuminated from one side like in the previous example. He stated that a sample surface placed in the near-field zone of a tiny aperture would therefore be illuminated by a light spot not limited by diffraction. The transmitted light should then be collected with a microscope. In order to establish an image of the sample, the aperture would have to be moved in small increments over the surface. Synge correctly asserted that the resolution of such an image should be limited by the size of the aperture and not by the wavelength of the illuminating light.

But how exactly would the information about subwavelength-sized structures from the surface get encoded in the diffracted radiation (propagating waves)? How is it possible at all to retrieve near-field information with a collection objective in the far-field where evanescent waves do not propagate? Actually, the underlying idea here was that, when using a confined field source with a large bandwidth of spatial frequencies to illuminate the sample, the large spatial frequencies of the sample itself are shifted. In a very simplified reasoning, we consider the case of a thin transparent sample characterized by a transmission function $T(x, y)$ (we ignore the topography as well as the specific properties of the sample). Immediately after being transmitted, the transmitted light field can be calculated as

$$E_{sample}(x, y; 0) = T(x, y)E_{source}(x, y; 0) \tag{4.4}$$

The product of T and E_{source} in direct space becomes a convolution in Fourier space. Therefore, the Fourier spectrum of E_{sample} can be written as

$$\tilde{E}_{sample}(\kappa_x, \kappa_y; 0) = \iint_{-\infty}^{+\infty} \tilde{T}(\kappa_x - k_x, \kappa_y - k_y)\tilde{E}_{source}(k_x, k_y; 0)\mathrm{d}k_x\mathrm{d}k_y \tag{4.5}$$

with $\tilde{T}(k'_x, k'_y)$ being the Fourier transform of T and $k'_{x,y} = \kappa_{x,y} - k_{x,y}$, respectively. This convolution means that the spectrum of the sample is shifted and the resulting transverse wavenumber $\kappa_{\|}$, defined as $\kappa = \sqrt{\kappa_x^2 + \kappa_y^2}$ is now

$$\kappa_{\|} = k'_{\|} + k_{\|} \tag{4.6}$$

i.e. the spectrum $\tilde{T}$ is translated by the transverse wavenumber of the source spectrum, $k_{\|}$. Hence, the large spatial frequencies of the sample are combined with the large spatial frequencies of the source field such that the difference wavevector may correspond to the far-field detection window where only propagating plane waves exist. This effect is somehow similar to the creation of the long-wavelength Moiré patterns that occur when two high-frequency gratings are shifted against each other. We can conclude that by using a confined source field with a large bandwidth of spatial frequencies, high spatial frequencies of the sample become accessible in the far-field. The better the confinement of the source field is, the better the resolution of the sample will be.

In a more realistic approach, we would need to develop a detailed model for the sample and take multiple interactions between source and sample (probe-sample coupling) into account. However, this simplified reasoning gives an intuitive idea of how the high spatial frequencies of a sample can get encoded in the propagating part of an angular spectrum. Finally, this approach qualitatively indicates that it is the source confinement what entirely defines the highest detectable spatial frequencies of the sample and thereby the resolution of the optical system. Similarly, an equivalent discussion could be held in the case of a small light-collecting device such a sub-λ aperture probe.

4.1.3 Near-field optical microscopy

The central idea of near-field optical microscopy is indeed to retain the spatial frequencies associated with evanescent waves. After the first experiments measuring evanescent waves in 1984 [57], it was soon realized that the inclusion of near-fields could not only allow for arbitrary spatial resolutions in optical imaging, but could also be of great interest for a large span of applications, ranging from fundamental physics and materials science to biology and medicine. Particularly, the strong interest in near-field optics gave birth to the fields of single-molecule spectroscopy [61] and plasmonics [35], and inspired new theoretical work associated with the nature of optical near-fields. In parallel, relying on the flourishing development of nanotechnology and nanofabrication, researchers started to tailor nanomaterials with novel optical properties, such as photonic crystals, single-photon sources and optical microcavities. The characterization of various optical near-field distributions around these new materials is thus of interest in itself, both aiming to ease the way to a better understanding of their properties as well as to improve their design for multiple applications.

In general terms, a near-field microscope is formed of a nanoscale optical probe which is raster scanned across the surface under study much as in AFM or STM. The probe can be either a pointed tip or a minute aperture which is “pounded” against the sample surface where the evanescent fields are confined (either for near-field excitation or near-field collection). The main difference between AFM/STM and near-field optical microscopy is that in the latter an optical near-field has to be created at the sample or at the probe apex before any interaction can be insured (i.e. they must provide a confined photon flux between probe and sample). However, this is at the expense of strong coupling between the source and the sample [33], a feature not present in standard microscopy where the properties of the light source (e.g. laser) are negligibly affected by the light-matter interaction with the sample. Moreover, in order to be detectable, the confined photon flux between the probe and the sample needs to have a minimum intensity. This requirement, together with the sample-probe coupling are two of the main challenges of near-field optical microscopy techniques.

There is a variety of possible experimental realizations in near-field optical microscopy. Depending on how the near-field is measured, one distinguishes between different configurations. Over the years, various techniques have been proposed, such as the photon scanning tunnelling microscope [25, 58], the near-field reflection microscope [23], microscopes using luminescent centres as light emitting sources [47, 49], microscopes based on local plasmon interaction [6, 71], and microscopes relying on the field enhancement effect near sharply pointed metal tips used as sub-wavelength scatterers [40]. All these techniques provide a confined photon flux between probe and sample.

4.2 Optical mapping by holographic localization of Brownian scatterers

As announced in the previous chapter, one of the goals of this PhD work is to develop a 3D superresoltution technique by imaging metallic nanoparticles (MNPs) undergoing Brownian motion, based on the fact that individual MNPs can be localized with a few nanometres accuracy from the optical far-field. But our purpose is not only to retrieve the accurate position of the MNPs but to utilize them to access an optical information with subwavelength resolution.

Like initially suggested by Synge [86], we propose the use of small objects to scatter light from wavevectors that were originally lost through propagation towards our far-field detector. Every Brownian MNP, when getting close to a given local field distribution, will be excited by the evanescent and propagating fields. In the case of confined evanescent fields, the MNP will scatter them, therefore coupling them to the far-field, as it is done with scattering-type NSOM techniques. For monodisperse particle sets (i.e. at fixed scattering cross section C_{scat}), the power scattered by the particle P_{scat} provides direct optical information on the local field intensity $I(x, y, z)$ at the position of the particle, since $I(x, y, z) = P_{scat}(x, y, z)/C_{scat}$ (see Sec. 2.1.3). This information gives a unique opportunity to map propagative and non-propagative optical fields with subwavelength accuracy.

Cang *et al.* [18] showed a similar technique, although limited to 2D imaging, using Brownian fluorescent molecules as local probes. They were able to map strongly localized hot spots arising at a rough metal surface by recording the fluorescent intensity as a function of the fluorophore position. However, this optical information contained in the probes' emission is often overlooked, most fluorescence studies only focusing on the presence or absence of a fluorophore at a given position.

In summary, the technique we propose here was inspired by combination of superlocalization techniques such as STORM and PALM together with near-field optical microscopies. In our case, it is the random motion of the Brownian MNPs that allows for a complete exploration of the sample, while the monitoring of their position is performed by post-acquisition superlocalization, as discussed in Chap. 3. Some of the advantages of using moving MNPs as probes instead of scanning a scattering tip include:

- Ease of use in water-based systems.
- No sample damage by the proximity of the probe.
- Weakly perturbative (as compared to an sNSOM tip supported by a comparatively large cantilever) and relatively easy to model for sample-probe coupling investigations.

Besides, the use of fluorophores instead of MNPs as local field probes presents some disadvantages, since fluorescence intensity depends on numerous parameters:

- The orientation of the electric dipole associated to a fluorescent molecule.
- The quantum efficiency of the fluorophore, related to its radiative and non-radiative decay rate. Non-radiative decay processes not being exclusively related with the incident field properties, prior knowledge of the sample characteristics is needed to account for a decrease in the fluorescence intensity (such as quenching).
- The saturation intensity, beyond which the fluorescent intensity is no longer linearly proportional to the incident field intensity.
- The eventual destruction of the dye or molecule caused by photobleaching.

Finally, the signal emitted by the fluorophores is not coherent with the incident illumination, conversely to light scattering by metallic NPs. Coherence is a great advantage since it allows one to perform heterodyne detection, useful both for the 3D reconstruction of the scattered field as well as for the amplification of the weak scattered signals by measuring the interference term $E_R^* E_S$.

Of course the electromagnetic response of MNPS to an incident field also depends on many parameters. For example, the response of the localized surface plasmons excited at the MNP strongly depends on the composition of the surrounding medium. Moreover, the coherent character of the scattered light can lead to a modulation of the measured intensity when imaging MNPs in close proximity to a highly reflecting substrate: as a function of the NP-surface distance, an interference pattern between the NP and its mirror image can arise. But these characteristic responses are arguably simpler to control than photobleaching, quenching, non-linear intensity response and dipole orientation effects linked to the use of fluorophores.

In the following sections, we present our results on the use of Brownian MNPs as local probes of the surrounding electromagnetic field. On the one hand, we chose to study the evanescent wave decay in a Total Internal Reflection (TIR) configuration, with particular interest along the decay direction. On the other hand, we investigated the field distribution around a focused laser in a large 3D volume. The following results have been accepted by *Optics Express* journal [56].

Experimental preamble

Our system can easily be adjusted to switch between a propagative and a non-propagative illumination of the colloidal particle solution. We can do so by varying the angle of incidence, θ, of the laser on the glass prism. When θ is larger than the critical angle at the glass-water interface, $\theta_{c-gw} = \arcsin(n_{water}/n_{glass}) = 62.5°$ (Fig. 4.3(a)), we create an evanescent wave decaying inside the water medium (see Fig. 4.3), while for smaller angles such that $\theta < \theta_{c-gw}$ we obtain a propagative illumination (Fig. 4.3(b)). In any case, total internal reflection conditions can be preserved at the last glass-air interface provided that $\theta > \theta_{c-ga} = asin(n_{glass}/n_{air}) = 41.8°$.

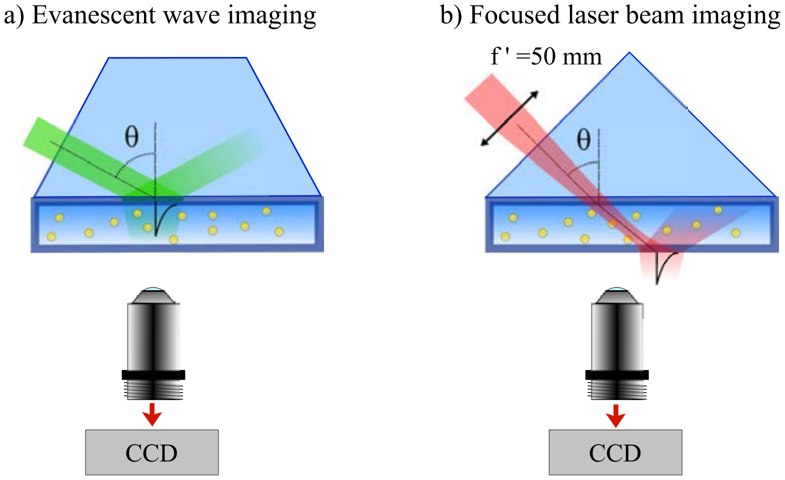

FIGURE 4.3: a,b) Microfluidic chamber containing MNPs in water. Above the glass/water total reflection angle (a), the particles are only illuminated by the evanescent wave, whereas below this critical incidence angle (b), propagative light directly illuminates the particles and is then reflected at the glass chamber/air interface. In both cases, only the light scattered by the particles is collected by the objective.

In order to prevent particles from adhering to the walls, the glass chambers were treated with Bovine Serum Albumin (BSA) and washed prior to being filled with colloidal nanoparticle suspensions. In the following experiments, we used suspensions of citrate-coated gold nanoparticles purchased from BBI, with radii of $r = 30$ and 50 nm, and initial concentrations $C = 2.6 \times 10^{10}$ and 5.6×10^{9} particles/ml, respectively.

4.2.1 Imaging an evanescent wave

A simple way to produce an evanescent wave from a propagative incident beam is to induce Total Internal Reflection at the interface between two different refractive index mediums. For $\theta > \theta_{c-gw}$, as shown in Fig. 4.3(a), all the $\lambda = 532$ nm illumination light is reflected off the glass/water interface and an exponentially decaying evanescent wave illuminates the nanoparticle-seeded water in the vicinity of the interface. In the weakly perturbative approximation, i.e. neglecting field disruption by the particles, the intensity in water is simply $I(z) = I_0\ e^{-z/\beta}$, where $\beta = \lambda/4\pi(n_s^2 \sin^2\theta - n_m^2)^{-1/2}$ is the evanescent field penetration depth, $n_s = 1.5$ is the substrate refractive index, $n_m = 1.33$ is the liquid medium refractive index, and I_0 is the incident field intensity at the glass-water interface. In our experimental conditions, the angle of incidence $\theta = 72°$ corresponds to a penetration depth of $\beta = 80$ nm.

Experiment
The glass chamber was filled with a solution of $r = 30$ nm particles with a concentration of 1.3×10^{9} particles/ml (1:20 dilution). Particle detection was achieved using a 100×, NA=0.85 objective, with adjustable correction to reduce the aberrations induced by the glass and water thickness, and imaged on the EMCCD at a frame rate $f = 20$ Hz and an exposure time $\tau = 1$ms. The position of the glass/water interface, corresponding to $z = 0$, was determined by localizing particles (or defects) fixed to the interface wall. This allowed us as well to correct for the sample drift: for every moving particle, we subtracted to the detected position a smooth of the position of the fixed particle for the corresponding time iteration (like already shown in Fig. 3.4).

In addition, in order to increase the signal-to-noise ratio when detecting moving NPs, we performed a subtraction of the background: before reconstructing the hologram, we systematically subtract the average of the ten previous frames. This step is skipped for fixed NPs, as it removes most of the scattering from immobile features in the hologram.

A series of 2000 holograms was acquired, for a total duration of 100 s. From these holograms, after reconstruction and localization, we extracted a set of 1500 localization coordinates corresponding to isolated particles at different locations and instants, and we measured for each of them the scattered intensity in the plane of best focusing, *I(x,y,z)*. Since the sample has no lateral structuring, the problem is x- and y- invariant, and the data can be reduced to a set of *I(z)* values. The 1500 measured values of *I(z)* are plotted in Fig. 4.4(a) (linear scale) and Fig. 4.4(b) (logarithmic scale), showing a general exponential decay well distributed around the expected exponential decay $I(z) = I_0\ e^{-z/\beta}$, with $\beta = 80$ nm (solid black line, no adjustment).

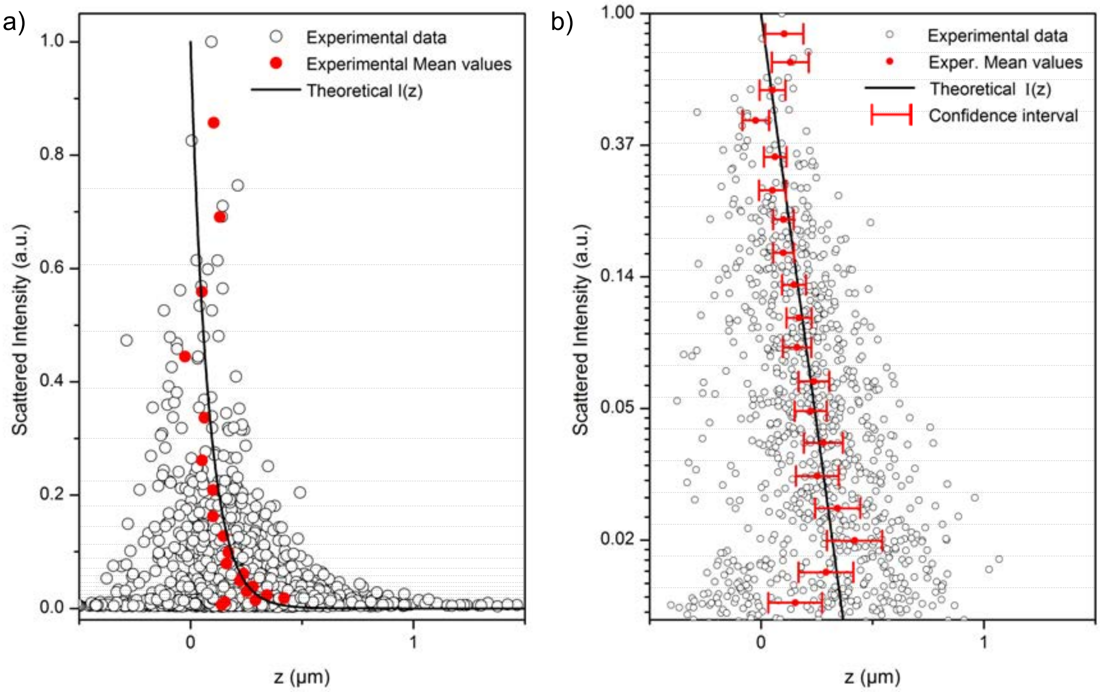

FIGURE 4.4: Normalized intensity $I(z)$ of the light scattered by $r = 30$ nm NPs represented in a) linear and b) logarithmic scale. 1500 individual localization events were extracted from a total of 2000 holograms (total acquisition time 100 s). Detection events located in the $z < 0$ region result from noise in the localization. The solid black line corresponds to the theoretically expected exponential decay ($\beta = 80$nm for θ=72°, no adjustment). In red, mean position values calculated from events inside the logarithmically distributed boxes indicated by thin gridlines. In (b), 95% confidence intervals are represented as horizontal error bars. The size of the experimental data symbols in a) is in real scale with the z axis, to give a pictorial flavour of a 60 nm NP proving an intensity decay characterized by an 80 nm decay length . Alternatively, in b) symbols are intendedly smaller to emphasize the high number of localization events.

Statistical analysis

As discussed in detail with immobilized particles, the localization accuracy is limited by the SNR of the recorded intensity. This explains the broadening, in Fig. 4.4, of the localization precision at low light levels as particles that are further away from the glass surface ($z = 0$) scatter less light. More precisely, we normalised the scattered intensity of each localized particle by the intensity of the brightest particle, assuming that the error on the localization of the latter was minimal due to its higher SNR. In the following we propose a statistical method to verify quantitatively that the stochastic $I(z)$ scattered by the nanoparticles follows indeed an exponential decay with the expected decay length, by taking into account the localization precision discussed in Sec. 3.1.2.1, which is our main source of error.

Let us call z_r the real particle distance to the surface (e.g. $z_r = 0$ corresponds to a particle in contact with the surface). Our hypothesis is that the scattered intensity, denoted $I(z_r)$, follows the law:

$$I(z_r) = I_0 \exp(-z_r/\beta). \tag{4.7}$$

Due to the uncertainty in the detected position of the particle, the measured distance to the interface is a random variable denoted Z_0. Accordingly to Eq. (3.3), we make the assumption that the error on the measured position can be written as:

$$Z_0 = z_r + \sigma = z_r + \frac{\alpha}{\sqrt{I(z_r)}}\eta \tag{4.8}$$

where η is a Gaussian noise of variance 1. The term accounting for the shot noise in the denominator of Eq. (3.3), $N^{-1/2}$, can be replaced by $I(z_r)^{-1/2}$, with $I(z_r)$ the scattered intensity by a gold particle at a real height z_r, because the number of detected photons will decrease as the field intensity seen by the nanoparticle decays. Note that, for our normalized intensity data, we assume a minimum uncertainty value on the position of the brightest particle, $\alpha\eta$.

The statistical validation for the relation in Eq. (4.7) with a specific value β relies on the following method:

1. Layer the data set into M boxes $(B_i)_{i\in[1,M]}$ according to the value of the intensity I. The width of each box should be logarithmically distributed (i.e. boxes of shorter width for smaller values of I) to ensure a fair distribution of the number of events J_i per box.

2. For each box B_i, compute the empirical mean $\hat{Z}_i$ of the detected heights $Z_0^{(j)}$:

   $$\hat{Z}_i = \frac{1}{J_i}\sum_{j\in B_i} Z_0^{(j)} = z_r(B_i) + \frac{\alpha}{\sqrt{J_i\, I(z_r)}}\eta, \tag{4.9}$$

   where the second equality is a consequence of Eq. (4.8). From Eq. (4.9), a 95% confidence interval for the value $z_r(B_i)$ is:

   $$z_r(B_i) \in \left[\hat{Z}_i - 1.96\alpha/(J_i I(\hat{Z}_i))^{-1/2},\ \hat{Z}_i + 1.96\alpha/(J_i I(\hat{Z}_i))^{-1/2}\right] \tag{4.10}$$

3. Check that the M values for $z_r(B_i)$ given by Eq. (4.8) are consistent within most of the M confidence intervals.

In Fig. 4.4, we show that the hypothesis of Eq. (4.7) is validated by the experimental data, for our theoretical penetration length of $\beta = 80$ nm. Grid lines in both figures show the $N = 20$ boxes, logarithmically distributed, used to compute the empirical mean values $\hat{Z}_i$. In the logarithmic plot (Fig. 4.4(b)) we have represented the confidence interval for each mean value: the only values not matching the theoretical exponential decay within a 95% confidence are those for very high and very low intensities. For very high intensities, it is due to the scarce number of events to compute the mean position; for low light intensities, the detected positions are not reliable any more and other low scattering artefacts may have been detected by our localization algorithm instead of nanoparticles.

4.2.2 Imaging a laser beam distribution

The previous analysis neglected the x- and y-dependence of the intensity, since there was no lateral structuring in the geometry of the system. In order to illustrate the 3-dimensional abilities of the technique, we investigate here the case where the angle of incidence $\theta_{c-ga} < \theta = 45° < \theta_{c-gw}$ allows light propagation inside the water-filled chamber (see Fig. 4.3(c)). This light is then reflected off the last glass-air interface, preserving a dark-field illumination. The experiment was conducted on a similar setup, using an illumination wavelength of λ= 660 nm from a laser diode (Opnext HL6545MG, max. power 120 mW). The diode was expanded by a collimated telescope and focused inside the microfluidic chamber with a $f' = 50$ mm converging lens.

Without nanoparticles, no light propagation occurred beyond the sample in these dark-field conditions and the laser beam was not observable. A colloidal solution of 50 nm radius particles with a concentration 5.6×10^8 particles/ml (1:10 dilution) was used to scatter light to the microscope objective (Olympus 60×, NA 0.7, adjustable coverslip correction) and the camera. The holographic detection of the particles on a dark background was repeated over 6000 holograms acquired with an integration time $\tau = 1$ms and a frame rate of 12 Hz, for a total recording time of 8.3 min. After processing with a detection threshold fixed at 45 times the background intensity (average signal measured in regions devoid of any particle) in order to avoid false detections, 36000 localization events were obtained. On average, 6 nanoparticles were therefore detected simultaneously in the volume reconstructed from each hologram. The corresponding (x, y, z) positions are shown in Fig. 4.5(a), with intensities $I(x, y, z)$ coded by the size of the dots.

Although the whole microchamber was filled with Brownian nanoparticles, only those which passed through the propagating laser beam were detected, and the scattered

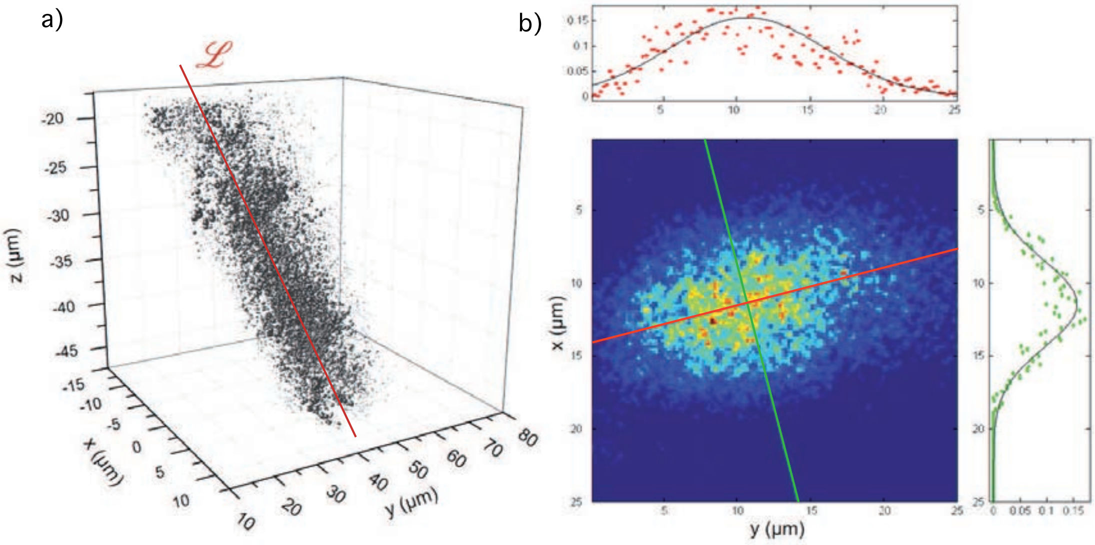

FIGURE 4.5: a) Position of 36000 localization events detected when illuminating gold particles 50 nm in radius in Brownian motion in water, with a $\lambda = 660$ nm diode laser beam. The intensity $I(x, y, z)$ recorded at each location is represented by the size of the spheres. The red line $\mathcal{L}$ corresponds to a 3D linear regression on the positions and indicates the direction of the laser beam. b) Projection of the values $I(x, y, z)$ onto a plane perpendicular to the propagation axis, $\mathcal{L}$. The two axis of the laser diode beam are clearly identified (red and green lines). Fitted profiles along these axis allow the retrieval of the Gaussian characteristics of the beam (see text).

intensity was stronger when the particle was close to the center of the beam. The beam propagation axis was determined by a 3D linear fit on the whole set of coordinates (x, y, z), as indicated by the red line $\mathcal{L}$ in Fig. 4.5(a).

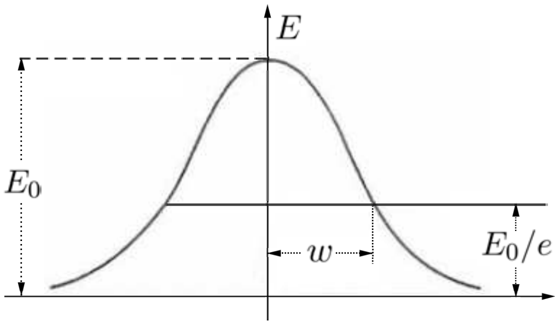

FIGURE 4.6: Amplitude distribution of the fundamental mode of a Gaussian beam.

The lateral properties of the beam can also be investigated. Due to our sparse experimental values, which reflect the stochastic character of our sampling methods, plotting a single cross-section perpendicular to propagation axis $\mathcal{L}$ leads to a very noisy image, some regions containing several particles, others none. To avoid this, we calculated the average intensity of the 3D dataset along 60 μm in the propagation direction. Since the focused Gaussian beam considered here has an almost constant profile along its Rayleigh length around its region of best focusing ($2 \times q_{out,\perp} = 84$ μm and $2 \times q_{out,\parallel} = 216$ μm, see calculation below and Fig. 4.7), this average does not have much influence in the experimental determination of the beam waist. Laterally, the (x, y) data were binned in 200 × 200 nm boxes in order to obtain an image exempt of empty pixels, resulting in Fig. 4.5(b). This 2D image clearly reveals the elongated mode structure characteristic of laser diodes. Indeed, the laser diode manufacturer indicates a high degree of astigmatism of the fundamental mode, with values for the beam divergence angle of $\theta_{\parallel} = 7.5°$ along its main axis and $\theta_{\perp} = 15°$ in the perpendicular direction.

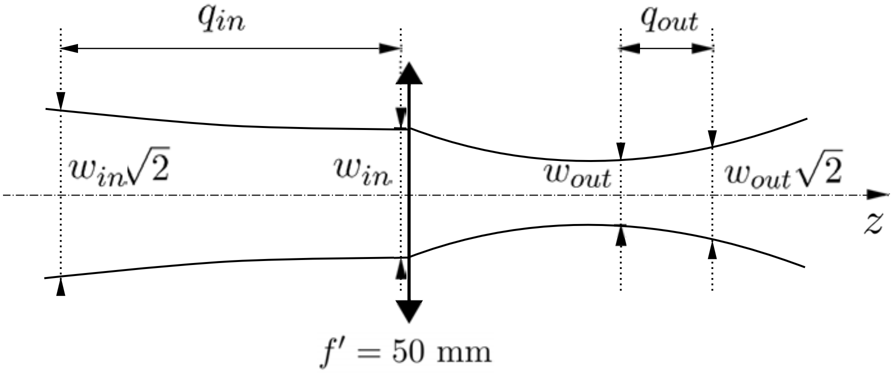

FIGURE 4.7: Schematic of the contour of our Gaussian beam before and after the focusing lens.

To quantify these values of beam asymmetry from our data, we fitted this 2D z-averaged cross-section to a 2D Gaussian asymmetric centroid by means of least-squares calculations, obtaining two profiles along its minor an major axis (green and red lines in Fig. 4.5(b)), which yield the experimental values of the waist of the focused beam along the main axis and perpendicular to it, $w^{exp}_{out,\perp} = 5.3$ μm and $w^{exp}_{out,\parallel} = 2.9$ μm, respectively.

In order to estimate the size of the focused beam inside the microfluidic chamber, we first measured the size of the beam waist after the telescope, i.e. at the input of the focusing lens, using a beam analyser (Thorlabs BC106N-vis): $w_{in,\perp} = 2.2$ mm and $w_{in,\parallel} = 3.5$ mm, for the two axis of the elliptic mode. After the focusing lens, the size of the emerging Gaussian beam can be calculated in the plane of best focusing as [24]:

$$w_{out}^2 = w_{in}^2 \frac{f'^2}{f'^2 + q_{in}^2} \tag{4.11}$$

where $q_{in} = \pi w_{in}^2/\lambda$ is the Rayleigh length of the beam before, and q_{out} after the lens:

$$q_{out} = q_{in} \frac{f'^2}{f'^2 + q_{in}^2} \tag{4.12}$$

Using Eqs. 4.11 and 4.12, and neglecting beam distortions induced by the thin microfluidic chamber and its water content, we obtain the expected geometrical parameters of the beam inside the chamber at the output of the $f' = 50$ mm lens: $w_{out,\perp} = 4.8$ μm,

$w_{out,\parallel} = 3$ μm and $q_{out,\parallel} = 108$ μm, $q_{out,\perp} = 42$ μm. These values are indeed in good agreement with the measured values, $w^{exp}_{out,\perp} = 5.3$ μm and $w^{exp}_{out,\parallel} = 2.9$ μm, the main source of error being attributed to the determination of best focusing region in the 3D plot.

4.3 Present challenges: optical mapping around nanostructures

One major goal of the present work is the characterization of the electromagnetic field distribution around plasmonic nanostructures with subwavelength resolution. Particularly, thanks to our 3D superresolved imaging technique with large depth of view, we aim at bridging the gap between near- and far-field characterizations. So far, the distinctive photonic and electronic hybrid character of plasmonic nanoantenna resonances has suggested analysis techniques using either photons, electrons or a combination of both. Among the different existing optical techniques, the most extensively used are NSOM techniques, previously presented. As already mentioned, these techniques introduce a non-negligible amount of perturbation, complicating interpretation of the data. Moreover, NSOM techniques are hard to implement in water-based systems due to tip oscillation damping, although there exist some successful attempts [69]. Other optical state-of-the-art techniques for probing electromagnetic fields around plasmonic nanostructures are nonlinear photoluminesce techniques [34]. Although being subdiffraction, their intrinsic resolution is poorer than NSOM. Alternatively, there exist analysis techniques involving electrons as probes, as it is the case for cathode luminescence imaging [96], electron energy-loss spectroscopy (EELS) [63] and photoemission electron microscopy (PEEM) [27], which offer high spatial resolution but require vacuum environments. The local electromagnetic characterization of plamonic nanostructures in water-based systems, present in many emerging microfluidics studies, is therefore inaccessible to electronic microscopy. Moreover, all of these techniques require some sort of sample or excitation scanning, slowering down the acquisition rates.

Our approach using MNPs as stochastic probes thereby presents many advantages. The main obstacle, however, is the light scattered to the far field by the plasmonic object itself. Conversely to techniques using fluorescent probes, for scattering probes the excitation and detection wavelength remains the same, hindering a simple filtering. In the best case, this parasitic light simply degrades the detection of the metallic nanoprobes after the hologram reconstruction, deteriorating the probe's localization accuracy. In this case, post-processing image treatments such as DC background subtraction are sometimes helpful. But in the worst-case situations, stray light prevents us from detecting the nanoprobes at all, the dynamic range of the CCD being insufficient to detect both the strong parasitic light and the weak scattering from the nanoprobes. This fact tells us that we actually need to remove this unwanted light at the acquisition stage.

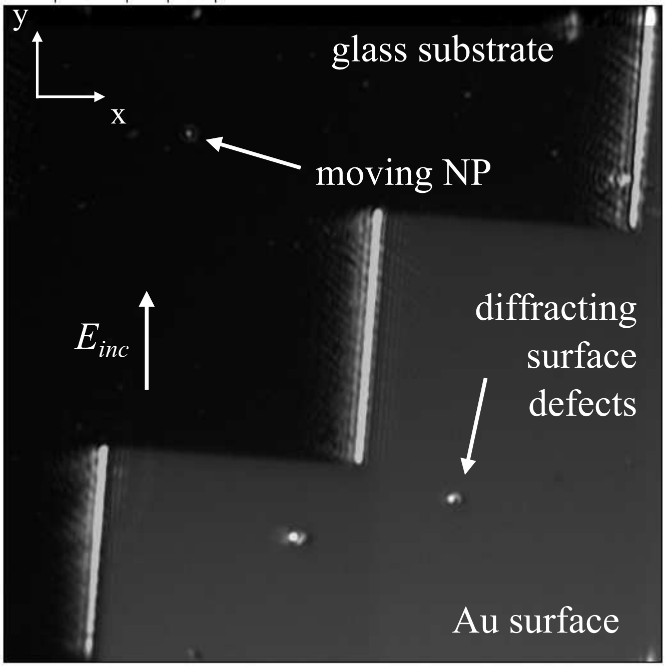

FIGURE 4.8: Imaged region of a sample composed of a gold layer, 70 nm thick, evaporated on top of a glass surface. We have overlapped the holographic reconstruction and the white light image for clarity. The sample is immersed in a colloidal solution of 80 nm diameter gold NPs. Note that the edge of the gold layer which is parallel to the incident polarization shows very strong scattering, almost blinding the CCD camera, and even small defects on the gold surface show stronger scattering than the moving probe NPs.

4.3.1 Background suppression

In order to overcome this problem, we have adopted two different strategies. The preliminary results are discussed in this section. Both alternatives rely on the differentiation of each type of scattering: that from static, generally bigger features, from the scattering of small moving NPs. With the first approach, we propose a spatial frequency-filtering by means of a circular mask placed at the back focal plane of the collection objective. In the second approach we use heterodyne holography, with a heterodyne offset frequency shifted so as to detect the Doppler-shifted light scattered by moving particles.

4.3.1.1 Fourier space spatial filtering

In the experiments shown in the preceding chapters, only NPs in liquid were imaged. The use of a glass prism and an oblique incidence angle of illumination were shown to provide a dark background, greatly enhancing the visibility of the faint NPs scattering. However, when trying to image a diffracting object, the oblique incident light is diffracted into the collection objective not only by the probe NPs, but also by the object under study.

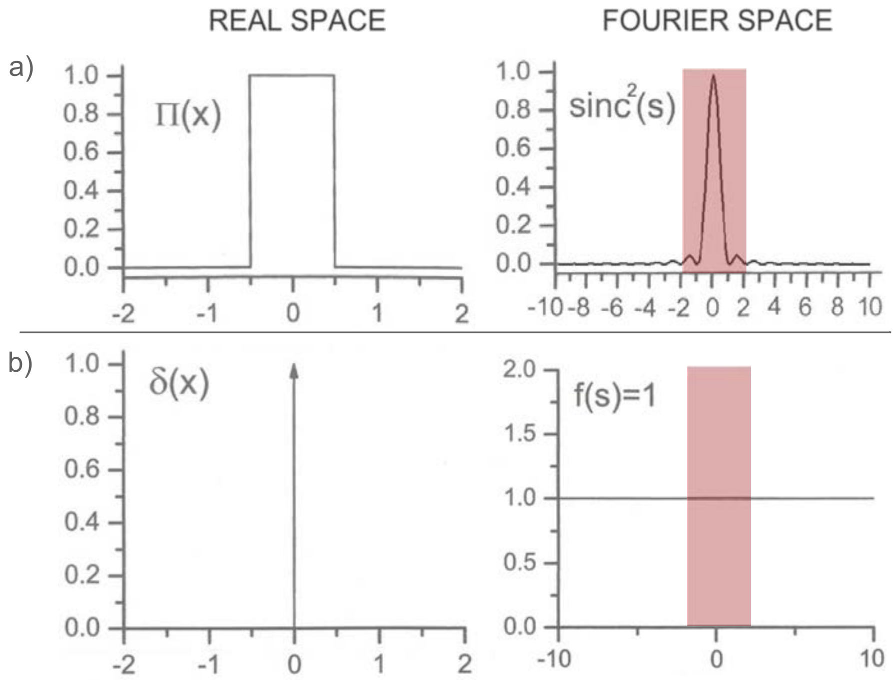

FIGURE 4.9: Theoretical diffraction pattern of a given object (a) of finite size (e.g. of rectangular shape) as opposed to (b) a point-like object. The red shadowed area on both diffraction patterns schematically represents the amount of intensity removed from each of these diffracting features when performing the same spatial filtering in the Fourier space.

The theoretical diffraction spectrum of a given object can include any possible spatial frequency k_x. As opposed to light in a transparent medium, for which the spatial frequencies are bound between $k_x = [0, n\omega/c]$, the spatial frequency spectrum of a diffracting object can include every frequency from $k_x = [0, 1/L]$, L being the dimension of the object. In this way, the smaller the object is, the higher spatial frequencies it diffracts. The structures under study being larger than our probe NPs, we suggest to perform a low-frequency filtering. Figure 4.9 shows the theoretical diffraction pattern of a rectangular object of finite size as opposed to the diffraction pattern of a point-like object. The red shadowed area on both diffraction patterns schematically represents the amount of intensity removed from each of these diffracting features when performing the same spatial low-frequency filtering in the Fourier space. The filtering will definitely remove part of the light coming from the point-like probes, but we expect it to have a stronger impact on the background light coming from bigger structures, for which the diffraction frequency bandwidth is narrower.

For this purpose, we first decided to perform a numerical ring filtering in the Fourier plane in order to study the deterioration of the reconstructed image and the localization accuracy as a function of the inside mask radius, R_{in} (see Fig. 4.10). The outer radius, R_{out}, is kept constant and its value corresponds to the size of the +1 diffraction order after the first FFT calculation, which is linked to the N.A. of the microscope objective. For our 100× magnification objective with N.A.=0.85, R_{out} measures 70 pixels.

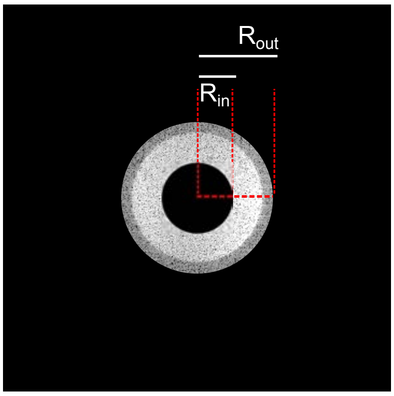

FIGURE 4.10: Ring filtering on the +1 diffraction order.

On the one hand, Fig. 4.11 shows the intensity profiles of immobilized gold NPs of 30 nm in diameter (same experimental data from Sec. 3.1.2.1) as a function of the inside mask radius used in the reconstruction process. For the transverse profile (Fig. 4.11(a)), this ring filtering has the particularity of shrinking the main lobe of the PSF. In fact, for every value of R_{in}, the resulting PSF is the outcome of the subtraction between our regular PSF ($R'_{in} = 0$, $R'_{out} = 70$ pixels) and a wider PSF corresponding to a smaller numerical aperture obtained with $R''_{in} = 0$ and $R''_{out} = R_{in}$. In terms of localization accuracy, this narrowing seems to compensate for the decrease in the number of detected photons, which explains why the final transverse localization accuracy does not worsen much with the ring filtering. On the contrary, the axial intensity profile broadens for higher R_{in} values. This broadening, together with the decrease in the remaining photon number for the reconstruction, leads to a gradual deterioration in the axial position accuracy.

On the other hand, we studied the influence of the numerical ring filtering on the intensity of holographic images containing different diffracting features. Figure 4.13 shows the reconstructed images of a 70 nm gold layer where five crosses were fabricated by lithography to work as markers, measuring 1 × 1 μm. These kind of markers are usually present when fabricating nanostructures for wide-field microscopy studies, so that

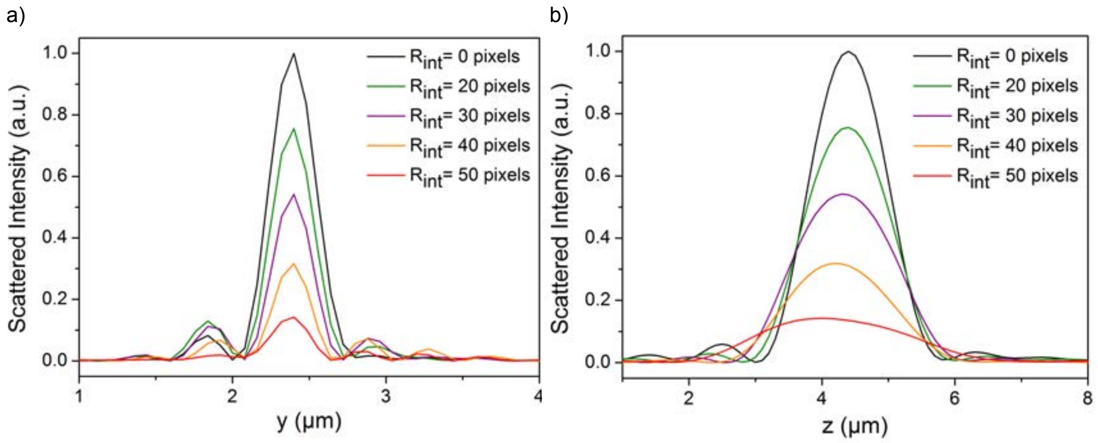

FIGURE 4.11: Intensity profiles of immobilized 30 nm diameter gold NPs (same experimental data from Sec. 3.1.2.1) as a function of the inside mask radius R_{in} used for the numerical ring filtering in the Fourier plane during the reconstruction process.

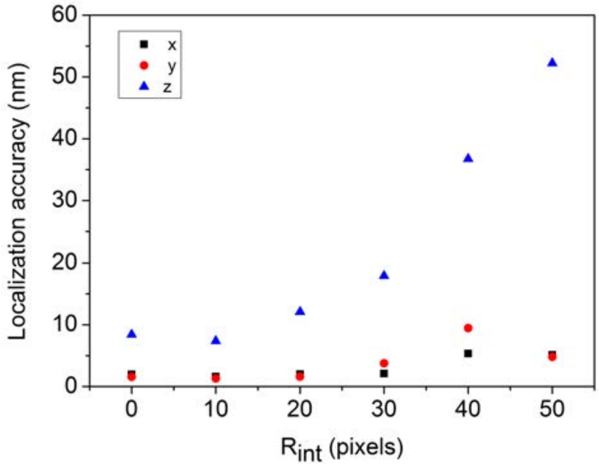

FIGURE 4.12: Localization accuracy of immobilized 30 nm diameter gold NPs (same experimental data from Sec. 3.1.2.1) as a function of the inside mask radius R_{in} used for the numerical ring filtering in the Fourier plane during the reconstruction process.

nanoobject under study can be easily located. Between the two upper and the two lower crosses, a 40 nm diameter hole was drilled. We analysed the decrease in the light scattered by these two features, very different in size, for different values of the inside mask radius. Measured as a percentage change, the results confirm that the intensity of the larger feature decreases more rapidly than for the nanoobject, especially for small R_{in} values. However, the difference in the decrease rate is not striking and a compromise has to be found between improving the intensity contrast while keeping a reasonable localization accuracy. An inner value of 20 pixels, for example, allows us to reduce the scattering intensity of the micron-sized diffracting feature by 20% while the nanoobject intensity is only reduced by 4% and the localization accuracy in the three dimensions remains fairly unchanged.

Experimentally, in order to block out the central light in our transmission configuration,

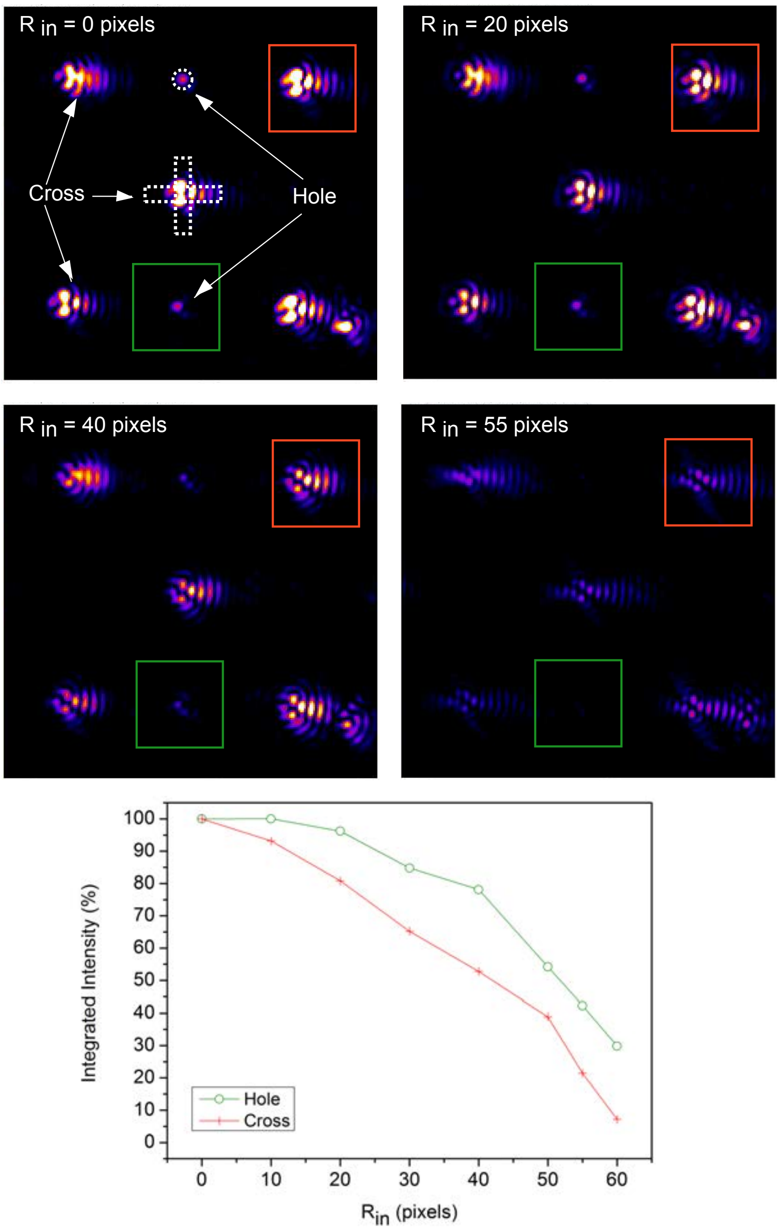

FIGURE 4.13: Holographic reconstruction (at the plane of best focusing) of a gold layer in which five micron-sized crosses (selected in red) have been lithographed to work as markers of the position of two nanoholes (selected in green). The integrated intensity of the two selected regions is plotted as function of of the inside mask radius R_{in} used for the numerical ring filtering in the Fourier plane during the reconstruction process.

we could have used a reflecting Cassegrain-type microscope objective as in Ref. [91]. With such objectives, the central part of the collected light is masked by the secondary mirror and low spatial frequencies are avoided. This mirror-based objectives have the advantage of being broadband (which is unnecessary with our monochromatic setup) but they suffer from image aberrations, provide poor numerical apertures and consequently broader PSFs as compared to traditional microscope refractive objectives. Therefore we chose to keep our refractive objective of 100× magnification and N.A.=0.85, equipped with a correction ring to compensate for the aberrations when imaging through a glass coverslip, for which we have already studied the localization performances in Chap. 3.

We fabricated a mask out of a circular piece of aluminium (3 mm in diameter), painted in black to avoid reflections. Our aim was to place it close to the back focal plane of the objective, therefore allowing only oblique rays to reach the detector. Figure 4.14 shows two experimental attempts at centering the mask. First, we glued the circular mask to a fishing thread and fixed it to the microscope turret where the objectives are screwed. This way we could change objectives without having to move the mask. But although the screw is very close to the rear face of the objective, its image in the reconstructed Fourier plane was blurred (see Fig. 4.14b), indicating it was not exactly at the back focal plane of the objective. As a result, the corresponding hologram was not uniformly illuminated. A second an better attempt is shown in Fig. 4.14c, in which we fixed the thread directly to the rear face of the objective. In this case, the borders of the mask appeared to be sharper and the hologram was uniformly illuminated while the low spatial frequencies had been removed.

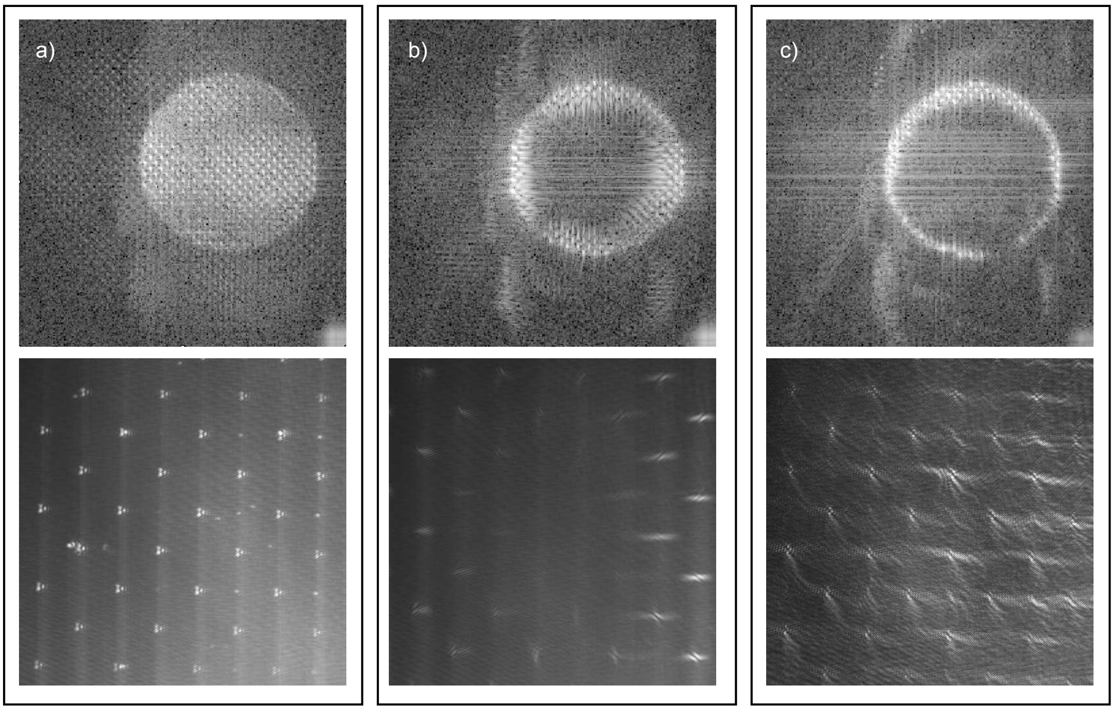

Figure 4.14: Two experimental attempts to block out the central light in our transmission configuration placing a home-made mask near the rear facet of the objective. The upper images show the quadrant containing the +1 diffraction order while the lower images show the corresponding recorded hologram for three cases (same grayscale for all images): a) without any physical mask; b) with a circular mask placed at the microscope turret; c) with a circular mask directly fixed to the rear face of the objective, showing better results.

However, the experimental positioning and centring of the mask came out to be a very arduous task. Moreover, the mask turned out to be too large, covering almost 65 pixels out of the 71 pixel radius of the filtered diffraction order, so the reconstructed image was strongly deteriorated. Future tests will have to include a mechanical translation of the mask and will require a better accuracy in its fabrication.

4.3.1.2 Heterodyne filtering of static objects

Most near-field optical microscopy implementations use a sharp vibrating tip to locally scatter the near-field at the sample surface. In order to discriminate the small scattered signal from the tip apex against the background from a diffraction-limited illumination area, these NSOM configurations usually apply homo- or heterodyne detection using lock-in techniques. In our case, we want to discriminate as well the faint light scattered by the probe particles in motion against the static light scattered by the structure under study. Owing to their Brownian displacements, the light scattered by moving particles is Doppler-shifted with respect to the incident illumination and the frequency spectrum of the resulting signal experiences a Lorentz broadening [37]. Consequently, in this section we propose to investigate the frequency response of the system: for low frequencies we expect a large contribution from the photons scattered by static objects, while for large frequency values the signal from the moving NPs might be predominant. If this hypothesis is validated, this would allow us to suppress the static background in a similar manner to NSOM heterodyne detection.

Previous studies have already validated the use of Digital Heterodyne Holography (DHH) to perform Doppler imaging in various domains such as microfluidics [10], vibration motion characterization [90, 93, 94], *in vivo* blood flow assessment [7, 9, 78] and frequency-resolved temperature response of integrated circuits [84], among others. DHH has also been used for photothermal studies, where a heating laser modulated at a constant frequency offset creates a modulation of the local refractive index of the sample [4]. For the case of Brownian NPs in solution, techniques such as Dynamic Light Scattering and self-mixing laser have studied the dependence of the recorded signal with the frequency offset induced by the moving NPs, being able to calculate the particles' size and concentration [85]. Our aim here is to study whether the introduction of an heterodyning offset frequency could be used to detect only the Doppler-shifted light scattered by moving particles, while still allowing their accurate localization.

Our interferometry setup allows us to investigate dynamic phenomena modulated at any frequency F_{var} by correctly detuning the frequency shift, $\Delta f = f_{AOM1} - f_{AOM2}$, due to the acousto-optic modulators. Supposing a variable frequency F_{var}, then in heterodyne holography the frequency modulation of the object beam is given by:

$$f_{AOM1} = f_{AOM2} - \frac{1}{n} \cdot f_{CCD} - F_{var} \tag{4.13}$$

with n the number of consecutive images used for demodulation (n-phase demodulation). The *static case*, with $F_{var} = 0$, corresponds to the phase-shifting configuration presented in Sec. 1.1.1. For a four-phase detection, the total frequency modulation is one quarter of the camera frame rate. In the *dynamic case*, with $F_{var} \neq 0$, a given frequency is added to the modulation. This case allows the investigation of phenomena modulated at any frequency F_{var}. By dynamically scanning F_{var} one can investigate the entire frequency domain of a system.

However, imaging fast moving objects by means of an n-phase demodulation (implying the combination of n consecutive holograms) requires high acquisition rate detectors. Otherwise, even a two-phase demodulation results in reconstructed images in which the moving objects are completely blurred or appear twice, due to the subtraction of two consecutive holograms at times t_1 and $t_2 = t_1 + T_{CCD}$, with $T_{CCD} = 1/f_{CCD}$, f_{CCD} being the acquisition rate of the camera. In the experiment we show hereafter, we used gold NPs 80 nm in diameter and an acquisition rate of 23 Hz. Under these conditions and using Eq. 3.4 we find that the NP has travelled an average distance of 684 nm from one snapshot to the next, a distance equivalent to 8 pixels. Therefore, even a two-phase demodulation is not well adapted for our imaging purposes and we must content ourselves with simple one-phase detection.

Instead, we suggest to average the signal from multiple reconstructed images acquired at the same frequency. Far from being optimum, this intensity averaging is intended to compensate for the one-phase detection. Fig. 4.15 schematically depicts the irregular impact on the detection efficiency of both the exposure time and frequency rate of the detector as a function of the targeted frequency. While the exposure time is small compared to the signal period, a correct sampling is mostly dictated by the acquisition rate. Except for the particular case in which $f_{CCD} = F_{var}$ (which we have intentionally avoided), a sufficiently long averaging would allow us to sample every time interval inside the slow oscillations. On the other hand, when the exposure time is comparable to the oscillation period, a correct sampling is not feasible, as we are integrating over almost the entire oscillating cycle. The detection efficiency in this case is quite poor. Unfortunately, for this preliminary experience at one-phase reconstruction, the initial phase of the camera trigger was not determined, which prevents us from further quantitative comparison between different acquisition frequencies.

Results

Figure 4.16 shows the frequency spectrum obtained for the moving NPs by sweeping the frequency offset introduced by Δf_{AOM}. In spite of our inhomogeneous detection

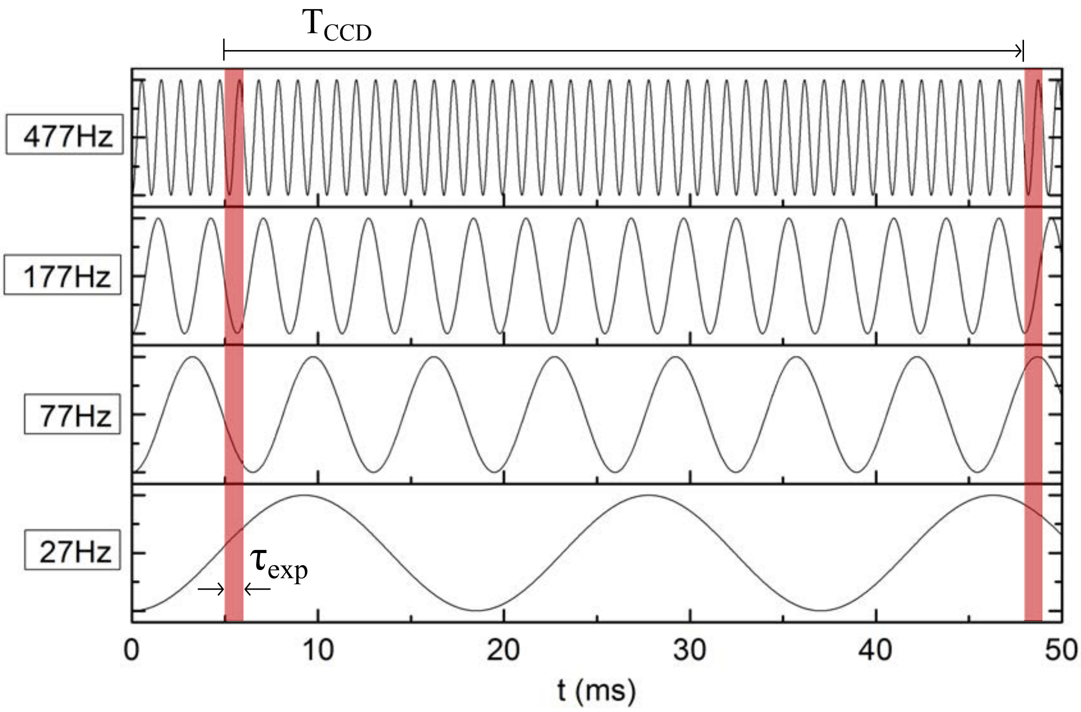

FIGURE 4.15: Schematic of the impact in the holographic detection efficiency of both the exposure time and frequency rate of the detector as a function of the targeted frequency.

efficiency, we recognize the expected Lorentz broadening due to the Doppler-shift on the incident frequency induced by Brownian motion [37].

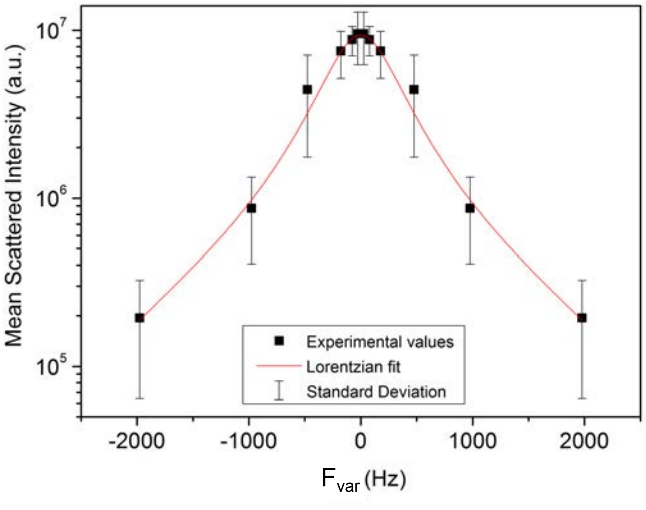

FIGURE 4.16: Frequency spectrum obtained for the moving NPs. In spite of our inhomogeneous detection efficiency, we recognize the expected Lorentz broadening due to the Doppler-shift on the incident frequency induced by Brownian motion.

We then investigated a sample composed of a gold layer, 70 nm thick, evaporated on top of a glass surface (see Fig. 4.8). Figure 4.8 shows the imaged region, where we have overlapped the holographic reconstruction and the white light image for clarity. Note that the gold edge which is parallel to the incident polarization shows strong scattering. In addition, the gold surface presents small scattering defects. For $F_{var} = 0$, the light scattered by moving NPs is even weaker than the surface defects and the surface edges almost blind the CCD camera.

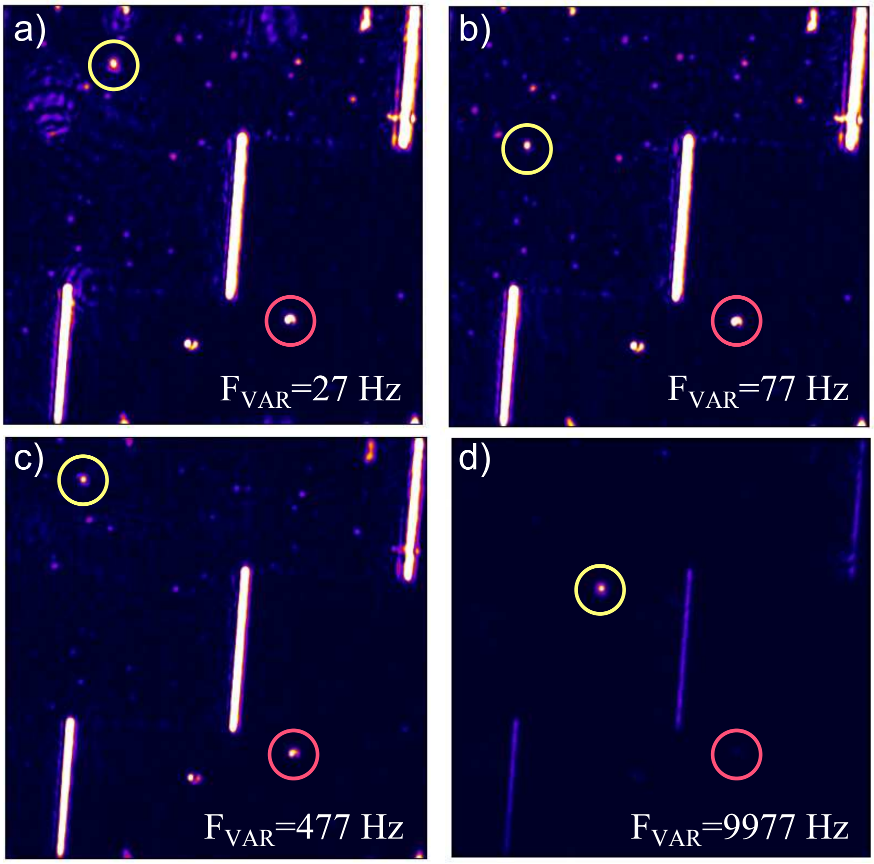

FIGURE 4.17: Decrease in the intensity of the static features (selected in red) for increasing frequency offsets while the moving particles remains clearly visible (in green).

Figure 4.17 shows the reconstructed images for different frequency offsets with the same color scale for the four images. The decrease in the intensity of the static features is evidenced for large frequency offsets while the moving particles remain clearly visible. For every frequency value, we run our localization procedure for both the fixed defect in the gold surface and for a given moving nanoparticle along ten consecutive snapshots. By doing so, we obtain the corresponding scattered intensities and we subsequently calculate the mean value for each set of ten successive localizations. In Figure 4.18 we compare the mean intensity values obtained for the fixed defect and the moving NPs. We indeed confirm the faster decrease in the intensity of the fixed defect for increasing frequency values as compared with the moving NP.

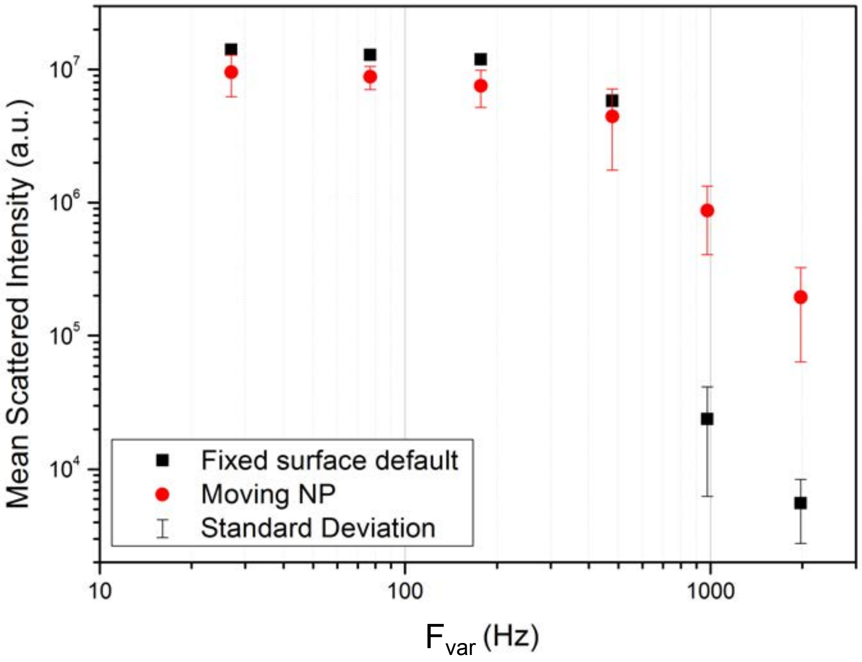

FIGURE 4.18: Mean scattered intensity as a function of the frequency offset.

Conclusions

We have started this chapter with a brief review about the concepts of near-field and evanescent waves. From this basis, we have presented our novel approach on mapping optical fields by holographic imaging, exploiting the light scattering from MNPs undergoing Brownian motion. Using an evanescent wave created by means of a TIR configuration, we have shown that these particles behave as multiple near-field probes, especially revealing the field characteristics along its decay direction. In addition, we have illustrated the possibilities of the technique to deliver a full 3D image of a focused laser beam propagating in water. This work recently led to a joint publication [56].

Finally, we have presented our preliminary results on spatial and temporal filtering of the recorded image during hologram acquisition. This filtering is crucial in order to be able to characterize plasmonic structures, as the light scattered to the far field by the object itself can hinder the detection of the faint probes' scattering. Far from being optimum, the present study nevertheless establishes a preliminary basis for the spatial and temporal filtering of the useful signal coming from the NP probes. In next experimental steps we plan to include a common clock to trigger the CCD camera in agreement with the corresponding frequency detuning. This will allow us derive an analytical expression for the holographic detection efficiency by taking into account the impact of the signal averaging over successive time frames.

Conclusions and Prospects

The work reported in this thesis shows that digital holographic microscopy is a powerful way to localize metallic nanoparticles in 3D with excellent accuracy down to $3 \times 3 \times 10$ nm^3 for 30 nm radius gold particles. This accuracy strongly depends on the available illumination and could be further improved using higher laser power while staying under the particle or solvent damage thresholds. The final optical resolution of the technique is therefore limited either by the size of the particle or the localization accuracy, both well below the diffraction limit.

In addition to working with non-bleaching probes, our holographic setup offers access to 3D optical information over large volumes, whereas most fluorescence-based techniques have limited ranges along the z-direction (typically a few micrometers range). The imaged volume has been shown to be unprecedentedly large: of the order of $40 \times 40 \times 30$ μm^3. The transverse plane extension is determined by the lateral magnification of the objective, while the axial depth is only limited by the aberrations of the microscope, which degrade the PSF far from the plane of best focus.

From this basis, we have successfully coupled our holographic microscope with electrochemistry investigations to study the chemistry reactions of colloidal silver NPs adsorbed onto a thin-film gold electrode. Obtaining rather complementary information from both techniques, we have proved that this coupling facilitates the chemical study of individual particle transformations. Especially, thanks to holography, we have evinced that the electrochemical signal was mostly coming from silver nano-agglomerates. In order to obtain quantitative rates for the investigated chemical processes, and consequently be able to correlate optical intensities to actual particle sizes, a detailed model of the particle/electrode system is currently being developed (using the nature of the particle, its size and its distance to the highly reflecting gold electrode as parameters). Besides, we are working on the use of micro-electrodes as small as our optical field-of-view, in order to stablish a bijective link between individual particle impacts and the corresponding electrical spikes.

The main achievement of this thesis work, however, has been the measurement of the scattered light by MNPs as a way to measure local optical information. Using a holographic setup, we acquire holograms of multiple gold nanoparticles undergoing Brownian motion in a liquid enclosed inside a microfluidic chamber, in the presence of spatially structured optical fields to be characterized. Within acquisition times of the order of few minutes (at a hologram acquisition rate of typically 20 Hz), particles have visited most voxels due to random motion. A computer reconstruction of the scattered intensities at each position yields a 3D map of the optical field in the sample.

By creating an evanescent wave by means of a TIR configuration, we have indeed shown that these particles behave as multiple near-field probes, revealing the field characteristics along its decay direction. In addition, we have illustrated the possibilities of the technique to deliver a full 3D image of a focused laser beam propagating in water. In summary, these results prove our ability to map non propagative fields or fields that are simply not collected by the imaging system (e.g. light propagating along directions beyond the collection cone of the objective) with subdiffraction resolution. In particular, we believe that this technique has the potential to serve as an alternative to other near-field techniques such as NSOM, specially in water-based systems.

Future steps will involve 3D imaging of complex near-field hot spots in a liquid environment, which will be crucial in order to characterize plasmonic structures. We have shown that one major obstacle, however, is the light scattered to the far field by the plasmonic object itself, hindering the detection of the metallic nanoprobes. We have presented the preliminary results of two different strategies, either for spatial or temporal signal filtering, while trying to preserve optimal localization accuracy. The combination of both strategies may also be considered.

Another future approach that we are currently considering relies on recovering the whole sample under study with gold particles and functionalizing them chemically with thiolated DNA strands. Then, freely moving MNPs in the solution, previously functionalized with complementary DNA strands, could lead to the reversible formation of dimers when getting close to the sample. The optical excitation should be adapted to the resonance wavelength of the coupled system. Under these conditions, each transient binding of a free NP with a NP grafted at the sample surface would be perceived as a stochastic alternation of “on” and “off” states. This would produce a signal blinking, allowing us to isolate the light scattered by the dimers from the constant optical background. This approach would therefore provide an equivalent of the photoactivation process used in PALM microscopy, but with all the advantages of working with metallic probes instead of fluorescent probes (possible interferometric detection, unlimited signal yield, single wavelength excitation-detection).

Appendix A

Centiles of the coupon-collector problem

Given a certain risk tolerance θ, what is the minimal number t_θ of snapshots that guarantee that the cumulated number of observations is at least equal to r for each of the N pixels in the field of observations? For the moment we only consider the 2D problem. Note that setting $\theta = 0$ necessarily leads to a diverging t_θ: whatever the number of snapshots, it is impossible to guarantee with 100 % chance that every single pixel will been observed.

Hypothesis:

1. We neglect the time spent by the particle within the pixel which is required in making the k–successive observations, as we consider that an effective unique snapshot with k simultaneous observations (see Fig. 3.11). In the regime of a large number of pixels $10 < N$, the waiting times between two consecutive hits of a Brownian particle is large compared to the time spent by the particle within the pixel.
2. We neglect events leading to multiple hitting particles per single pixel at the same time, due to the large number of pixels N and to the low probability of events per pixel $p = \mu/N$.
3. We do not consider the spatial correlation between neighbouring pixels.
4. We consider that the interface is spatially homogeneous and that the probability vector p is the same for each pixel in the field of observation.

A.1 Time for r observations of each n pixels, one hit at a time ($k = 1$)

In this first next section, we consider that the pixel can be detected only once by a particle, i.e. $p_k = p_0\delta_{k0} + (1 - p_0)\delta_{k1}$. The number of observations of a pixel at each snapshot is a Bernouilli random variable equal to 1 with probability p_1 and to 0 with probability p_0.

Single pixel system Let us first consider the coverage dynamics for a single pixel. The probability for a single pixel to be have collected j observations at the time t is denoted $q_j^{(t)}$. Between two snapshots,

$$q_j^{(t+1)} = p_0 q_j^{(t)} + p_1\, q_{j-1}^{(t)}, \quad 1 \le j \le r-1, \tag{A.1}$$

where $p_1 = p$ is the probability to have a single observation, and $p_0 = 1 - p$ is the probability to have no observations. We consider that the state with r observations is an absorbing state:

$$q_j^{(t+1)} = q_j^{(t)} + p_1\, q_{j-1}^{(t)}. \tag{A.2}$$

Initially, $q_j^{(0)} = \delta_{0j}$: at the initial time $t = 0$, the event that "there has been no observations" has a probability 1. As soon as $j \le t$, the probability to have reached $j \le r-1$ observations of the pixel is:

$$q_j^{(t)} = \frac{t!}{(t-j)!\, j!}\, p^j\, (1-p)^{t-j}, \qquad j \le r-1, \tag{A.3}$$

from which we deduce the last component of the vector $q_r^{(t)} = 1 - \sum_{j=0}^{r-1} q_j^{(t)}$.

Long time distribution We now consider the long-time limit $1 \ll t$ and we recall the equivalence $t!/(t-j)! \sim t^j$ from the Stirling formula. The absorption probability $q_r^{(t)}$ tends to 1, with a leading order term corresponding to the probability $q_{r-1}^{(t)}$:

$$q_r^{(t)} = 1 - t^{r-1} \frac{p_0^t}{(r-1)!} \left(\frac{p_1}{p_0}\right)^{r-1}. \tag{A.4}$$

System of N pixels We now consider the whole system consisting in an ensemble of N pixels. We obtain the full evolution of the system from the evolution of a single pixel

Eq. (A.2):

$$P\left(\left\{N_j^{(t)}\right\}_j\right) = \frac{N!}{N_1^{(t)}\dots N_r^{(t)}}\left\{q_1^{(t)}\right\}^{N_1^{(t)}}\dots\left\{q_r^{(t)}\right\}^{N_r^{(t)}} \tag{A.5}$$

In particular, the probability that all particles are in the absorbing state at the time t is

$$P\left(\{N\delta_{jr}\}_j\right) = \left\{q_r^{(t)}\right\}^N. \tag{A.6}$$

We seek to obtain an expression for the minimal time t_θ corresponding to $P\left(\{N\delta_{jr}\}_j\right) = 1-\theta$. Typically $\theta = 0.05$ and t_θ will be the time after which there is a 95% probability that the whole system of N pixels has been covered r–times. Provided that θ is sufficiently small and N sufficiently large and $1 \gg t_\theta$, we can use the long-time behavior from A.4 to obtain an expression for t_θ as the solution to the following equation:

$$1-(1-\theta)^{1/N} = \frac{p_0^{t_\theta}}{(r-1)!}\left(t_\theta\frac{p_1}{p_0}\right)^{r-1}. \tag{A.7}$$

Provided that $\theta < 0.10$, then $1-(1-\theta)^{1/N} \approx \theta/N$. Taking the log of A.7, we obtain:

$$-(1-p_0)t_\theta + (r-1)\ln\left(\frac{p_1}{p_0}t_\theta\right) = \ln\left(\frac{\theta}{N}\right) + \ln\left[(r-1)!\right] \tag{A.8}$$

where we have used the relation $\ln(p_0) = \ln(1-(1-p_0)) = -(1-p_0)$.

$$t_\theta \approx \frac{1}{1-p_0}\left\{\ln\left(\frac{N}{\theta}\right) + (r-1)\ln\left[\frac{p_1}{p_0(1-p_0)}\ln\left(\frac{N}{\theta}\right)\right]\right\}, \qquad r \ll N. \tag{A.9}$$

Using the relation $1-p_0 = p_1 = \mu/N$, we obtain the following approximate solution of Eq. (A.8) is

$$t_\theta \approx \frac{1}{\mu}\left\{N\ln(N/\theta) + (r-1)N\ln(\ln(N/\theta))\right\}, \qquad r \ll N. \tag{A.10}$$

The latter A.10 has the same scaling with N as $\mathbb{E}[N]$, the mean first time for a to collect a number of r full collections of pictures of the N cards of the game [64] (in which $\mu = 1$).

A.2 Time for r observations of each n pixels, with random number of observations at a time ($k \geq 1$)

In this section, we consider that, at each snapshot, the number of observations of a given pixel is random variable equal to $k \in [0, r]$ with probability p_k and to 0 with probability

p_0 (see Fig. 3.11).

We first consider a single pixel. Using standard Laplace transform techniques, we obtain the probability that this single pixel has been observed j-times during a sequence of t snapshots:

$$q_j^{(t)} = \sum_{(j_0,\dots j_r)} \frac{t!}{j_0!\dots j_r!}\delta\left(\sum_{m=0}^{r} j_m - t\right)\delta\left(\sum_{m=1}^{r} m j_m - j\right) p_0^{j_0} p_1^{j_1}\dots p_r^{j_r}, \quad j \leq r-1 \tag{A.11}$$

$$= \sum_{(j_1,\dots j_r)} \frac{t!}{(t-j_u)!\dots j_r!}\delta\left(\sum_{m=1}^{r} m j_m - j\right) p_0^t \left(\frac{p_1}{p_0}\right)^{j_1}\dots\left(\frac{p_r}{p_0}\right)^{j_r}, \tag{A.12}$$

where δ is the Dirac function and $j_u = \sum_{m=1}^{r} j_m$ is the total number of adsorption events, which we recall is distinct from the number of observations $\sum_{m=1}^{r} m j_m = j$.

From A.11 we seek to determine the asymptotic behavior of $q_r^{(t)} = 1 - \sum_{j=0}^{r-1} q_j^{(t)}$. We want to have a risk less than 5%.

The terms $j_1!\dots j_r!$ is bounded by $r!^r$, hence it does not diverge with t. The leading order in $t \gg 1$ stems from the $t!/(t-j_u)! \sim t^{j_u}$ term. We now consider two specific situations:

- $p_k = p_s\delta(s-k)$ and $p_1 = 0$, with r is a multiple of s (i.e. there exists q such that $r = qs$). The situations amounts to the case considered in the section A.1, with the substitution $r \leftarrow q$ by $p_1 \leftarrow p_s$.
- If $p_1 > 0$, the question is to find the set in sum indices which maximizes the exponent j_u. The set of time interval length $(j_1,\dots j_r) = (j,0,\dots 0)$ maximizes the leading exponent j_u under the constraint that $\sum_{m=1}^{r} m j_m = j$. Moreover, $j = r-1$ trivially maximizes the exponent $j_u = j_1 = j$. At the leading order in t, A.11 reads

  $$q_r^{(t)} = 1 - t^{r-1}\frac{p_0^t}{(r-1)!}\left(\frac{p_1}{p_0}\right)^{r-1}, \tag{A.13}$$

  which is identical to A.4, and leads to the scaling of A.9:

  $$t_\theta \approx \frac{1}{1-p_0}\left\{\ln\left(\frac{N}{\theta}\right) + (r-1)\ln\left[\frac{p_1}{p_0(1-p_0)}\ln\left(\frac{N}{\theta}\right)\right]\right\}, \qquad r \ll N. \tag{A.14}$$

Due to the inequality $\frac{p_1}{(1-p_0)} < 1$, A.14 predits a lower time than A.9, which is expected since large jumps are allowed. This effect is quite low as we retrieve the same scaling for the leading order term ($N \ln(N)$, with $\frac{1}{1-p_0} = N/\mu$).

Conlusion

We recover the same scaling at first orders when $N \gg r$ as in Eq. 3.9 for the mean-time calculation:

$$t_\theta = \frac{1}{1-p_0}\{\ln(N) + (r-1)\ln(\ln(N)) + cnt.\} \tag{A.15}$$

Appendix B

Scientific Activities

Oral Presentations

- **Meta12**, April 2012, Paris, France
- **Photonics West**, February 2013, San Francisco, California
- **Summer School in Plasmonics**, July 2013, Cargèse, Corsica
- **Nanolight 2014**, February 2014, Benasque, Spain
- **JIONC 2014** (Journée d'Imagerie Non Conventionelle), April 2014, Paris, France

Publications

Chemical Physics Letters

- C. Batchelor-McAuley, **A. Martinez-Marrades**, K. Tschulik, A. N. Patel, C. Combellas, F. Kanoufi, G. Tessier, and R. G. Compton, "Simultaneous electrochemical and 3D optical imaging of silver nanoparticle oxidation," Chemical Physics Letters **597**, 20–25, Mar. 2014.

Optics Express

- **A. Martinez-Marrades**, J.F. Rupprecht, M. Gross and G. Tessier, "Stochastic 3D optical mapping by holographic localization of Brownian scatterers," Optics Express **22** (23), 29191–29203, Nov. 2014.

Teaching

Assistant Professor for engineering students at **École Centrale**, Île de France (France). Supervisor of Experimental Activities based on **Optical Coherence Tomography**.

Awards

April 2014: **Judges 1st Price** of the **scientific research spreading contest "Ma thše en 180s"** among PhD students from *UMPC* and *Sorbonne* Universities. The goal of the contest was to orally explain one's own PhD subject to a non-specialised audience in 3min flat. May 2014: **Judges 2nd Price** at the regional final of Île de France.

La physique, ça peut paraître compliqué, mais je me dis que parfois elle ressemble à la peinture. Je suis en thèse de physique, sur un sujet, vous allez voir, très pictural : je développe un nouveau microscope pour faire des images du monde tout petit. Une première nouveauté de mon microscope est la possibilité d'imager des volumes et non pas d'enregistrer une simple projection plate de ce que j'observe, comme ferait par exemple une peinture. C'est pourquoi j'utilise un microscope dit holographique, qui me permet d'acquérir des images tridimensionnelles. Un peu comme nos deux yeux, qui nous donnent deux images que notre cerveau recombine pour en faire une image en 3D, l'holographie se sert d'un double éclairage pour obtenir des images avec de la profondeur.

J'espère donc que vous avez encore vos deux yeux grand ouverts, ainsi que vos oreilles, car maintenant que je vous ai présenté mon microscope holographique, je dois vous dire que ce que je cherche à imager (accrochez-vous bien!) a le mauvais goût d'être invisible! Le but de ma thèse est d'imager des distributions du champ électromagétique qui se créent à l'intérieur d'une minuscule piscine liquide. Vous pouvez imaginer ces champs électromagnétiques comme des courants d'eau chaude et d'eau froide dans cette minipiscine.

L'astuce consiste alors, et voici le deuxième point novateur de mon sujet, à visualiser ces champs par son interaction avec des toutes petites billes métalliques, qui nagent tranquillement dans la minipiscine. Ces nageurs, ce sont des naoparticules qu'on ne peut pas voir à l'oeil nu, mais qui jouent le rôle d'espions, nous révélant des informations autrement inaccessibles.

Mettons-nous dans la peau d'un de ces espions. La nanoparticule est en train de nager tranquillement dans la minipisicne (un immense océan d'ailleur, d'après elle) quand, tout d'un coup, elle ressent un champ électromagnétique dans lequel elle se sent bien, imaginons un courant d'eau chaude, et elle pense: "wow, ce champ et moi, nous sommes *sur la même longueur d'onde, nous sommes vraiment en phase!" et une musique harmonieuse résonne chez elle et la fait rayonner de joie! Puis, au contraire, quand le champ environnant ne lui plaît pas, elle s'éteint un peu et continue sa baignade aléatoire d'un air très sombre.*

Moi, qui regarde dans mon microscope cette piscine scintillante faite de miniparticules en mouvement qui clignotent en fonction du champ qu'elles traversent, je vois se dessiner, petit à petit, une sorte de relief, une peinture par petites touches du champ électromagnétique que je cherche à étudier. J'ose donc dire aujourd'hui que je suis en train de développer un nouveau courant artistique: le pointillisme 3D du 21ème siècle. Bientôt, à l'issue de mon travail de thèse, on devrait pouvoir regarder ces beaux tableaux tridimensionnels se dessiner tout seuls, pendant qu'ils rendent visible l'invisible.

Bibliography

[1] Mie scattering calculator: http://omlc.ogi.edu/calc/mie_calc.html.

[2] RefractiveIndex.INFO website: http://refractiveindex.info.

[3] Abbe, E. (1873, December). Beiträge zur theorie des mikroskops und der mikroskopischen wahrnehmung: I. die construction von mikroskopen auf grund der theorie. *Archiv für Mikroskopische Anatomie 9*(1), 413–418.

[4] Absil, E., G. Tessier, M. Gross, M. Atlan, N. Warnasooriya, S. Suck, M. Coppey-Moisan, D. Fournier, et al. (2010). Photothermal heterodyne holography of gold nanoparticles. *Opt. Express 18*, 780–786.

[5] Albaladejo, S., R. Gómez-Medina, L. S. Froufe-Pérez, H. Marinchio, R. Carminati, J. F. Torrado, G. Armelles, A. García-Martín, and J. J. Sáenz (2010, February). Radiative corrections to the polarizability tensor of an electrically small anisotropic dielectric particle. *Optics Express 18*(4), 3556–3567.

[6] Ashino, M. and M. Ohtsu (1998, March). Fabrication and evaluation of a localized plasmon resonance probe for near-field optical microscopy/spectroscopy. *Applied Physics Letters 72*(11), 1299–1301.

[7] Atlan, M., B. C. Forget, A. C. Boccara, T. Vitalis, A. Rancillac, A. K. Dunn, and M. Gross (2007, April). Cortical blood flow assessment with frequency-domain laser doppler microscopy. *Journal of Biomedical Optics 12*(2), 024019.

[8] Atlan, M., M. Gross, P. Desbiolles, E. Absil, G. Tessier, and M. Coppey-Moisan (2008, March). Heterodyne holographic microscopy of gold particles. *Optics Letters 33*(5), 500–502. WOS:000254565700030.

[9] Atlan, M., M. Gross, B. C. Forget, T. Vitalis, A. Rancillac, and A. K. Dunn (2006, September). Frequency-domain wide-field laser doppler in vivo imaging. *Optics Letters 31*(18), 2762–2764.

[10] Atlan, M., M. Gross, and J. Leng (2006, November). Laser doppler imaging of microflow. *Journal of the European Optical Society - Rapid publications 1*(0).

[11] Baddeley, D., M. B. Cannell, and C. Soeller (2011, March). Three-dimensional sub-100 nm super-resolution imaging of biological samples using a phase ramp in the objective pupil. *Nano Research 4*(6), 589–598.

[12] Bahl, M. and P. Senthilkumaran (2012, November). Helmholtz hodge decomposition of scalar optical fields. *Journal of the Optical Society of America A 29*(11), 2421–2427.

[13] Batchelor-McAuley, C., A. Martinez-Marrades, K. Tschulik, A. N. Patel, C. Combellas, F. Kanoufi, G. Tessier, and R. G. Compton (2014, March). Simultaneous electrochemical and 3d optical imaging of silver nanoparticle oxidation. *Chemical Physics Letters 597*, 20–25.

[14] Betzig, E. (1995). Proposed method for molecular optical imaging. *Optics letters 20*(3), 237–239.

[15] Betzig, E., G. H. Patterson, R. Sougrat, O. W. Lindwasser, S. Olenych, J. S. Bonifacino, M. W. Davidson, J. Lippincott-Schwartz, and H. F. Hess (2006, September). Imaging intracellular fluorescent proteins at nanometer resolution. *Science 313*(5793), 1642–1645.

[16] Bohren, C. F. and D. R. Huffman (1983). *Absorption and scattering of light by small particles*. Wiley.

[17] Boneh, A. and M. Hofri (1997). The coupon-collector problem revisited—a survey of engineering problems and computational methods. *Stochastic Models 13*(1), 39–66.

[18] Cang, H., A. Labno, C. Lu, X. Yin, M. Liu, C. Gladden, Y. Liu, and X. Zhang (2011, January). Probing the electromagnetic field of a 15-nanometre hotspot by single molecule imaging. *Nature 469*(7330), 385–388.

[19] Carter, W. H. (1992). On unwrapping two-dimensional phase data in contour maps. *Optics communications 94*(1), 1–7.

[20] Cheng, X., D. Dai, D. Xu, Y. He, and E. S. Yeung (2014, March). Subdiffraction-limited plasmonic imaging with anisotropic metal nanoparticles. *Analytical Chemistry 86*(5), 2303–2307.

[21] Chowdhury, M. H., J. M. Catchmark, and J. R. Lakowicz (2007). Imaging three-dimensional light propagation through periodic nanohole arrays using scanning aperture microscopy. *Applied Physics Letters 91*(10), 103118.

[22] Costantini, D., L. Greusard, A. Bousseksou, R. Rungsawang, T. P. Zhang, S. Callard, J. Decobert, F. Lelarge, G.-H. Duan, Y. De Wilde, and R. Colombelli (2012, September). In situ generation of surface plasmon polaritons using a near-infrared laser diode. *Nano Letters 12*(9), 4693–4697.

[23] Courjon, D., J.-M. Vigoureux, M. Spajer, K. Sarayeddine, and S. Leblanc (1990, September). External and internal reflection near field microscopy: experiments and results. *Applied Optics 29*(26), 3734–3740.

[24] Davis, C. Lasers and electro optics fundamentals and engineering | optics, optoelectronics and photonics | cambridge university press.

[25] De Wilde, Y., F. Formanek, R. Carminati, B. Gralak, P.-A. Lemoine, K. Joulain, J.-P. Mulet, Y. Chen, and J.-J. Greffet (2006, December). Thermal radiation scanning tunnelling microscopy. *Nature 444*(7120), 740–743.

[26] Diaspro, A., P. Bianchini, G. Vicidomini, M. Faretta, P. Ramoino, and C. Usai (2006, June). Multi-photon excitation microscopy. *BioMedical Engineering OnLine 5*(1), 36.

[27] Douillard, L., F. Charra, Z. Korczak, R. Bachelot, S. Kostcheev, G. Lerondel, P.-M. Adam, and P. Royer (2008, March). Short range plasmon resonators probed by photoemission electron microscopy. *Nano Letters 8*(3), 935–940.

[28] El Badawy, A. M., T. P. Luxton, R. G. Silva, K. G. Scheckel, M. T. Suidan, and T. M. Tolaymat (2010, February). Impact of environmental conditions (pH, ionic strength, and electrolyte type) on the surface charge and aggregation of silver nanoparticles suspensions. *Environmental Science & Technology 44*(4), 1260–1266.

[29] Ernst, D. and J. Köhler (2013). Measuring a diffusion coefficient by single-particle tracking: statistical analysis of experimental mean squared displacement curves. *Physical Chemistry Chemical Physics 15*(3), 845.

[30] Flajolet, P., L. Thimonier, D. Gardy, and others (1987). Birthday paradox, coupon collectors, caching algorithms and self-organizing search.

[31] Fournier, C., L. Denis, and T. Fournel (2010, August). On the single point resolution of on-axis digital holography. *Journal of the Optical Society of America. A, Optics, Image Science, and Vision 27*(8), 1856–1862.

[32] Gabor, D. and others (1948). A new microscopic principle. *Nature 161*(4098), 777–778.

[33] García-Etxarri, A., I. Romero, F. García de Abajo, R. Hillenbrand, and J. Aizpurua (2009, March). Influence of the tip in near-field imaging of nanoparticle plasmonic modes: Weak and strong coupling regimes. *Physical Review B 79*(12).

[34] Ghenuche, P., S. Cherukulappurath, and R. Quidant (2008). Mode mapping of plasmonic stars using TPL microscopy. *New Journal of Physics 10*, 105013.

[35] Gramotnev, D. K. and S. I. Bozhevolnyi (2010, January). Plasmonics beyond the diffraction limit. *Nature Photonics 4*(2), 83–91.

[36] Gross, M. and M. Atlan (2007). Digital holography with ultimate sensitivity. *Optics letters 32*(8), 909–911.

[37] Harris, M., G. N. Pearson, C. A. Hill, and J. M. Vaughan (1995, April). The fractal character of gaussian-lorentzian light. *Optics Communications 116*(1–3), 15–19.

[38] Hell, S. W. and J. Wichmann (1994, June). Breaking the diffraction resolution limit by stimulated emission: stimulated-emission-depletion fluorescence microscopy. *Optics Letters 19*(11), 780–782.

[39] Huang, B., W. Wang, M. Bates, and X. Zhuang (2008, February). Three-dimensional super-resolution imaging by stochastic optical reconstruction microscopy. *Science 319*(5864), 810–813.

[40] Inouye, Y. and S. Kawata (1994). Near-field scanning optical microscope with a metallic probe tip. *Optics letters 19*(3), 159–161.

[41] Jackson, J. D. (1998, August). *Classical Electrodynamics Third Edition* (3 edition ed.). New York: Wiley.

[42] Johnson, P. B. and R. W. Christy (1972, December). Optical constants of the noble metals. *Physical Review B 6*(12), 4370–4379.

[43] Jones, S. A., S.-H. Shim, J. He, and X. Zhuang (2011). Fast, three-dimensional super-resolution imaging of live cells. *Nature Methods 8*(6), 499–505.

[44] Joud, F., F. Verpillat, P. Desbiolles, M. Abboud, and M. Gross (2011). Holographic microscopy for the three-dimensional exploration of light scattering from gold nanomarkers in biological media. In H. V. Sterenborg (Ed.), *Novel Biophotonic Techniques and Applications*, Volume 8090. WOS:000293625400004.

[45] Juette, M. F., T. J. Gould, M. D. Lessard, M. J. Mlodzianoski, B. S. Nagpure, B. T. Bennett, S. T. Hess, and J. Bewersdorf (2008, June). Three-dimensional sub–100 nm resolution fluorescence microscopy of thick samples. *Nature Methods 5*(6), 527–529.

[46] Kawata, S. and Y. Kawata (2000, May). Three-dimensional optical data storage using photochromic materials. *Chemical Reviews 100*(5), 1777–1788. WOS:000087009200006.

[47] Kühn, S., C. Hettich, C. Schmitt, J.-P. Poizat, and V. Sandoghdar (2001, April). Diamond colour centres as a nanoscopic light source for scanning near-field optical microscopy. *Journal of Microscopy 202*(1), 2–6.

[48] Kim, J. and K.-B. Song (2007). Recent progress of nano-technology with NSOM. *Micron 38*(4), 409–426. WOS:000244392400010.

[49] Krachmalnicoff, V., D. Cao, A. Cazé, E. Castanié, R. Pierrat, N. Bardou, S. Collin, R. Carminati, and Y. De Wilde (2013, May). Towards a full characterization of a plasmonic nanostructure with a fluorescent near-field probe. *Optics Express 21*(9), 11536.

[50] Lee, S.-H., Y. Roichman, G.-R. Yi, S.-H. Kim, S.-M. Yang, A. van Blaaderen, P. van Oostrum, and D. G. Grier (2007, December). Characterizing and tracking single colloidal particles with video holographic microscopy. *Optics Express 15*(26), 18275–18282.

[51] Leith, E. N. and J. Upatnieks (1962, October). Reconstructed wavefronts and communication theory. *Journal of the Optical Society of America 52*(10), 1123–1128.

[52] Leith, E. N. and J. Upatnieks (1964, November). Wavefront reconstruction with diffused illumination and three-dimensional objects. *Journal of the Optical Society of America 54*(11), 1295–1301.

[53] Li, H., C.-F. Yen, and S. Sivasankar (2012, July). Fluorescence axial localization with nanometer accuracy and precision. *Nano Letters 12*(7), 3731–3735.

[54] Lieb, M. A., J. M. Zavislan, and L. Novotny (2004). Single-molecule orientations determined by direct emission pattern imaging. *JOSA B 21*(6), 1210–1215.

[55] Maier, S. A. (2007). *Plasmonics: Fundamentals and Applications.* Springer.

[56] Martinez-Marrades, A., J.-F. Rupprecht, M. Gross, and G. Tessier (2014, November). Stochastic 3d optical mapping by holographic localization of brownian scatterers. *Optics Express 22*(23).

[57] Massey, G. A. (1984, March). Microscopy and pattern generation with scanned evanescent waves. *Applied Optics 23*(5), 658–660.

[58] Meixner, A. J., M. A. Bopp, and G. Tarrach (1994). Direct measurement of standing evanescent waves with a photon-scanning tunneling microscope. *Applied optics 33*(34), 7995–8000.

[59] Mie, G. (1908, January). Beiträge zur optik trüber medien, speziell kolloidaler metallösungen. *Annalen der Physik 330*(3), 377–445.

[60] Mock, J. J., R. T. Hill, A. Degiron, S. Zauscher, A. Chilkoti, and D. R. Smith (2008, August). Distance-dependent plasmon resonant coupling between a gold nanoparticle and gold film. *Nano Letters 8*(8), 2245–2252.

[61] Moerner, W. E. and D. P. Fromm (2003). Methods of single-molecule fluorescence spectroscopy and microscopy. *Review of Scientific Instruments 74*(8), 3597.

[62] Moerner, W. E. and L. Kador (1989). Optical detection and spectroscopy of single molecules in a solid. *Physical Review Letters 62*(21), 2535.

[63] Nelayah, J., M. Kociak, O. Stéphan, F. J. García de Abajo, M. Tencé, L. Henrard, D. Taverna, I. Pastoriza-Santos, L. M. Liz-Marzán, and C. Colliex (2007, April). Mapping surface plasmons on a single metallic nanoparticle. *Nature Physics 3*(5), 348–353.

[64] Newman, D. J. (1960, January). The double dixie cup problem. *The American Mathematical Monthly 67*(1), 58.

[65] Novotny, L. (2012). *Principles of Nano-Optics.* Cambridge: Cambridge University Press.

[66] Novotny, L. and N. van Hulst (2011, February). Antennas for light. *Nature Photonics 5*(2), 83–90.

[67] Ortega-Quijano, N., F. Fanjul-Velez, I. Salas-Garcia, O. G. Romanov, D. V. Gorbach, A. L. Tolstik, and J. L. Arce-Diego (2010). Optical phase conjugation by dynamic holography for wavefront restoration in turbid media. In E. D. Jansen and R. J. Thomas (Eds.), *Optical Interactions with Tissues and Cells Xxi*, Volume 7562, pp. 75620A. Bellingham: Spie-Int Soc Optical Engineering. WOS:000284359500006.

[68] Osseforth, C., J. R. Moffitt, L. Schermelleh, and J. Michaelis (2014, March). Simultaneous dual-color 3d STED microscopy. *Optics Express 22*(6), 7028–7039. WOS:000333579300082.

[69] Park, K.-D., D. J. Park, S. G. Lee, G. Choi, D.-S. Kim, C. C. Byeon, S. B. Choi, and M. S. Jeong (2014, February). Operation of a wet near-field scanning optical microscope in stable zones by minimizing the resonance change of tuning forks. *Nanotechnology 25*(7), 075704.

[70] Proppert, S., S. Wolter, T. Holm, T. Klein, S. van de Linde, and M. Sauer (2014, May). Cubic b-spline calibration for 3d super-resolution measurements using astigmatic imaging. *Optics Express 22*(9), 10304.

[71] Punj, D., M. Mivelle, S. B. Moparthi, T. S. van Zanten, H. Rigneault, N. F. van Hulst, M. F. García-Parajó, and J. Wenger (2013, June). A plasmonic 'antenna-in-box' platform for enhanced single-molecule analysis at micromolar concentrations. *Nature Nanotechnology 8*(7), 512–516.

[72] Rayleigh, J. W. S. B. (1871). *On the Light from the Sky, Its Polarization and Colour.*

[73] Rindzevicius, T., Y. Alaverdyan, B. Sepulveda, T. Pakizeh, M. Kall, R. Hillenbrand, J. Aizpurua, and F. GarciadeAbajo (2007, January). Nanohole plasmons in optically thin gold films. *Journal of Physical Chemistry C 111*(3), 1207–1212.

[74] Rust, M. J., M. Bates, and X. Zhuang (2006, October). Sub-diffraction-limit imaging by stochastic optical reconstruction microscopy (STORM). *Nature Methods 3*(10), 793–796.

[75] Schuller, J. A., E. S. Barnard, W. Cai, Y. C. Jun, J. S. White, and M. L. Brongersma (2010, February). Plasmonics for extreme light concentration and manipulation. *Nature Materials 9*(3), 193–204.

[76] Seifi, M., L. Denis, and C. Fournier (2013, October). Fast and accurate 3d object recognition directly from digital holograms. *Journal of the Optical Society of America A 30*(11), 2216.

[77] Sharonov, A. and R. M. Hochstrasser (2006). Wide-field subdiffraction imaging by accumulated binding of diffusing probes. *Proceedings of the National Academy of Sciences 103*(50), 18911–18916.

[78] Simonutti, M., M. Paques, J. A. Sahel, M. Gross, B. Samson, C. Magnain, and M. Atlan (2010, June). Holographic laser doppler ophthalmoscopy. *Optics Letters 35*(12), 1941–1943.

[79] Stebounova, L. V., E. Guio, and V. H. Grassian (2011, January). Silver nanoparticles in simulated biological media: a study of aggregation, sedimentation, and dissolution. *Journal of Nanoparticle Research 13*(1), 233–244.

[80] Stockman, M. I. (2011). Nanoplasmonics: The physics behind the applications. *Physics Today 64*(2), 39–44.

[81] Stuart, E. J. E., N. V. Rees, J. T. Cullen, and R. G. Compton (2012, December). Direct electrochemical detection and sizing of silver nanoparticles in seawater media. *Nanoscale 5*(1), 174–177.

[82] Suck, S. Y., S. Bidault, N. Bonod, S. Collin, N. Bardou, Y. De Wilde, and G. Tessier (2012). Digital heterodyne holography reveals the non-quasi-static scattering behaviour of transversally coupled nanodisk pairs. *International Journal of Optics 2012*, 1–8.

[83] Suck, S. Y., S. Collin, N. Bardou, Y. De Wilde, and G. Tessier (2011, March). Imaging the three-dimensional scattering pattern of plasmonic nanodisk chains by digital heterodyne holography. *Optics Letters 36*(6), 849–851. WOS:000288322800025.

[84] Suck, S. Y., G. Tessier, N. Warnasooriya, A. Babuty, and Y. De Wilde (2010). Frequency-resolved temperature imaging of integrated circuits with full field heterodyne interferometry. *Applied Physics Letters 96*(12), 121108.

[85] Sudo, S., Y. Miyasaka, and K. Otsuka (2006, February). Quick and easy measurement of particle size of brownian particles and plankton in water using a self-mixing laser. *Optics Express 14*(3), 1044–1054.

[86] Synge, E. (1928). A suggested method for extending microscopic resolution into the ultra-microscopic region. *Philosophical Magazine Series 7 6*(35), 356–362.

[87] Thompson, M. A., M. D. Lew, M. Badieirostami, and W. E. Moerner (2010, January). Localizing and tracking single nanoscale emitters in three dimensions with high spatiotemporal resolution using a double-helix point spread function. *Nano Letters 10*(1), 211–218.

[88] Thompson, R. E., D. R. Larson, and W. W. Webb (2002, May). Precise nanometer localization analysis for individual fluorescent probes. *Biophysical journal 82*(5), 2775–2783.

[89] Vandenrijt, J.-F., C. Thizy, P. Queeckers, F. Dubois, D. Doyle, and M. P. Georges (2014, November). Long-wave infrared digital holographic interferometry with diffuser or point source illuminations for measuring deformations of aspheric mirrors. *Optical Engineering 53*(11), 112309. WOS:000339569900021.

[90] Verpillat, F., F. Joud, M. Atlan, and M. Gross (2012, September). Imaging velocities of a vibrating object by stroboscopic sideband holography. *Optics Express 20*(20), 22860–22871.

[91] Verpillat, F., F. Joud, P. Desbiolles, and M. Gross (2011). Dark-field digital holographic microscopy for 3d-tracking of gold nanoparticles. *Optics Express 19*(27), 26044–26055.

[92] Verrier, N. and M. Atlan (2011). Off-axis digital hologram reconstruction: some practical considerations. *Applied Optics 50*(34), H136–H146.

[93] Verrier, N. and M. Atlan (2013). Absolute measurement of small-amplitude vibrations by time-averaged heterodyne holography with a dual local oscillator. *Optics letters 38*(5), 739–741.

[94] Verrier, N., M. Gross, and M. Atlan (2013). Phase-resolved heterodyne holographic vibrometry with a strobe local oscillator. *Optics letters 38*(3), 377–379.

[95] Verrier, N., C. Remacha, M. Brunel, D. Lebrun, and S. Coetmellec (2010, April). Micropipe flow visualization using digital in-line holographic microscopy. *Optics Express 18*(8), 7807–7819. WOS:000276610300028.

[96] Vesseur, E. J. R., R. de Waele, M. Kuttge, and A. Polman (2007, September). Direct observation of plasmonic modes in au nanowires using high-resolution cathodoluminescence spectroscopy. *Nano Letters 7*(9), 2843–2846.

[97] Volkov, V. V. and Y. Zhu (2003). Deterministic phase unwrapping in the presence of noise. *Optics letters 28*(22), 2156–2158.

[98] Walter, N. G., C.-Y. Huang, A. J. Manzo, and M. A. Sobhy (2008, June). Do-it-yourself guide: how to use the modern single-molecule toolkit. *Nature Methods 5*(6), 475–489.

[99] Wang, A., T. G. Dimiduk, J. Fung, S. Razavi, I. Kretzschmar, K. Chaudhary, and V. N. Manoharan (2014, October). Using the discrete dipole approximation and holographic microscopy to measure rotational dynamics of non-spherical colloidal particles. *Journal of Quantitative Spectroscopy and Radiative Transfer 146*, 499–509.

[100] Warnasooriya, N., F. Joud, P. Bun, G. Tessier, M. Coppey-Moisan, P. Desbiolles, M. Atlan, M. Abboud, and M. Gross (2010, February). Imaging gold nanoparticles in living cell environments using heterodyne digital holographic microscopy. *Optics Express 18*(4), 3264–3273. WOS:000274795700006.

[101] Willets, K. A. (2014). Super-resolution imaging of SERS hot spots. *Chemical Society Reviews 43*(11), 3854.

[102] Yamaguchi, I. and T. Zhang (1997, August). Phase-shifting digital holography. *Optics Letters 22*(16), 1268–1270.

[103] Zhang, T. and I. Yamaguchi (1998, August). Three-dimensional microscopy with phase-shifting digital holography. *Optics Letters 23*(15), 1221–1223.